This is to certify that the

dissertation entitled

PROBING THE ELECTRONIC STRUCTURE OF A QUINOENZYME COFACTOR

presented by

VINITA SINGH

has been accepted towards fulfillment
of the requirements for

Ph.D. degree in CHEMISTRY

John L. McCracken
Major professor

Date May 5, 2000

PROBING THE ELECTRONIC STRUCTURE OF A QUINOENZYME COFACTOR

By

Vinita Singh

A DISSERTATION

Submitted to
Michigan State University
in partial fulfillment of the requirements
for the degree of

DOCTOR OF PHILOSOPHY

Department of Chemistry

2000

ABSTRACT

PROBING THE ELECTRONIC STRUCTURE OF A QUINOENZYME COFACTOR

By

Vinita Singh

The electronic structure of the tryptophan tryptophyl-semiquinone (TTQ$^{\bullet}$) cofactor generated by addition of the substrate, methylamine, to methylamine dehydrogenase (MADH) from *Paracoccus denitrificans* has been studied by continuous-wave electron paramagnetic resonance (cw-EPR) and electron spin echo envelope modulation (ESEEM) spectroscopy. The cw-EPR spectrum of TTQ semiquinone prepared by substrate addition (N-form) was found to differ substantially from that observed when the semiquinone was generated by dithionite reduction of the enzyme (O-form). These differences prompted a detailed study of hyperfine and nuclear quadrupole interactions of the three ^{14}N atoms of the semiquinone species using ESEEM. Two of these heteroatoms are derived from the indole and indole-quinone side chains that comprise TTQ, while the third ^{14}N originates from substrate methylamine. Three-pulse ESEEM spectra of the $CH_3{}^{14}NH_2$-reduced sample showed three isolated features at 1.0, 1.5 and 4.3 MHz, which were absent in the MADH sample reduced with $CH_3{}^{15}NH_2$. Analysis of the spectral data for substrate-derived ^{14}N revealed an isotropic hyperfine coupling of 2.4 MHz and nuclear quadrupole couplings characterized by e^2qQ = 1.7 MHz and η = 0.5. The hyperfine and the nuclear quadrupole couplings found for the two ^{14}N nuclei indigenous to TTQ were: A_{iso}, 2.8 and 1.9 MHz; e^2qQ, 3.0 and 2.1 MHz and η, 0.3 and 0.7, respectively. Taken together, these couplings provide definitive evidence that substrate ^{14}N is covalently bound to TTQ when the cofactor is in its one-electron reduced

form and that it has an imine-like structure. The intensities of the modulations indicate that the semiquinone generated by the method recently reported by Zhu and Davidson (*Biochim. Biophys. Acta.*, **1998,** *1364*, 297-300) results in a homogeneous preparation of the radical. A comparison of the ^{14}N hyperfine and nuclear quadrupole couplings measured for the N-form semiquinone with those measured previously for O-form (Warncke, K.; Brooks, H. B.; Lee H.-I.; McCracken, J.; Davidson, V. L.; Babcock, G. T.; *J. Am. Chem. Soc.*, **1995,** *117*, 10063-10075) shows that a significant change occurs in the highest occupied molecular orbital when substrate nitrogen is bound, and may be related to the different redox and electron transfer properties of these two semiquinone forms.

To my family

ACKNOWLEDGMENTS

I wish to thank people who have helped me in some way in carrying out the work presented in this thesis.

First of all I am grateful to my parents for providing me the best education possible that gave me an opportunity to come to the United States for higher education. I am thankful to them for giving me the freedom to choose the path of my choice in my life and for their strong faith in me that whatever I do will be right thing to do.

I am thankful to all the teachers who have taught me so far. My research advisor Prof. J. L McCracken is one of them for whom I have highest respect and gratefulness. I started with no experience in EPR methods, but he patiently helped me learn about EPR and spent time in explaining the working of pulsed EPR spectrometer and in troubleshooting during experiments. I am thankful to him for his support, encouragement and help during the course of this work.

I wish to thank our collaborators Prof. V. L. Davidson and Dr. Z. Zhu from University of Mississippi medical center for supplying the enzyme samples for this work.

I am thankful to Prof. J. F. Harrison, Prof. P. Piecuch, Prof. N. Jackson, Dr. Jesse Edwards, Dr. Rudolf Burcl, Chetan Ahuja, John Goodpaster, and Ian Sedrick O. Pimienta for their help, suggestions and discussion on the molecular orbital calculations.

I wish to acknowledge present and past staff of the department of Chemistry for their help. I wish to thank Kermit Johnson, Paul Reed, Dr. T. B. Atkinson, and Dr. Eric Saari for helping me solve computer-related problems. I wish to thank physical chemistry secretary Vada O' Donell and the secretary for the graduate office, Lisa

Dillingham for their help. I also want to thank John Rugis for making the current pulse generator for the field-jump experiments.

I would like to thank past and present members of Prof. McCracken's and Prof. J. Babcock's research group especially Dr. Vladimir Bouchev, Dr. Marilena Di Valentin, Dr. C. W. Hoganson, Dr. Geörgy Filep, and Constantino P. Aznar III for discussing the fundamentals of EPR. I also wish to thank Dr. M. Mac, Dr. K. Reidy and Dr. S. Smith. I would also like to thank all my friends at MSU for their company.

I am grateful to everyone in my family, my parents, my brother, sister, my grandmother, and my fiancé Karun for their love, support, care and encouragement and for understanding my changing mood.

TABLE OF CONTENTS

LIST OF TABLES

LIST OF FIGURES

Note: Figures IV-10 - figure IV-14 in this dissertation are presented in color.

LIST OF ABBREVIATIONS

AADH	Aromatic amine dehydrogenase
C	The C programming language
Cw	Continuous wave
EDTA	Ethylene diamine tetra acetic acid
ENDOR	Electron nuclear double resonance
EPR	Electron paramagnetic resonance
ESE	Electron spin echo
ESEEM	Electron spin echo envelope modulation
ESR	Electron spin resonance
FET	Field effect transistor
FID	Free induction decay
FORTRAN	Formula translator (programming language)
FT	Fourier transform
$\hbar$	Planck's constant 'h' divided by $2\pi = 1.05459\times10^{-34}$ J.s
Hfi	Hyperfine interaction
HYSCORE	Hyperfine sublevel correlation spectroscopy
FWHM	Full-width-half-maximum
LabVIEW	Laboratory virtual instrument environment workbench
MADH	Methylamine Dehydrogenase
Matlab	Matrix laboratory (programming and visualization software)
Mw	Microwave
NMR	Nuclear magnetic resonance
Nqi	Nuclear quadrupolar interaction
PAS	Principal axis system
Ppm	parts per million
TWTA	Travelling wave tube amplifier

INTRODUCTION

Many vital bioenergetic processes such as respiration, photosynthesis and many other oxidation-reduction reactions involve electron transfer. The mechanism and control of electron transfer within various protein systems, although studied extensively, is still not well understood. Present study is focused on understanding the electron transfer process in one such system using methods of electron paramagnetic resonance spectroscopy. The field of pulsed EPR spectroscopy has made tremendous progress in the past few years and new techniques are being developed to study more complicated and challenged spin systems. Paramagnetic manganese is a transition ion of interest because it acts as a cofactor in many enzymes and can serve as a substitute for a required Mg(II) cofactor in other enzymes. Present studies explored the possibility of simplifying the spectrum of a manganese complex by achieving enhancement in the resolution by application of magnetic field vector jumps.

Chapter I gives a brief introduction to the class of enzymes called quinoenzymes, and focuses on Methylamine dehydrogenase which is a periplasmic enzyme found in gram-negative soil bacteria. Its main function is to catalyze the reactions leading to assimilation of methylamine, the substrate on which these organisms grow. It forms part of a soluble electron transfer complex where it has been possible to study protein-protein interactions and structures using spectroscopic and X-ray crystallographic methods.

In chapter II, principles of Electronic Paramagnetic Resonance (EPR) spectroscopy are discussed along with the need for the pulsed methods. Various interactions of the unpaired electron spin with a magnetic nucleus present in its near

vicinity modify the energy levels involved in the transitions and are discussed briefly. The basic principles of EPR are similar to that of Nuclear Magnetic Resonance (NMR). A thousand-fold larger electron moment than the nuclear moment makes EPR more sensitive to its environment, leading to broader spectral widths and faster relaxation times as compared to NMR.

Although the development of pulsed-EPR techniques faced more technical limitations than those encountered for the pulsed-NMR, it has overcome the earlier challenges and due to the availability of faster digital logic components and advances in microwave technology it is now possible to exploit the potentials of this important spectroscopic technique. The experimental pulsed-EPR data for this study were collected on a home-built pulsed EPR spectrometer built by Prof. J. L. McCracken at Michigan State University in 1990, which has been modified from its original design since then. The main features of this spectrometer are discussed in chapter III.

Results from cw-EPR and electron spin echo envelope modulation (ESEEM) spectroscopic studies on semiquinone forms of the cofactor of MADH are presented and discussed in chapter IV. Quantum mechanical principles discussed in chapter II are used to perform simulations of the experimental results and to extract useful information from the experimental results. Results of Molecular orbital calculations performed on a model compound structurally related to the cofactor of MADH are presented and they provide a qualitative look on the distribution of unpaired spin density studied by the EPR techniques.

Chapter V presents the results of experiments aimed at achieving resolution enhancement of echo detected EPR spectrum of manganese-ethylene (dinitrilo) tetraacetate by magnetic field vector jump at X-band.

Chapter I

INTRODUCTION TO METHYLAMINE DEHYDROGENASE - A BACTERIAL QUINOENZYME

Electron transfer is central to bioenergetic processes such as respiration, photosynthesis and many other oxidation-reduction reactions. Electron transfer in biological systems occurs between protein-bound prosthetic groups separated by long distances, often greater than 10Å, with high efficiency and specificity. The prosthetic groups of most of the oxidoreductases are enzyme-bound quinones and flavins. These prosthetic groups and the membrane-bound components of respiratory electron transfer chains play the important role of coupling the two-electron oxidation of substrates to single-electron carriers during metabolism and respiration. The mechanism and control of electron transfer within various protein systems, although studied extensively, is not well understood. Most electron transfer chains contain membrane proteins that are difficult to purify, crystallize, and study in solution. Methylamine dehydrogenase (MADH, EC 1.4.99.3), which is a periplasmic enzyme found in gram-negative soil bacteria, along with its physiological electron acceptor amicyanin, form part of a soluble electron transfer complex where it has been possible to study protein-protein interactions and structures using spectroscopic and X-ray crystallographic methods.

I.1 Quinoenzymes - a different class of redox enzymes

Quinoenzymes are enzymes whose catalytic mechanisms involve quinone-containing prosthetic groups. The history of the quinoproteins began in the 1960s with

the characterization of the novel prosthetic groups of glucose dehydrogenase[1] and methanol dehydrogenase.[2] More than ten years later, it was demonstrated that the prosthetic group of methanol dehydrogenase was a quinone structure containing two nitrogen atoms,[3] and later it was shown to be pyrrolo-quinoline quinone (PQQ) by X-ray diffraction analysis.[4](figure I-1) A number of other bacterial dehydrogenases were subsequently shown to contain PQQ, and the term quinoprotein was coined to include all these proteins.[5] About this time, incorrect identification of PQQ as the prosthetic group of many other enzymes led to considerable confusion that was resolved with the determination of the structures of other quinone cofactors, Tryptophan tryptophylquinone (TTQ),[6] Topaquinone (TPQ)[7] and Lysine topaquinone (LTQ).[8](figure I-1)

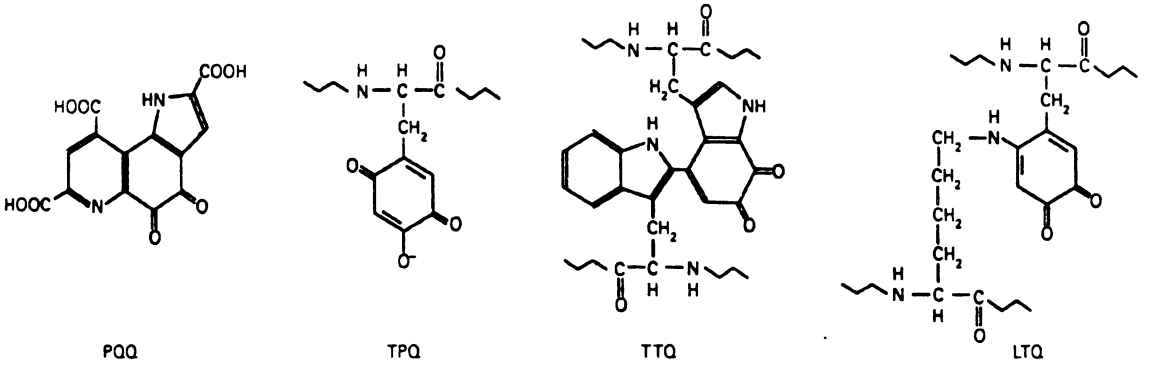

Figure I-1: Structure of known quinone cofactors: pyrrolo-quinoline quinone (PQQ), topaquinone (TPQ), tryptophan tryptophylquinone (TTQ), lysine topaquinone (LTQ).

These cofactors can be bound non-covalently or derived from amino acids in the protein backbone of the enzyme. The only non-covalently bound example is PQQ found in bacterial enzymes. Tryptophan tryptophylquinone (TTQ) is derived from two tryptophan residues and occurs in NAD(P)H-independent alkylamine dehydrogenases from gram-negative soil bacteria. Topaquinone (TPQ) is derived from tyrosine and is the prosthetic group of the copper-containing amine oxidases found in nearly all forms of life, mammals, gram-positive and gram-negative bacteria, yeast, fungi, plants, fish, mollusks, etc. Lysine topaquinone (LTQ) is also derived from tyrosine together with a lysyl residue, and has been recently found in lysyl oxidase, an enzyme required for proper cross-linking of collagen and elastin.[8] Because these cofactors are quinones, they share common chemical and biochemical properties. For example, all three are used by enzymes that oxidize amines and are derived, in a more-or-less direct manner, from amino acyl groups.

I.2 Methylamine dehydrogenase (MADH)

Methylamine dehydrogenase is a periplasmic quinoprotein[9] found in several constitutive and facultative methylotrophic bacteria.[10,11] This enzyme is induced when bacteria grow on a medium containing methylamine as the sole source of carbon and energy.

I.2.1 Structure

The identification of the correct nature and orientation of the redox cofactor of methylamine dehydrogenase faced many acute difficulties. When MADH was first

described, based on its absorption spectra in the presence and absence of the substrate, its sensitivity to carbonyl reagents, and its probable Schiff-base formation, it was suggested that its prosthetic group consisted of a pyridoxal derivative that was acting in a novel fashion.[3,12,13] This group was subsequently thought to be a covalently attached form of PQQ, but this possibility was later excluded by mass spectrometry of a derivative of the isolated prosthetic-group peptide,[14] and by analysis of X-ray data (at 2.25 Å) obtained for the whole enzyme which suggested a precursor form of PQQ (pro-PQQ).[15] The structure of the prosthetic group was finally solved by McIntire and his colleagues by an extensive analysis of its semicarbazide derivative by ^{13}C-NMR and mass spectrometry.[6,16] It is 2′,4-bitryptophan-6,7-dione or Tryptophan Tryptophyl Quinone (TTQ; figure I-2).

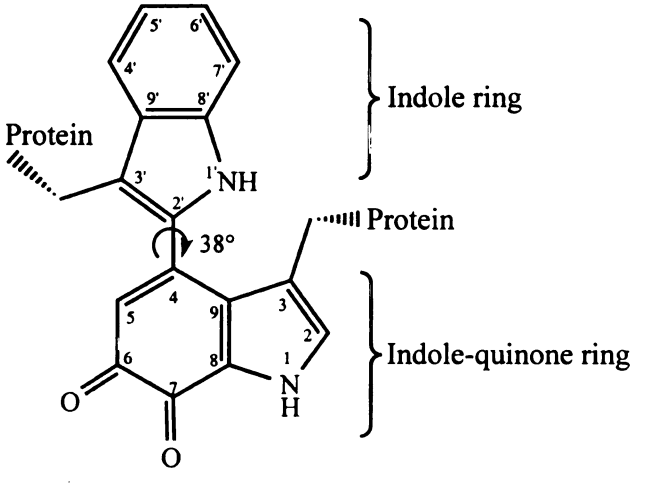

Figure I-2: Structure of the oxidized TTQ cofactor of MADH.

Their proposed structure was consistent with the sequence of the gene for the light subunit of MADH, indicating that the prosthetic group arose by post-translational modification of two tryptophan residues.[17] The structure proposed by McIntire was subsequently shown to fit the X-ray data for methylamine dehydrogenase,[18] and resonance Raman spectroscopy confirmed the presence of same structure in a number of other methylamine dehydrogenases.[6,19-21] The two tryptophan residues that are post-translationally modified are Trp108 and Trp57 and are linked by a covalent bond from C2 of one indole (Trp108) to C4 of the second indole (Trp57), which is also oxidized to an ortho-quinone at C6 and C7 positions (Trq57). The indole and indole-quinone rings of oxidized TTQ are not coplanar, but are at a dihedral angle of 38°.[22] Crystal structures of the resting enzyme in MADH at 1.75 Å,[22] MADH-amicyanin binary complex[23] at 2.24 Å and MADH-amicyanin-cytochrome c_{551i} ternary complex[24,25] at 2.4 Å are now available. The native enzyme is void of metal ion cofactors and has an overall H_2L_2 subunit structure,[22,25] (figure I-3) with the exception of MADH from *Methylobacillus flagellatum*, which has a HL structure. From the functional point of view, MADH can be considered as a pair of HL dimers, H_1L_1 and H_2L_2, related by a molecular twofold axis. The heavy (H) subunits have molecular masses that range from 40 to 50 kD, while the light (L) subunits have molecular masses in the range of 13-16 kD, depending on the source of enzyme. The 373-residue H subunit is disc-shaped and forms a β-propeller structure composed of seven repeated motifs, each having a four-stranded antiparallel β-sheet that resembles the letter W. These seven β-sheets are related by pseudo-7-fold symmetry whose axis passes through the center of the disc and is approximately

perpendicular to the molecular two-fold axis of the tetrameric enzyme. Each L subunit contains 131 residues folded in a tight structure composed of five β-strands that form two antiparallel β-sheets, of two strands and three strands each. A covalently bound TTQ cofactor is present in each of the L-subunits. A channel leading into the active site is located in the H_1L_1 interface. The active site cavity in L_1 subunit containing the quinone oxygen atoms of TTQ is adjacent to the H_1 subunit. In addition to the cross-link provided by TTQ, the small L subunit contains six disulfide bonds.[26] The large subunit does not contain any cysteinyl groups. The H_1L_1 interface is extensive, covering an area of about 1600Å^2. The interface is largely hydrophobic, involving approximately 25 residues from each subunit with additional 20 hydrogen bonds linking the subunits. The H_1L_2 interface is slightly less extensive, covering about 1100Å^2, but has roughly the same number of hydrophobic and hydrogen-bonding interactions. The H_1H_2 interface is the smallest, about 700Å^2, and contains two salt bridges and 12 van der Waals interactions from each subunit. There is no contact between L_1 and L_2. The crystal structure of the binary complex of MADH and amicyanin (both isolated from *P. denitrificans*) shows a composition H_2L_2Amicyanin$_2$.[23,25] Each amicyanin is in contact with both the large and the small subunits of MADH, but its interaction with TTQ-bearing small subunit is more extensive. The structure of both MADH and amicyanin are virtually the same in the binary complex as in the isolated molecules.[24] Most of the TTQ ring system is deeply buried within the L subunit. The modified tryptophylquinone side chain of residue Trq57 is oriented such that it lies in the H-L interface channel with the two carbonyl groups pointing into the channel region. The Trp108 fragment of TTQ has its phenyl portion exposed at the surface of L subunit with atoms C5′ and C6′ only 9.3Å from the

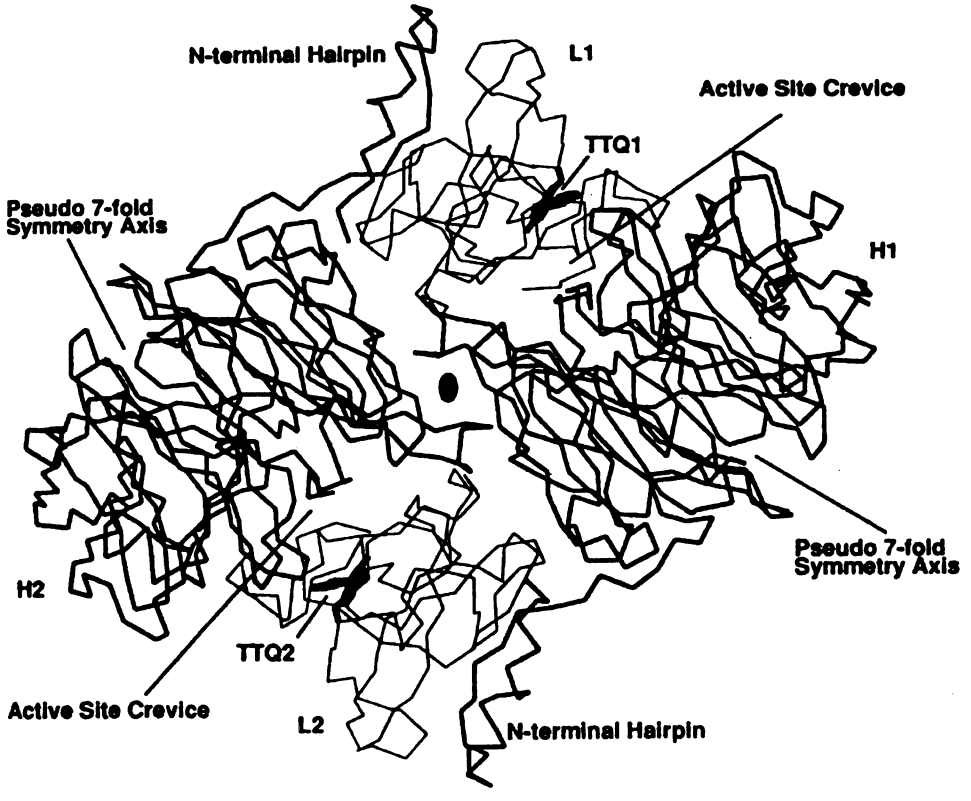

Figure I-3: The tetrameric structure of *PD*-MADH.

Cu site of amicyanin when the MADH-amicyanin complex is formed (figure I-4). The o-quinol of Trq57 is pointed away from Cu and the distance from its C6 to the Cu is 15.8 Å. The cytochrome molecule is also adjacent to the amicyanin, but is separated from both the H and L subunits of MADH within each HLAC (heavy chain, light chain, amicyanin, cytochrome) tetramer. The iron of the heme group and the copper of amicyanin are 24.8 Å apart.

Three of the four heteroatoms of TTQ form hydrogen bonds to the backbone atoms: Trq57 O7 to Asp32 N, Trq57 N1 to Ser30 O/ Gly31 O, and Trp108 N1′ to Ala103 O with average bond distances of 3.0, 2.9 and 3.1 respectively in the two β-subunits. The fourth heteroatom, O6 of Trq57, is hydrogen bonded to side-chains of Thr122 and Asp76. There are two solvent molecules close to this oxygen, one of which has interactions with the main-chain carbonyl groups of Asn104 and Ile106 while the other interacts with the carboxylic group on Asp76. The active-site cavity containing these two solvent molecules is a closed cavity inaccessible to the bulk solvent and is lined with several hydrophobic side chains together with the side chains of Asp32 and Asp76. The most likely route for the substrate to get access to the active site is through a deep channel containing a tight cluster of highly ordered water molecules between the H and L subunits in the HL dimer leading to the protein surface. A phenylalanine side chain of the H subunit (Phe55H) acts as a potential "gate", isolating this large channel from the closed active-site cavity. Movement of this or other side chain or main chain groups would be needed for the substrate to gain access to the active site. Phe55H, side chain of Tyr119L from L subunit and a number of neighboring oxygen atoms may also provide a binding site

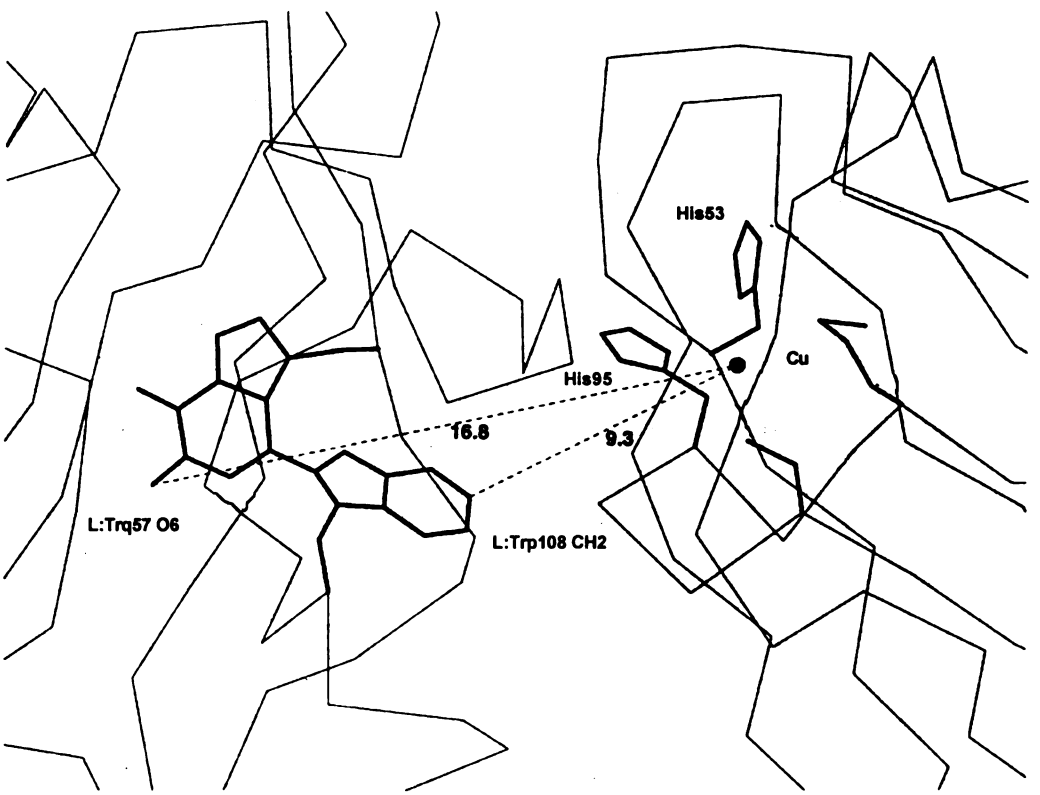

Figure I-4: Orientation of TTQ in the MADH-amicyanin complex showing the relative positions and distances between TTQ and Cu. Only the side chains of TTQ and Cu ligands are shown.

for monovalent cations that are known to affect the reactivity and spectral properties of TTQ as well as the oxidative half reaction. [18,22,27]

I.2.2 Biosynthesis of the TTQ cofactor

TTQ biosynthesis likely requires external enzymes because amine dehydrogenases do not contain metal ions. It has been hypothesized that the first of the two pre-cofactor tryptophan residues (Trp57) in the sequence of the small subunit of the dehydrogenases is converted to a tryptophylquinone in an extra-enzymatic process. This could be followed by an enzyme-mediated or a self-catalytic cross-linking with the partner tryptophan (Trp108) in the sequence.[28] Methylamine-utilizing (*mau*) gene clusters have been isolated and sequenced from several methylotrophic bacteria.[29-31] Studies of these clusters have indicated that at least 12 genes are involved in methylamine utilization. The cluster contains the genes for the large and the small subunits (*mauB* and *mauA*, respectively) of MADH. Several of the clusters harbor the gene for amicyanin. In *Paracoccus denitrificans* (*PD*), the cluster is under the control of a LyrR-type transcription factor.[32] It has been suggested that a peroxidase is involved at some stage in the transformation of Trp to tryptophylquinone and possibly in the tryptophylquinone/Trp cross-linking process.

I.2.3 Spectral and oxidation-reduction properties

The color given to MADH by TTQ is yellow in dilute solutions and blackish-green in concentrated solutions. When MADH is resolved into its individual subunits, only the β subunits exhibit a visible absorption spectrum. Anaerobic titration of *PD*-

MADH with substrate or reductant, sodium dithionite proceeds through the semiquinone intermediate, and reduction of the semiquinone during the second half of the titration was observed to be quite slow indicating that the semiquinone is stable once formed and suggested a kinetic barrier to further reduction. The oxidized, reduced and semiquinone redox states of MADH generated by titration with sodium dithionite have been clearly characterized with regard to their spectral properties. The UV-visible spectra of the three redox states of *PD*-MADH are shown in figure I-5. The absorption spectrum is perturbed at alkaline pH values[33,34] and by the presence of monovalent cations. A pK value of 8.2 was obtained from the pH titration of the spectral changes observed for the oxidized enzyme.[34] At neutral pH, the semiquinone is slowly reoxidized under aerobic conditions, but, the fully reduced enzyme is stable in the presence of oxygen and is slowly reoxidized by ferricyanide. The overall oxidation-reduction midpoint potential (E_m) value of +100mV for the two electron couple (fully oxidized/fully reduced) was obtained by electrochemical titrations of *PD*-MADH.[35]

I.2.4 Function

Quinoproteins may function either as oxidases or dehydrogenases, depending on the nature of their quinone prosthetic group. Quinoproteins that possess TPQ and LTQ are oxidases, whereas those, which possess PQQ and TTQ, are dehydrogenases. It is important, physiologically, that most dehydrogenases do not react with O_2 because their role is to feed electrons derived from the oxidation of substrates, into the respiratory chain, which would otherwise be prevented. It has been recently shown that when

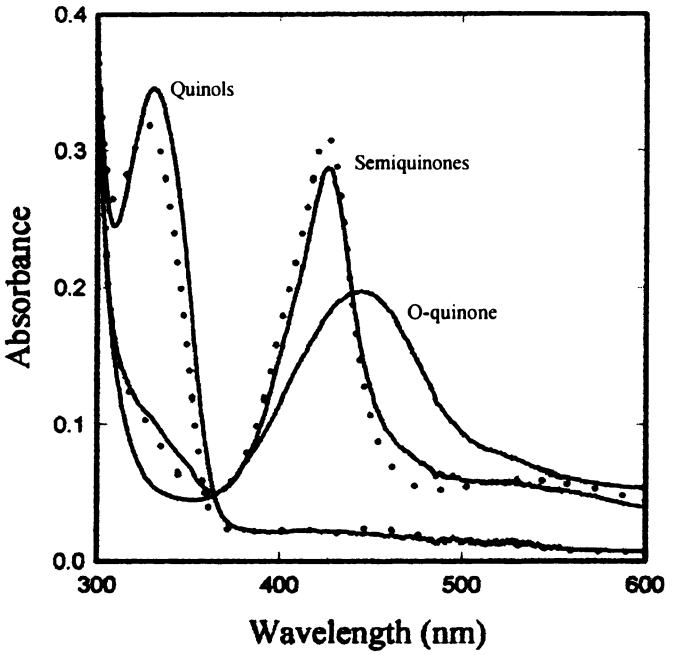

Figure I-5: Absorption spectra of different redox forms of MADH. Spectra of the O-quinone, O-semiquinone, and O-quinol are displayed as solid lines. Spectra of the N-semiquinone and N-quinol are displayed as dotted lines. All spectra were recorded in 6.7 M MADH in 10 mM BTP buffer at pH 7.5 and 25 C. (Taken from reference 54).

MADH is exposed to ultraviolet light in the presence of O_2, it is oxidized and exhibits substrate-dependent steady state oxidase activity.[36] The effects of light are completely reversible and oxidase activity is lost upon removal of light. The light-dependent oxidation of MADH proceeds via a semiquinone intermediate, which accumulates to near stoichiometric levels. The absorption of light may provide the energy needed to

overcome the thermodynamic barrier for electron transfer from TTQ to O_2. This study is focussed on the dehydrogenase activity of MADH.

As a dehydrogenase, MADH transfers electrons, extracted from substrate methylamine, into the electron transport chain in the inner membrane of bacteria for the production of ATP.[37-39] It catalyzes the oxidative deamination of methylamine to yield formaldehyde and ammonia. The net reaction can be written as:

$$CH_3NH_2 + H_2O + 2Ami(Cu^{2+}) \rightarrow HCHO + NH_4^+ + H_3O^+ + 2Ami(Cu^+)$$

This is the first step in the assimilation of methylamine, which serves as a carbon source for methylotrophic bacteria. During this reaction, two electrons are transferred from substrate methylamine to amicyanin (Ami in the above equation), a type I blue copper protein of molecular weight 11.5kD, which mediates electron transfer from MADH to c-type cytochromes.[37,40-42] The sequential electron transfer pathway is then: methylamine → MADH → amicyanin → c-type cytochrome (cytochrome c_{551i}) → cytochrome oxidase. MADH from *Paracoccus denitrificans* (*PD*), *Thiobacillus versutus* (*TV*) and *Methylobacterium extorquens* AM1 (*EX*) is not able to reduce c-type cytochrome in the absence of amicyanin,[11] but MADH from *Methylophilus methylotrophus* W3A1 (*WA*) can act without the mediation of amicyanin.[43]

I.2.5 Reaction mechanism

Deuterium kinetic isotope effect and stopped flow kinetic studies of the reductive half reaction of MADH, showed the absorbance changes upon mixing MADH with

methylamine that were best fit to a single-exponential decay. These results suggest that direct two-electron reduction of TTQ by substrate occurs in the reductive half-reaction.[44] As the oxidation of MADH occurs via two one-electron transfer steps, and the reduction of TTQ is a two-electron process, the overall reaction can be separated into discrete reductive and oxidative half reactions as shown in figure I-6.

In the reductive half (figure I-6a), methylamine reacts with TTQ to form an aminoquinol species. Based on the evidence from the reactions of benzylamines with MADH, it was proposed by Davidson[45] that the reaction is initiated by a nucleophilic attack of substrate amine nitrogen on the quinone carbon to form a carbinolamine intermediate; substitution of the amine nitrogen appears to occur at C6 carbonyl carbon of TTQ.[46] Further evidence for this intermediate was provided by resonance Raman spectroscopy.[19-21] The carbinolamine loses water to form an iminoquinone. A subsequent nucleophilic attack by an active-site base leads to abstraction of a proton from the iminoquinone intermediate to form a carbanion. The X-ray structure of the enzyme indicates that the base is probably Asp76. Benzylamines are not full substrates of MADH, but are competitive inhibitors able to reduce TTQ; analysis of Hammett plots for their reactions with MADH led to the proposal that a key intermediate in the reductive half-reaction is the carbanion.[45] The involvement of a carbanion in the mechanism is supported by the results of a detailed investigation of a second TTQ-containing enzyme, aromatic amine dehydrogenase.[47-49] Hydrolysis of the carbanionic intermediate leads to release of aldehyde and formation of aminoquinol (figure I-6a).

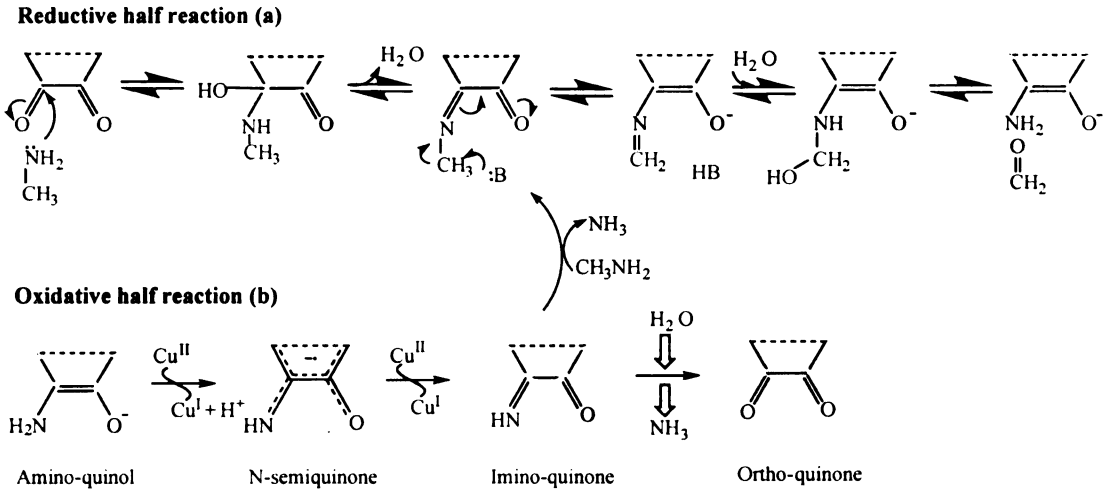

Figure I-6: Proposed reaction pathway for MADH divided into reductive (a) and oxidative (b) steps.

In the subsequent oxidative half reaction (figure I-6b), two electrons are transferred sequentially from the substrate-reduced aminoquinol form of MADH to amicyanin via the formation of an N-semiquinone intermediate.[22] The existence of the N-semiquinone intermediate has been confirmed by kinetic methods,[50] and ESEEM spectroscopy.[51] Potentiometric studies on the pH dependence of the redox potentials for the oxidized/reduced couples of MADH[52] have shown that the quinol is singly protonated while the semiquinone is anionic and deprotonated. This unusual feature provides stabilization of the N-quinol and N-semiquinone reaction intermediates. Conversion of semiquinone to the quinone requires two biochemical events, an electron transfer to amicyanin and release of ammonia from TTQ. These events may occur in a concerted manner or in a sequential fashion. It was initially thought that the first step in

the oxidation of the aminoquinol would involve release of ammonia and production of a semiquinone, with the second electron transfer to amicyanin producing the oxidized quinone.[11,53] It was later shown using rapid scanning stopped-flow spectroscopy[54] that the oxidation of the semiquinone by amicyanin occurs by a sequential mechanism in which oxidation to an iminoquinone precedes hydrolysis and release of ammonia (figure I-6). In the presence of excess of substrate, methylamine rather than water initiates a nucleophilic attack at C6 position to release ammonia and to form the next TTQ-substrate imine adduct. It was also found that the two-electron transfer is linked to transfer of a single proton, which is involved during the conversion of the fully reduced quinol to N-semiquinone form (figure I-6b).[54] These steps in the reductive and the oxidative half reaction involve several acids and bases, which could be fulfilled by side chains of Asp76, Thr122, Asp32 and Tyr119 present near the active site. Since the space in the active site is limited, it is possible that the same residue is involved in more than one step.

This reaction sequence is just one of many chemical mechanisms employed by enzymes for the oxidation of amine substrates, other enzymes catalyzing similar transformations include the flavoproteins trimethylamine dehydrogenase,[55] sarcosine oxidases[56] and the copper-containing amine oxidases that utilize topaquinone (TPQ) as the redox cofactor.[57] The reductive half-reaction which involves cleavage of one of the C-H bonds of methylamine poses a common and major problem to these enzymes, that is the difficulty in cleaving a stable substrate C-H bond. Stopped-flow kinetics have demonstrated the presence of two kinetically significant intermediates, a relatively fast transition due to reduction of TTQ by substrate and a slower transition due to release of the aldehyde product implying a mechanism involving rate-limiting abstraction of a

methyl proton.[58] For bovine plasma amine oxidase, a large isotope effect was explained by a mechanism involving proton tunneling. It is possible that similar quantum mechanical effects play role in the proton abstraction step in the reaction between MADH and methylamine. In a recent study[59] enzymatic breakage of the substrate C-H bond by *WA*-MADH was studied by stopped-flow spectroscopy. The rate of reduction of the TTQ cofactor was observed to have a large kinetic isotope effect (KIE = 16.8 ± 0.5), and the KIE was independent of temperature. Reaction rates were strongly dependent on temperature, indicating that the H-transfer reaction was driven by thermally induced, vibrational motion. From the analysis of the temperature dependence of C-H bond breakage, it was inferred that extreme (ground state) quantum tunneling driven by vibrational motion of the protein scaffold was responsible for the transfer of the hydrogen nucleus. The results demonstrated that classical transition state theory and its tunneling derivatives were not adequate to describe this enzymatic reaction.

Spectroscopic studies on N-semiquinone showed that the delocalization of electrons into the ring system of the semiquinone is consistent with the route for departure of electrons from the indole ring that was proposed on the basis of the X-ray structure[23] and kinetic studies.[60] In the MADH-amicyanin complex, the tryptophan that does not contain the o-quinone (Trp108) lies near the surface, only 9.3 Å away from the amicyanin copper atom. His95, one of the four copper ligands, is on the surface of the protein and about halfway between copper and TTQ, with the shortest distance between them being approx. 5.5 Å (figure I-4). It was therefore suggested that this histidine might mediate electron transfer between the redox centers, thus forming an electron transfer triad.[23] On the basis of stopped-flow kinetics, an electron transfer

pathway was suggested that involves a 3.6 Å jump through space from TTQ to the carbonyl of a proline residue (Pro94) and passage through six covalent bonds to the copper (a total distance of 14 Å)[60]. An alternative pathway was suggested for electron transfer in the ternary complex with cytochrome c, which is moderately more efficient but depends critically on the presence of an intracomplex water molecule.[25]

I.3 Earlier studies on TTQ-semiquinone

Observation of a metastable N-semiquinone intermediate during controlled *in vitro* oxidation of substrate-reduced MADH was reported by Davidson et al (1990)[61] and supported by previous pulsed EPR studies.[51] For these studies, TTQ semiquinone was prepared by comproportionation of a 1:1 molar mixture of oxidized and substrate-reduced TTQ cofactors that resulted from addition of a 0.5 molar equivalent of substrate to the resting enzyme.[62] As a result, enzyme samples contained an approximate 1:1 molar proportion of N-semiquinone, formed by direct substrate-reduction followed by an electron transfer and O-semiquinone, formed by direct one electron reduction of the oxidized TTQ. The N-semiquinone species was not stable in solution at relatively high protein concentrations. In order to minimize oxidation and disproportionation reactions, anaerobic conditions were maintained. For comparative ESEEM studies, semiquinone MADH samples were prepared by comproportionation with ^{14}N- and ^{15}N-methylamine. The resulting ESEEM spectra clearly showed ^{14}N modulations from methylamine derived nitrogen. Because the intensities of these ^{14}N modulations were similar to those found for the heteroatoms of TTQ$^{\bullet}$, the authors concluded that methylamine derived ^{14}N was

covalently bound to TTQ$^{\bullet}$ and that NH_3 release must take place after, or in concert with oxidation of the TTQ semiquinone.[51]

The presence of covalently bound substrate nitrogen atom in TTQ was questioned by Duine et al. (1994)[63,64] and McIntire et al. (1994)[65] based on their studies of the effects of alkali metal ions on the EPR signal of MADH semiquinone. These studies investigated the absorbance changes induced by the addition of a 10^4-10^6 molar excess of the chloride salts of several monovalent cations to the enzyme. Two types of pH dependent effects were noted: small cations (K^+, Na^+) caused bleaching of all absorbance bands in the visible spectrum, whereas large cations (Cs^+, $(CH_3)_2NH_2^+$ $(CH_3)_3NH^+$ and $(CH_3)_4N^+$) caused a red shift in the visible absorbance spectrum. With NH_4^+ and Rb^+, both effects were observed, the former effect at high and the latter at low concentrations. From the observation that the nature of the effect of NH_4^+ is concentration-dependent, it was concluded that MADH has two different binding sites: a high-affinity binding site that specifically binds bigger monovalent cations and a less specific low-affinity binding site that preferentially binds smaller cations. From resonance Raman studies it was noted that the effect of Cs^+, NH_4^+, and $(CH_3)_3NH^+$ on the spectrum of oxidized MADH was to shift the peaks assigned to carbonyl stretching vibrations to lower frequencies. This downshift was explained on the basis of a possible weakening of the C=O bond by the presence of a positive charge. Larger shifts were predicted for the more electropositive K^+ and Na^+ ions, but were not observed. On the basis of above results, these studies proposed an imine elimination mechanism that ruled out the presence of covalent binding between methylamine and TTQ. It was concluded that methylamine and monovalent

cations share the same binding site on MADH. Hence, it was inferred that methylamine is bound to MADH as methylammonium ion ($CH_3NH_3^+$) and is stabilized by the peptide carbonyl oxygens present in the binding site.[64] The fact that the frequencies due to C, N and H vibrational modes of the TTQ remained essentially unaffected by addition of cations, was taken as an evidence that the cations did not affect the TTQ structure. These authors suggested that the ^{14}N-ESEEM detected by Warncke, et al.[51] could have originated from a through-space magnetic coupling, casting doubt on the mechanistic conclusions of the earlier work.

Rapid scanning stopped-flow spectroscopy and global kinetic analysis were used by Davidson, et al. (1996),[50] to demonstrate that the N-semiquinone is a true physiological reaction intermediate which accumulates during two sequential one-electron oxidations of reduced MADH by amicyanin. This study was further substantiated by direct detection of the N-semiquinone intermediate of MADH using ^{15}N-NMR. These authors resolved a ^{15}N-NMR resonance at 54 ppm that was resistant to chemical exchange and was distinguishable from free- or adventitiously bound ^{15}N as it had shorter T_1.[50] These findings were consistent with the proposed mechanism[54] (figure I-6), which involves covalent addition of the substrate nitrogen to TTQ and the formation of an aminosemiquinone after one-electron oxidation of the aminoquinol.

I.4 Usefulness of quinoproteins to higher animals

The usefulness of quinoproteins in nutrition and medicine has been discussed in the past.[66] It is not likely that these quinone cofactors can act as essential nutrients or

vitamins for humans. The release of these cofactors from their parent proteins requires extensive proteolysis and they are released as amino acyl derivatives. Even if these freed cofactors found their way into the human body, there is no known mechanism to incorporate such modified amino acids into nascent polypeptides, although it could be possible that the amino-acyl derivatives could bind noncovalently to an apoprotein. If human enzymes do contain these quinone cofactors, it is more likely that they are also made in situ. TTQ also fails to meet the fundamental requirement of a vitamin, that it should be widely distributed and easily accessible from foods. At present, it is believed that the accessibility of external TTQ is restricted and has little or no significance for the well being of humans. It is produced in situ as an integral component in a limited number of enzymes from small groups of organisms and it is not anticipated that these enzymes will grow significantly.

It has been proposed that the quinoproteins can be used as biocatalysts to produce research and industrial amounts of useful chemicals. In membrane-free cell extracts or for pure quinoproteins, large levels of a desired chemical could be produced if a convenient natural or artificial electron transport chain was used, for example, a pure or partially pure natural electron acceptor for the quinoproteins, or components of methylotroph membrane electron transport chains.[11,38,57,67] Another possible route is coupling the protein directly or via mediators to an electrode for electrochemical regeneration of substrate-reduced enzyme.[68-70] Pure alcohol dehydrogenases[71-73] and methylamine dehydrogenase,[74] have been used to construct immobilized enzyme-based electrodes. These enzyme-based electrodes can be used to produce useful chemicals, and could be designed for use as biosensors to measure levels of specific substances in

biological tissues and fluids, in the same way as has been done with the flavoprotein, glucose oxidase.[71,75]

The role of the semiquinone in catalysis and electron transfer by MADH, and the mechanism by which this enzyme, possessing a four-electron capacity from two cofactors, donates electrons to a one-electron carrier, amicyanin , is not yet understood completely. The present work was directed towards finding evidence in support of the presence of covalently bound substrate nitrogen in the TTQ cofactor, understanding the changes in the electronic properties as a result of covalent binding of the substrate nitrogen into the TTQ ring and getting further insight into the electron transfer process.

List of References

1)Hauge, J. G. *J. Biol. Chem.* **1964**, *239*, 3630-3639.

2)Anthony, C.; Zatman, L. J. *Biochem. J.* **1967**, *104*, 960-969.

3)Duine, J. A.; Frank, J.; Weaterling, J. *Biochim. Biophys. Acta* **1978**, *524*, 277-287.

4)Salisbury, S. A.; Forrest, H. S.; Cruse, W. B. T.; Kennard, O. *Nature* **1979**, *280*, 843-844.

5)Duine, J. A.; Frank, J.; Verwiel, P. E. J. *Eur. J. Biochem.* **1980**, *108*, 187-192.

6)McIntire, W. S.; Bates, J. L.; Brown, D. E.; Dooley, D. M. *Biochemistry* **1991**, *30*, 125-133.

7)Janes, S. M.; Mu, D.; Wemmer, D.; Smith, A. J.; Kaur, S.; Maltby, D.; Burlingame, A. L.; Klinman, J. P. *Science* **1990**, *248*, 981-987.

8)Wang, S. X.; Mure, M.; Medzihradszky, K. F.; Burlingame, A. L.; Brown, D. E.; Dooley, D. M.; Smith, A. J.; Kagan, H. M.; Klinman, J. P. *Science* **1996**, *273*, 1078-1084.

9)De Beer, R.; Duine, J. A.; Frank, J.; Jones, L. H. *Biochim. Biophys. Acta* **1995**, *662*, 370-374.

10)Anthony, C. *PQQ and Quinoproteins*; Jongejan, J. A. and Duine, J. A., eds., Ed.; Kluwer Academic Publishers: Dordrecht, 1989, pp 1-11.

11)Davidson, V. L. *Principles and Applications of Quinoproteins*; Marcel Dekker, Inc.: New York, 1993.

12) van der Meer, R. A.; Jongejan, J. A.; Duine, J. A. *FEBS Lett.* **1987**, *254*, 299-304.

13)Eady, R. R.; Large, P. J. *Biochem. J.* **1971**, *123*, 757-771.

14)McIntire, W. S.; Stults, J. T. *Biochem. Biophys. Res. Commun.* **1986**, *141*, 562-568.

15)Vellieux, F. M. D.; Hol, W. G. J. *FEBS lett.* **1989**, *255*, 460-464.

16)McIntire, W. S. *Methods Enzymol.* **1995**, *258*, 149-164.

17)Christoserdov, A. Y.; Tsygankov, Y. D.; Lidstrom, M. E. *Biochem. Biophys. Res. Commun.* **1990**, *172*, 211-216.

18)Chen, L.; Mathews, F. S.; Davidson, V. L.; Huizenga, E. G.; Vellieux, F. M. D.; Duine, J. A.; Hol, W. G. J. *FEBS Lett.* **1991**, *287*, 163-166.

19)Dooley, D. M.; Brown, D. E. *Meth. Enzymol.* **1995**, *258*, 132-140.

20)Backes, G.; Davidson, V. L.; Huitema, F.; Duine, J. A.; Sanders-Loehr, J. *Biochemistry* **1991**, *30*, 9201-9210.

21)Dooley, D. M.; Brown, D. E. *Principles and Applications of Quinoproteins*; Davidson, V. L., Ed.; Marcel Dekker: New York, 1993, pp 132-140.

22)Chen, L.; Doi, M.; Durley, R. C.; Y., C. A.; E., L. M.; Davidson, V. L.; Mathews, F. S. *J. Mol. Biol.* **1998**, *276(1)*, 131-49.

23)Chen, L.; Durley, R. C.; Poliks, B. J.; Hamada, K.; Chen, Z.-W.; Mathews, F. S.; Davidson, V. L.; Satow, Y.; Huizinga, E.; Vellieux, F. M. D.; Hol, W. G. J. *Biochemistry* **1992**, *31*, 4959-4964.

24)Chen, L.; Durley, R. C.; Mathews, F. S.; Davidson, V. L.; Tegoni, M.; Rivetti, C.; Rossi, G. L. *Protein Sci.* **1993**, *2*, 147-154.

25)Chen, L.; Durley, R. C. E.; Davidson, V. L.; Mathews, F. S. *Science* **1994**, *264*, 86-89.

26)Christoserdov, A. Y.; Boyd, J.; Mathews, F. S.; Lidstrom, M. E. *Biochem. Biophys. Res. Co.* **1992**, *184*, 1181-1189.

27)Chen, L.; Mathews, F. S.; Davidson, V. L.; Huizinga, E.; Vellieux, F. M. D.; Hol, W. G. J. *Protein Struct. Funct. Genet.* **1992**, *14*, 288-299.

28)McIntire, W. S.; Christoserdov, A. Y.; Wemmer, D. E.; Lidstrom, M. E. *Science* **1991**, *252*, 817-824.

29)Willner, I.; Heleg-Shabtai, V.; Blonder, R.; Katz, E.; Tao, G. *J. Am. Chem. Soc.* **1996**, *118*, 10321-22.

30)Lidstrom, M. E.; Christoserdov, A. Y. *Microbial Growth on C_1 Compounds*; Murell, J. C. and Kelly, D. P., Ed.; Intercept: Andover, UK, 1993, pp 381-400.

31)Christoserdov, A. Y.; Christoserdova, L. V.; McIntire, W. S.; E., L. M. *J. Bacteriol.* **1994**, *176*, 4052-4065.

32)van Spanning, R. J. M.; van der Palen, C. J. N. M.; Slotboom, D.-J.; Reijinder, W. N. M.; Stouthamer, A. H.; Duine, J. A. *Eur. J. Biochem.* **1994**, *226*, 201-210.

33)Davidson, V. L. *Biochem. J.* **1989**, *261*, 107-111.

34)Davidson, V. L.; Jones, L. H.; Kumar, M. A. *Biochemistry* **1990**, *29*, 5299-5304.

35)Husain, M.; Davidson, V. L.; Gray, K. A.; Knaff, D. B. *Biochemistry* **1987**, *26*, 4139-4143.

36)Zhu, Z.; Davidson, V. L. *Biochim. Biophys. Acta.* **1998**, *1364*, 297-300.

37)Tobari, J.; Harada, Y. *Biochim. Biophys. Res. Commun.* **1981**, *101*, 502-508.

38)Anthony, C. *Bacterial Energy Transduction*; Anthony, C., Ed.; Academic Press: London, 1988, pp 293-316.

39)Anthony, C. *Principles and applications of Quinoproteins*; Davidson, V. L., Ed.; Marcel Dekker: New York, 1993, pp 223-244.

40)van Houwelingen, T.; Canters, G. W.; Stobbelaar, G.; Duine, J. A.; Frank, J. J.; Tsugita, A. *Eur. J. Biochem.* **1985**, *153*, 75-80.

41)Husain, M.; Davidson, V. L. *J.Biol. Chem.* **1985**, *260*, 4626-4629.

42)Lawson, S. A.; Anthony, C. *Biochem. J.* **1985**, *228*, 719-726.

43)Christoserdov, A. Y.; E., L. M.; Mathews, F. S.; McIntire, W. S. *J. Bacteriol.* **1994**, *176*, 4073-4080.

44)Brooks, H. B.; Jones, L. H.; Davidson, V. L. *Biochemistry* **1993**, *32*, 2725-2729.

45)Davidson, V. L.; Jones, L. H.; Graichen, M. E. *Biochemistry* **1992**, *31*, 3385-3390.

46)Huizinga, E. G.; Vanzanten, B. A. M.; Duine, J. A.; Jongejan, J. A.; Huitema, F.; Wilson, K. S.; Hol, W. G. J. *Biochemistry* **1992**, *31*, 9789-9795.

47)Hyun, Y. L.; Davidson, V. L. *Biochemistry* **1995**, *34*, 816-823.

48)Hyun, Y. L.; Davidson, V. L. *Biochim. Biophys. Acta. Protein Struct. Mol. Enzymol.* **1995**, *1251*, 198-200.

49)Govindraj, S.; Eisenstein, E.; Jone, L. H.; Sanders-Loehr, J.; Christoserdov, A. Y.; Davidson, V. L.; Edwards, S. L. *J. Bacteriol.* **1994**, *176*, 2922-2929.

50)Bishop, G. R.; Brooks, H. B.; Davidson, V. L. *Biochemistry* **1996**, *35*, 8948-8954.

51)Warncke, K.; McCracken, J. L.; Brooks, H. B.; Babcock, G. T.; Davidson, V. L. *J. Am. Chem. Soc.* **1993**, *115*, 63-64.

52)Zhu, Z.; Davidson, V. L. *J. Biol. Chem.* **1998**, *273*, 14254-14260.

53)van Wielink, J. E.; Frank, J.; Duine, J. A. *PQQ and Quinoproteins*; Jongejan, J. A. and Duine, J. A., Ed.; Kluwer Academic Publishers: Dordrecht, 1989, pp 269-278.

54)Zhu, Z.; Davidson, V. L. *Biochemistry* **1999**, *38*, 4862-4867.

55)Rohlfs, R. J.; Hille, R. *J. Biol. Chem.* **1994**, *269*, 30869-30879.

56)Wagner, M. A.; Jorns, M. S. *Arch. Biochem. Biophys.* **1997**, *342*, 176-181.

57)Anthony, C. *Biochem. J.* **1996**, *320*, 697-711.

58)McWhirter, R. B.; Klapper, M. H. *PQQ and Quinoproteins*; Jongejan, J. A. and Duine, J. A., Ed.; Kluwer Academic Publishers: Dordrecht, 1989, pp 259-268.

59)Basran, J.; Sutcliffe, M. J.; Scrutton, N. S. *Biochemistry* **1999**, *38*, 3218-3222.

60)Brooks, H. B.; Davidson, V. L. *Biochemistry* **1994**, *33*, 5696-5701.

61)Christoserdov, A. Y.; Tsygankov, Y. D.; Lidstrom, M. E.; Davidson, V. L. *Meth. Enzymol.* **1990**, *188*, 241-246.

62)Davidson, V. L.; Jones, L. H.; Kumar, M. A. *Biochemistry* **1990**, *29*, 10786-10791.

63)Gorren, C. F. A.; Duine, J. A. *Biochemistry* **1994**, *33*, 12202-12209.

64)Gorren, C. F. A.; Moenne-Loccoz, P.; Backes, G.; Vries, S.; Loehr, J. S.; Duine, J. A. *Biochemistry* **1995**, *34*, 12926-12931.

65)Kuusk, V.; McIntire, W. S. *J.Biol. Chem.* **1994**, *269*, 26136-26143.

66)McIntire, W. S. *Annu. Rev. Nutr.* **1998**, *18*, 145-177.

67)Anthony, C. *Principles and applications of Quinoproteins*; Davidson, V. L., Ed.; Marcel Dekker: New York, 1993, pp 17-45.

68)Hill, H. A. O.; Hunt, N. I. *Methods Enzymol.* **1993**, *227*, 501-522.

69)Davidson, V. L. *Am. Biotech. Lab.* **1990**, *8*, 32-34.

70)Burrows, A. L.; Hill, H. A. O.; Leese, T. A.; McIntire, W. S.; Nakayama, H.; Sanghera, G. S. *Eur. J. Biochem.* **1991**, *199*, 73-78.

71)Karube, I.; Yokoyama, K.; Kitagawa, Y. *Quinoproteins as biosensors in Principles and Applications of Quinoproteins*; Davidson V. L., E., Ed.; Marcel Dekker, Inc.: New York, 1993, pp 429-46.

72)Stigter, E. C. A.; de Jong, G. A. H.; Jongejan, J. A.; Duine, J. A.; van der Lugt, J. P.; Somers, W. A. C. *Enzym. Microb. Technol.* **1996**, *18*, 489-94.

73)Zhao, S.; Lennox, R. B. *Anal. Chem.* **1991**, *63*, 1174-78.

74)Loughran, M. G.; Hall, J. M.; Turner, A. P. F.; Davidson, V. L. *Biosensors Bioelectron.* **1995**, *10*, 569-76.

75)Raba, J.; Mottola, H. A. *Crit. Rev. Anal. Chem.* **1995**, *25*, 1-42.

Chapter II

PRINCIPLES OF CONTINUOUS WAVE AND PULSED ELECTRON PARAMAGNETIC RESONANCE SPECTROSCOPY

II.1 Continuous wave Electronic Paramagnetic Resonance (cw-EPR)

Electronic Paramagnetic Resonance (EPR) spectroscopy is a technique applicable to systems with net electron spin angular momentum. In this experiment an oscillating microwave magnetic field is applied to a paramagnetic system in order to invert its electron magnetic moment in the presence of an external magnetic field. The basic principles of EPR are similar to that of Nuclear Magnetic Resonance (NMR). A thousand-fold larger electron moment makes EPR more sensitive to its environment, leading to broader spectral widths and faster relaxation times as compared to NMR. Many useful NMR techniques like magic-angle spinning, decoupling nuclei during an FID are not routine in EPR because of technological limitations. The theory, instrumentation and methodology of EPR spectroscopy has been described in several books and journal articles.[1-8] In this chapter principles of cw-EPR and pulsed-EPR methods are discussed briefly.

II.1.1 The electronic Zeeman interaction

In a molecule, permanent magnetic dipoles are associated either with electrons or with nuclei. The magnetic dipoles attributable to the electrons arise from net spin or net orbital angular momentum or a combination of these. In most of the molecules the contribution from the spin angular momentum dominates. The magnetic dipole can interact with the magnetic component of the microwave radiation. When such a molecule

is irradiated with a range of spectral frequencies, it normally leads to no absorption attributable to a magnetic interaction, because the energy levels are degenerate. In the presence of a static magnetic field, which can also be provided internally by the nuclei of a molecule (section V.1.2), this degeneracy is lifted and absorption attributable to magnetic dipole transitions may occur. The permanent magnetic dipole moment (μ_e) arising from net electron spin angular momentum (**S**) is given by,

$$\mu_e = -g\,\beta\,\mathbf{S} = -\gamma\,\hbar\,\mathbf{S} \qquad [2.1]$$

The negative sign indicates that for an electron the magnetic moment is antiparallel to the spin, g has a value of 2.0023 for a free electron and is considered isotropic in the above expression, β the is Bohr magneton, the magnetic moment for one unit of quantum mechanical angular momentum. It is defined by $\beta = e\hbar/2m_e$ in MKS units, where, e is the charge on an electron, m_e is the mass of an electron. γ is the gyromagnetic ratio, the ratio of the magnetic moment to the angular momentum for an electron. According to the classical electrodynamics, the electron spin will experience a torque equal to $\mu_e \times \mathbf{B_0}$ in the presence of an external magnetic field ($\mathbf{B_0}$). So, the magnetic moments will take preferred orientations. The individual spins will precess around the magnetic field axis at angular frequency $\omega_o = g\,\beta\,B_o$, also called the Larmor frequency which is roughly 8.3 GHz at magnetic field of 0.3 T. The energy of a magnetic dipole in a static external magnetic field, B_o, is given by the expression,

$$W = -\mu_e \cdot \mathbf{B_0} \qquad [2.2]$$

For a quantum mechanical system the interaction energy of a spin with the external magnetic field is quantized. The electronic Zeeman Hamiltonian describing the interaction of electron magnetic moment with the magnetic field is,

$$\mathcal{H}_{e\text{-}Zeeman} = -(-g\,\beta\,\mathbf{S}) \cdot \mathbf{B_0}, \qquad [2.3]$$

The eigenvalues for the projection of **S** on to a specified direction, usually the **z** direction of a cartesian coordinate system are $M_s\hbar$ where M_s can have values from -S to +S in integral steps. So, there will be (2S + 1) states with different energies and spin orientations. If the direction of $\mathbf{B_0}$ is along z-axis, the Hamiltonian [2.3] can be rewritten as,

$$\mathcal{H}_{e\text{-}Zeeman} = g\,\beta\,B_0S_z$$

and its energy eigenvalues are,

$$E_{e\text{-}Zeeman} = g\,\beta\,B_0M_s \qquad [2.4]$$

For a species with single unpaired electron, $M_s = \pm 1/2$, so there will be two possible energy levels corresponding to two possible orientations of the electron, parallel and antiparallel to the external magnetic field (figure II-1). A transition between these levels would involve a change in the orientation of the electron magnetic moment. Hence, the radiation inducing the transition must be polarized such that its oscillating magnetic field has a component perpendicular to the static magnetic field. The transition energy falls in the microwave range and is given by,

$$\Delta E = g\,\beta\,B_0 \qquad [2.5]$$

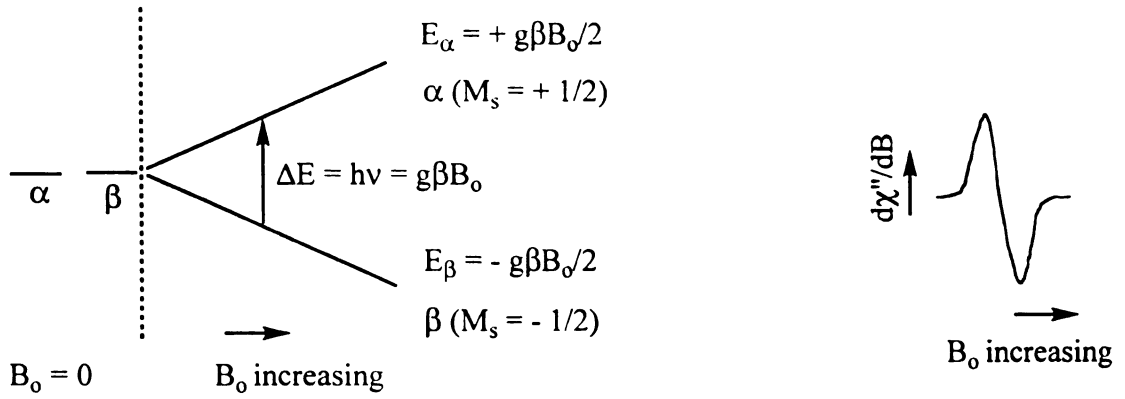

Figure II-1: (a) Splitting of degenerate α and β electron spin states due to electron Zeeman interaction in the presence of applied static magnetic field B_o. (b) An EPR line expected from a transition in (a) for systems with isotropic g value.

As a result of absorption of microwave radiation, the microwave power returned from the sample to the detector changes and is detected as an absorptive peak. The EPR spectrum is a plot of intensity against the strength of applied magnetic field and due to the phase sensitive detection system usually employed, it is recorded as a derivative curve. The features are easily visible in a derivative mode if the absorption lines are broad. Difference in the transition energies for different molecules are described by changes in the g-values, hence g-value is characteristic of the sample. The g value can be dependent on the orientation of the molecular axis with respect to the external field. This anisotropy in g-factor can arise from coupling of the spin angular momentum with the orbital angular momentum. The spin-orbit coupling is described by the Hamiltonian,

$$\mathcal{H}_{LS} = -\lambda \mathbf{L} \cdot \mathbf{S} \qquad [2.6]$$

where **L** is the orbital angular momentum and λ is spin-orbit coupling constant for a particular shell in particular atom. The spin angular momentum is oriented with the field, but the orbital angular momentum, which is associated with electrons moving in molecular orbitals, is locked to the molecular wave function (figure II-2). The total angular momentum (**J**) of electron is the vector sum of spin (**S**) and orbital (**L**) components, **J** = **L** + **S**, where **J** has the possible magnitudes | L - S |, | L - S +1 |,..., | L + S |. When the effects of orbital moment are small, they are incorporated into the g value thus, making the g value anisotropic. This corresponds to combining $\mathcal{H}_{e\text{-}Zeeman}$ and $\mathcal{H}_{LS}$ and the overall magnetic moment is given by, $\mu = g\,\beta\,\mathbf{J}$ and the g factor is modified as,

$$g = \frac{3}{2} + \frac{S(S+1) - L(L+1)}{2J(J+1)} \qquad [2.7]$$

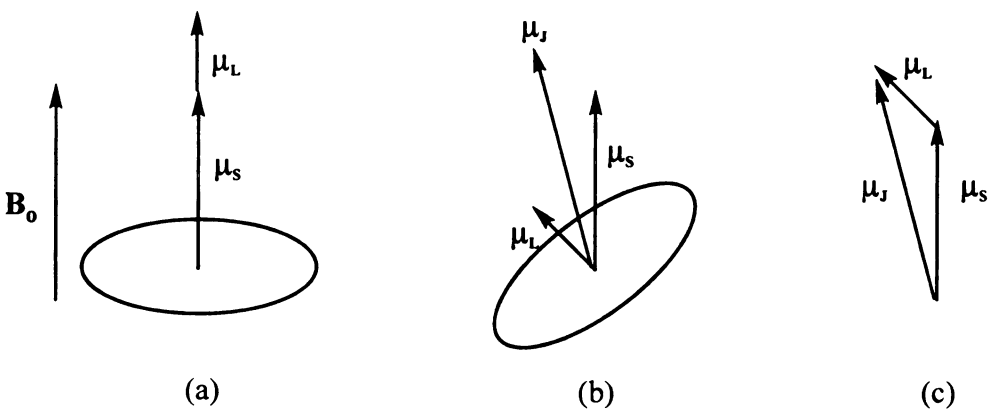

Figure II-2: Coupling of the projections of the spin and the orbital angular momentum in case of two different molecular orientations, (a) and (b), relative to the applied static magnetic field $\mathbf{B_0}$. (c) The vector addition of orbital and spin magnetic moments.

The modified Hamiltonian is given by,

$$\mathcal{H}_{e\text{-}Zeeman} = \beta \mathbf{B_0} \cdot \mathbf{g} \cdot \mathbf{S} \qquad [2.8]$$

where **g** is a tensor. In some cases the **g** tensor can have axial symmetry, i.e. $g_{||} = g_{zz}$; $g_{\perp} = g_{xx} = g_{yy}$, where z-axis defines the axis of symmetry. In general, **g** forms a symmetric tensor with six components, which could be diagonalized by finding its principal axis system.

Quantum mechanically EPR spectrum can be interpreted as the allowed transitions between the eigenvalues of the *effective spin Hamiltonian* containing all the terms that modify the EPR transition energies given by equation 2.5. These include electron-nuclear hyperfine interaction (hfi), nuclear Zeeman interaction, nuclear quadrupolar interaction (nqi), zero field splitting (zfs) etc. resulting from the interaction of electron with nearby charges, dipoles and quadrupoles. These effects that modify electron energy levels are discussed below.

II.1.2 Nuclear Zeeman interaction

Protons and neutrons both have a spin quantum number of 1/2 and depending upon how they pair up in the nucleus, the nucleus may or may not have a net non-zero nuclear spin. If the spins are all paired, then there will be no net spin and the nuclear spin quantum number *I* will be zero. When the number of protons and neutrons are not both even, then the nucleus can have net spin. Nuclear spins may be integral or half integral. There is a magnetic moment μ_N associated with the nuclear spin angular momentum **I**,

$$\mu_N = g_N \beta_N \mathbf{I} = \gamma_N \hbar \mathbf{I}, \qquad [2.9]$$

where γ_N is the nuclear gyromagnetic ratio and is characteristic of the isotope, β_N is nuclear magneton, g_N is nuclear g-factor characteristic of a specific nucleus. In contrast to the electron magnetic moment (eq. 2.1), there is no negative sign in eq. 2.9 indicating that nuclear spin and magnetic moment are parallel. This holds true for protons and most of the nuclei, but for those nuclei that are one neutron short of being factorizable into an integral number of ^{4}He units, e.g. ^{15}N, a negative gyromagnetic ratio, where nuclear spin and magnetic moment are antiparallel, is found. The interaction energy of a nuclear magnetic moment with an applied magnetic field is also quantized, and there are (2I + 1) allowed values for its projection on the field axis, given by -I, (-I +1),..., +I. The axis of quantization of the nucleus reorients when an electron spin transition occurs. The nuclear Zeeman Hamiltonian describing the interaction of nuclear magnetic moment with the magnetic field directed along the z-axis is,

$$\mathcal{H}_{nuc\text{-}Zeeman} = -(\gamma_N \hbar \mathbf{I}) \cdot \mathbf{B_0} = -\gamma_N \hbar B_0 I_z, \qquad [2.10]$$

The energies of nuclear Zeeman levels are given by,

$$E_N = -\gamma_N \hbar B_0 m_I \qquad [2.11]$$

This would lead to splitting of energy levels (figure II-3). In a 0.3 T magnetic field, typical for EPR at X-band frequencies, the nuclear Larmor frequency for protons is about 14 MHz (*cf.* $\omega_{o,\,electron}$, II.1.1). The nuclear Zeeman effect is much smaller than the

electronic Zeeman interaction and typically smaller than the hyperfine interactions. It can often be neglected during simulations of EPR spectra.

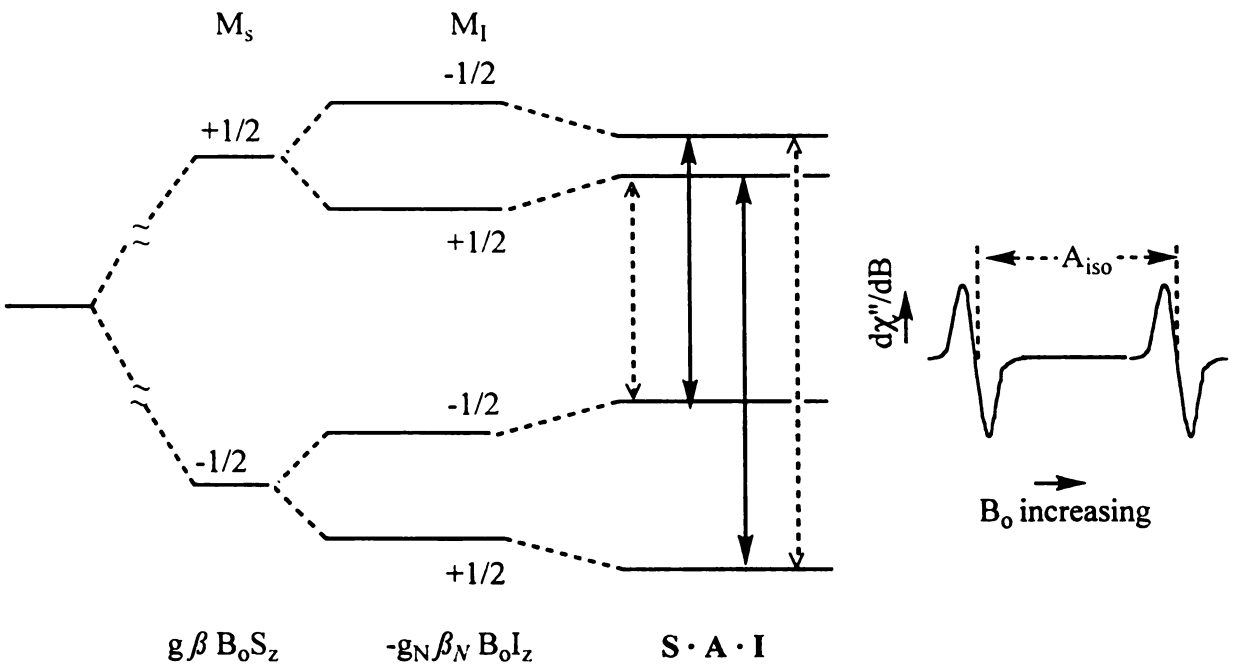

Figure II-3: (a) Energy level diagram showing the effects of electron Zeeman, nuclear Zeeman and Hyperfine interactions of an unpaired electron (S = 1/2) with a I = 1/2 nucleus in the presence of an external magnetic field $\mathbf{B_o}$; (b) Resulting EPR spectrum.

II.1.3 The hyperfine interaction

The interaction between the electron spin and neighboring nuclear spins is called the electron-nuclear hyperfine interaction (hfi). An unpaired electron in the vicinity of a nuclear spin experiences a local magnetic field generated by the nearby nucleus ($\mathbf{B_{local}}$). The transition energy modified by hfi is given by, $\Delta E = g\beta (B_o + B_{local})$, the value of B_o needed to excite a transition will depend on B_{local}. A nuclear spin is quantized in the total magnetic field it experiences, which is the resultant of $\mathbf{B_o}$ and the field due to electron. For a nuclear spin I, there are (2I + 1) distinct nuclear spin states and each of these gives

rise to a different local field at the electron. The energy differences between the nuclear spin states are small, and all the nuclear spin states are equally populated for practical purposes. Thus, there are (2I + 1) possible values of B_0 that can fulfill the resonance condition and these occur with equal weight. As a result the spectrum is split into (2I + 1) lines of equal intensities.

For the case of an axial hfi, the electron-nuclear coupling can be separated into two components, the anisotropic dipole-dipole interaction and the isotropic Fermi contact interaction. When an unpaired electron has access to an s-orbital associated with a magnetic nucleus, there is a non-zero probability density of the electron and nuclear moments "contacting" one-another. Because s-orbitals have spherical symmetry, the resulting hfi is isotropic and is known as Fermi contact interaction. The energy of this isotropic hyperfine interaction is given approximately by,

$$E_{iso} = -2/3\ \mu_o\ |\psi(0)|^2\ \mu_e \cdot \mu_N \qquad [2.12]$$

where μ_o is the permeability of vacuum and $|\psi(0)|^2$ is the probability of finding an electron at the nucleus assuming that the electron probability distribution is uniform over the volume of the orbital. Using equations 2.1 and 2.9 to replace magnetic moments by their operators, the Hamiltonian can be written as,

$$\mathcal{H}_{iso} = A_{iso}\hat{S} \cdot \hat{I}, \qquad [2.13]$$

A_{iso} is called isotropic hyperfine coupling constant expressed in frequency units and is defined as,

$$A_{iso} = -2/3\ \mu_o g\ \beta\ g_N \beta_N |\psi(0)|^2 \qquad [2.14]$$

Thus, the isotropic hyperfine coupling is proportional to the probability of finding the unpaired electron at the nucleus. Hence, magnetic nuclei in paramagnetic molecules can provide information about the unpaired electron distribution and its wavefunction.

The anisotropic hyperfine interaction arises from the magnetic interaction between the magnetic dipoles of the electron and a nearby nucleus. This interaction occurs when the electron is in an orbital with orbital quantum number $l > 0$. Because the electron probability distribution for these orbitals is zero at the nucleus, the Fermi contact interaction is not possible. As these orbitals have non-spherical symmetry, this hyperfine interaction is anisotropic. For the case of an atom with nucleus at a distance 'r' from the electron at the origin, (figure II-4) the dipolar interaction energy can be obtained by assuming the electron and nuclear dipoles to be point dipoles. Then, using the point dipole-dipole model, the energy of a magnetic dipole in the field of the other is,

$$E_{dipolar} = \frac{\mu_e \cdot \mu_N}{r^3} - \frac{3(\mu_e \cdot \mathbf{r})(\mu_N \cdot \mathbf{r})}{r^5} \qquad [2.15]$$

and the Hamiltonian describing such interaction can be written as,

$$\mathcal{H}_{dipolar} = -g\ \beta\ g_N \beta_N [\hat{S} \cdot \hat{I}/r^3 - 3(\hat{S} \cdot \mathbf{r})(\hat{I} \cdot \mathbf{r})/r^5] \qquad [2.16]$$

The above Hamiltonian can be expanded in the Cartesian coordinates as,

$$\mathcal{H}_{dipolar} = -\frac{\mu_o}{4\pi} g\ \beta\ g_N \beta_N \left\{ \frac{(r^2 - 3x^2)}{r^5} I_x S_x + \frac{(r^2 - 3y^2)}{r^5} I_y S_y + \frac{(r^2 - 3z^2)}{r^5} I_z S_z + \right.$$

$$\left. - \frac{3xy}{r^5}(I_x S_y + I_y S_x) - \frac{3yz}{r^5}(I_y S_z + I_z S_y) - \frac{3zx}{r^5}(I_z S_x + I_x S_z) \right\} \qquad [2.17]$$

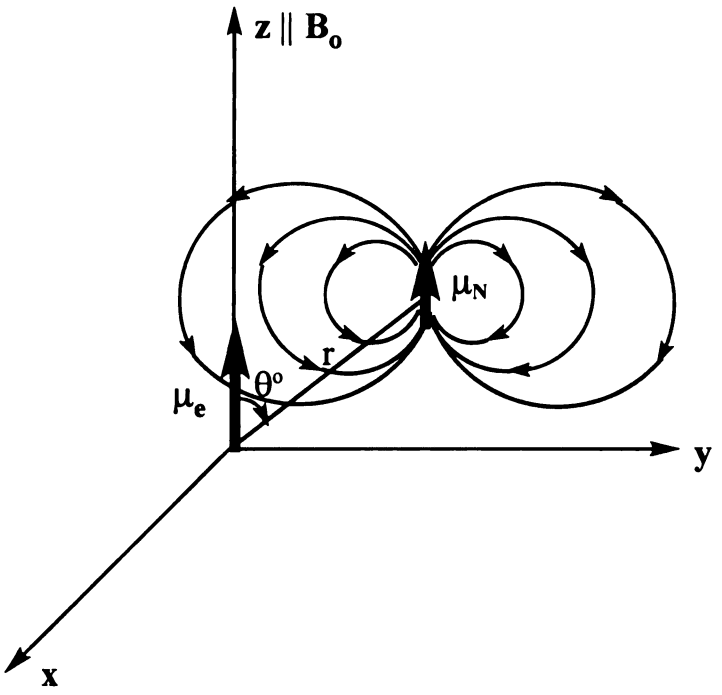

Figure II-4: Dipolar interaction of magnetic dipoles μ_N and μ_e due to nuclear spin angular momentum and electron spin angular momentum respectively. The lengths of vectors μ_N and μ_e are not drawn to scale. The electron is at the origin at a distance 'r' from the nucleus. The dipoles are aligned with the external magnetic field and θ is the angle between the electron-nuclear vector r and the applied external magnetic field $\mathbf{B_0}$.

By integrating over the spatial wavefunction [2.17] can be written as,

$$\mathcal{H}_{dipolar} = T_{xx}I_xS_x + T_{yy}I_yS_y + T_{zz}I_zS_z + T_{xy}(I_xS_y + I_yS_x) + T_{yz}(I_yS_z + I_zS_y) + T_{zx}(I_zS_x + I_xS_z) \quad [2.18]$$

where the coefficients are defined as,

$$T_{ii} = \frac{\mu_o}{4\pi} g\beta\, g_N\beta_N \left\langle \frac{r^2 - 3i^2}{r^5} \right\rangle \text{ and } T_{ij} = -\frac{\mu_o}{4\pi} g\beta\, g_N\beta_N \left\langle \frac{3ij}{r^5} \right\rangle \qquad [2.19]$$

The angular brackets denote average taken over the electronic wave function, since the electron is not fixed in space. Equation 2.18 can be written in the matrix form as: $\mathcal{H}_{dipolar}$ = **I** · **T** · **S**, the anisotropic hyperfine coupling tensor **T** is traceless and symmetric with elements T_{ij}. The hyperfine interaction matrix **A** can be defined as a combination of isotropic and anisotropic hyperfine couplings,

$$\mathbf{A} = A_{iso}\,\mathbf{1} + \mathbf{T} \qquad [2.20]$$

where trace of **A** , Tr{**A**} = 3 A_{iso}.

Information about the geometry of the paramagnetic system, the unpaired electron spin density and molecular wavefunctions can be obtained from the hfi tensor. When the molecular motion is fast, as in the case of molecules with low viscosity or at high sample temperature, the anisotropic hyperfine interaction averages to zero.

II.1.4 Nuclear quadrupole interaction

The nuclear quadrupole interaction is an electrostatic interaction between the quadrupole moment of the nucleus and the electric field gradient at the nucleus due to the surrounding electronic charges in an atom or molecule. A nucleus with a nuclear quantum number I = 1/2 has one net unpaired spin, which imparts a nuclear magnetic moment to the nucleus. The distribution of charge in such a nucleus is spherical. When I ≥ 1, a nucleus has an electric moment along with the magnetic moment and the distribution of nuclear charge is non-spherical. Such a nucleus has a quadrupole moment eQ, where e is

the charge on an electron and Q is a measure of deviation of nuclear charge distribution from spherical symmetry. In systems that are studied using EPR spectroscopy, a charge cloud of electron surrounds the nucleus and an inhomogeneous electric field can result from asymmetry in the electron distribution and electronic structure of the paramagnetic species. In such a case, the quadrupole moment will interact with the resulting electric field gradient and affect the electron spin energy states via electron-nuclear magnetic coupling.

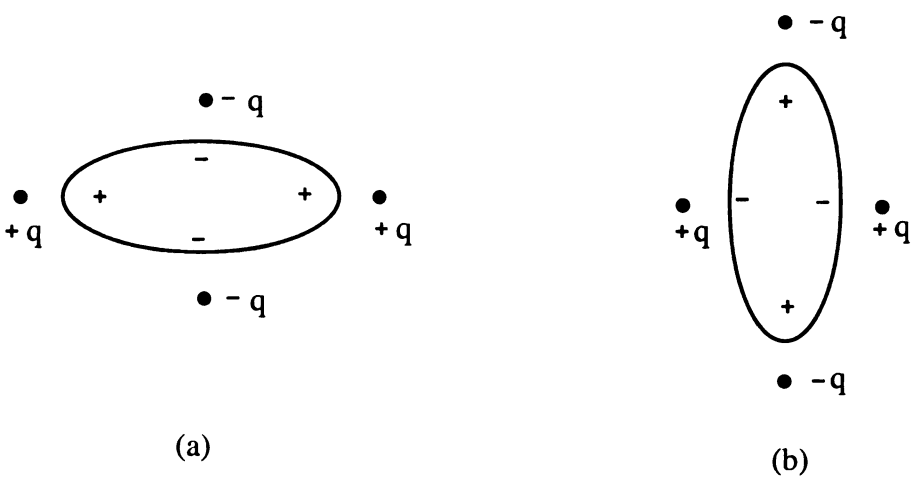

Figure II-5: Interactions of a quadrupolar nucleus with four point charges, the orientation in (b) is of lower energy and is preferred over (a).

The quadrupolar moment acts to orient the nucleus in the direction of the largest electric field gradient (figure II-5). When the magnetic field axis and the crystal axis are parallel, the effect of quadrupolar interaction is to displace all the energy levels by a

constant amount, which produces no change in the observed transitions. However, when the two axes are not parallel, there is a competition between the electric field and the magnetic field and it manifests itself in the EPR spectrum. Since, the axis of quadrupole moment and the nuclear spin angular momentum are collinear, the Hamiltonian for the quadrupole interaction can be described in terms of the nuclear spins as,

$$\mathcal{H}_{NQI} = \kappa [3 I_z^2 - I^2 + \eta(I_x^2 - I_y^2)], \qquad [2.21]$$

where $\kappa = e^2qQ/4$, is the quadrupole coupling constant, η is the asymmetry parameter defined in terms of the principal values of the diagonal and traceless electric field gradient tensor as,

$$\eta = |V_{xx} - V_{yy}|/V_{zz}$$

The nuclear quadrupole interaction is discussed further in section IV-4.1.

II.1.5 Zero field interaction

The magnetic dipole-dipole interaction between two unpaired electrons can remove the degeneracy of the electron spin energy levels in the absence of external magnetic field and is called zero field interaction. In transition metal ion systems (with $S \geq 1$), this term is used to explain any effect that removes the spin degeneracy, including dipolar spin-spin interactions and spin-orbit coupling. Experimentally it is not possible to separate the contributions of these two effects to the zero field splitting tensor **D**. The zero field Hamiltonian has the form,

$$\mathcal{H}_{zfs} = \hat{\mathbf{S}} \cdot \mathbf{D} \cdot \hat{\mathbf{S}}$$

$$= D_{xx}\hat{S}_x^2 + D_{yy}\hat{S}_y^2 + D_{zz}\hat{S}_z^2$$

$$= D[\hat{S}_z^2 - \tfrac{1}{3}S(S+1)] + E(\hat{S}_x^2 - \hat{S}_y^2) + \tfrac{1}{3}(D_{xx} + D_{yy} + D_{zz})S(S+1) \qquad [2.22]$$

where $D = D_{zz} - (D_{xx} + D_{yy})/2$ and $E = (D_{xx} - D_{yy})/2$. The last term in [2.22] is a constant, which shifts all the components of the ground state equally. The coefficient of this term is proportional to the trace of **D**. This term is usually not included in the spin Hamiltonian as it is zero for pure spin-spin coupling. This is discussed further in section V-5.

II.1.6 Relaxation effects

At thermal equilibrium, the relative populations in the electronic energy levels are given by the Boltzmann distribution,

$$n_\alpha/n_\beta = e^{-\Delta E/kT}, \qquad [2.23]$$

where n_α and n_β are the populations of the upper (α) and lower (β) energy levels involved in an EPR transition, k is the Boltzmann constant and T is the temperature of the sample. Electrons being Fermions obey Fermi-Dirac statistics, but when interactions between electron spins are weak, then Boltzmann statistics can be applied to them. This ratio decreases and the difference in population of two levels increases with decreasing T. Hence, resolution is expected to improve upon lowering the temperature of the sample. A population difference between the energy levels allows the absorption of microwave radiation. In the absence of any relaxation mechanism by which the electron in the higher energy spin states can decay back to the lower state, absorption of microwave radiation

followed by EPR transitions would lead to saturation. But, there are many possible paths that can lead to spin relaxation. Spins interact with the applied field and with each other. Thermal motion causes these interactions to fluctuate and a spin experiences a randomly fluctuating magnetic field. Thus, there is always an oscillating field present with the right frequency and orientation to induce a transition leading to relaxation. The major contribution to the energy of the spin system comes from the Zeeman energy defined by equation 2.4. Major changes in the energy of the spin system due to thermal fluctuations may therefore be brought by changes in the z-component of magnetization M_z. The relaxation of M_z, the component parallel to the external field, is called longitudinal or spin lattice relaxation and its characteristic time constant (T_1) is called spin lattice relaxation time constant, as it is connected with the exchange of energy between the spin system and the lattice in which the dipoles are embedded. Quantitatively, T_1 is the time required for the longitudinal magnetization (M_z) to decay to 1/e of its equilibrium value M_0 after the mw pulse is turned off. The mutual interactions between the dipoles do not affect the total energy of the system, so in presence of external magnetic field, which is much larger than the local fields, they do not affect the longitudinal component but only affect the transverse components M_x and M_y. This relaxation effect is called spin-spin relaxation or transverse relaxation. The transverse relaxation time T_2 is the decay time of the transverse components of magnetization. Both spin-lattice and spin-spin interactions lead to broadening of the EPR signal. Spin-spin interaction varies as a function of $(1 - \cos^3\theta)/r^3$, where r is the distance between spins and θ is the angle between the field and the symmetry axis of the system. Hence, this broadening effect can be reduced by diluting the sample. The effect of spin-lattice relaxation can be minimized by

decreasing the sample temperature. Various other effects such as electron spin exchange, rapid chemical processes, electron transfer between a radical and a diamagnetic species can also cause line broadening. The EPR lineshape can be Lorentzian or Gaussian depending on the lifetimes of the spin states, for shorter lifetimes it is Lorentzian and for lifetimes long enough for the spins to experience different local field for different spins, the shape is Gaussian.

II.1.7 Information available from cw-EPR

EPR is a highly sensitive technique for detecting paramagnetic species and can provide information about electronic spin state, electronic and spatial structure and internal dynamics of the system under study. One major advantage of EPR is its extreme sensitivity to very small amounts of paramagnetic materials. EPR experiments can be performed on a variety of systems including gases, solutions, powders, frozen solutions, single crystals, complex biological systems and polymeric matrices having unpaired electrons. The main information gained from an EPR spectrum is an estimate of the various terms in the spin Hamiltonian as discussed above. If the spectral features are well resolved, then the Zeeman and hfi parameters can be found directly from EPR spectrum. In order to extract maximum information from EPR spectra of a particular system, spectra are collected at several frequencies and temperature. It is possible to identify an unknown ion or lattice defect and to distinguish between several states of the same ion. Considerable information can be obtained about the nuclei in the immediate neighborhood of the absorbing spin. Sometimes data on relaxation times can provide information about long-range effects. Diffusion constants, correlation times and the type of hydration can

be in principle determined from the EPR spectra of solutions. Chemical bonds in molecules and crystal may be sometimes characterized by EPR studies. The concentration of paramagnetic species may be determined. Detailed information about ferromagnetic, antimagnetic and ferrimagnetic materials may be obtained.

Conventional cw-EPR experiment is performed at fixed microwave frequency and the magnetic field is varied to adjust the energy level splitting to the energy of the microwave quantum. Two commonly used frequencies fall in the range of X-band (8.2-12.4 GHz) and Q-band (33-50 GHz). The sensitivity of the instrument is proportional to the square of the microwave frequency and resolution is expected to improve with an increase in frequency, but there are several limitations on the use of higher frequencies. With the increase in frequency the sample size decreases, so sensitivity is not as much greater as predicted from ν^2. It is more difficult to attain higher field homogeneity ($\delta B_o/B_o$) that is required at higher frequencies. For aqueous samples, dielectric absorption by solvents becomes more serious as the frequency increases and results in decreased sensitivity. Water, alcohols and other high dielectric constant solvents strongly absorb microwave power. They can be used when the samples have strong resonance and are contained in very narrow sample tubes. The best frozen solution results are obtained when the solvent freezes to form a glass; otherwise, paramagnetic aggregates form, which lead to a spectrum with broadened lines. Ethylene glycol is often used for this purpose. The sample tube employed is also important. A quartz tube is preferred, because pyrex absorbs more microwave power and also exhibits an EPR signal.

The main limitation of EPR is the linewidth changes, which may occur over a range of approximately 1 ns to 1 μs. In case of randomly ordered samples EPR spectra

are often inhomogeneously broadened and it becomes normally impossible to measure the hyperfine splittings. The inhomogeneity in the cw-EPR line is caused when the unpaired electrons in different free radicals in the sample experience slightly different effective magnetic fields at a given time and hence only a fraction of the spins meets the resonance condition as the magnetic field is swept. The experimentally observed EPR line is then a superposition of contributions from a large number of individual components called spin packets, each slightly shifted from the others. A spin packet is a collection of spins with individual spin magnetic moments having same Larmor frequencies but different phases. The inhomogeneity in the effective field at the electron can arise from inhomogeneous magnetic field or from anisotropic g and hfi interactions that give rise to a distribution of local magnetic fields. Hence, a need arises to find a method with the ability to resolve these unresolved hf splittings.

II.2 Pulsed EPR

Electron Spin Echo Envelope Modulation (ESEEM) Spectroscopy is one of the most useful methods of pulsed EPR. It is a low-temperature, time-domain EPR technique used for structural determination in paramagnetic systems and is based on the electron spin echo (ESE) phenomenon. It enables the measurement of weak electron-nuclear hyperfine couplings that remain unresolved in cw-EPR due to inhomogeneous broadening of the EPR lineshape. In this method, the time evolution of the spin system is recorded directly, which allows observation of individual spin packets and hence overcomes the problem of inhomogeneous broadening. The paramagnetic sample is studied in a constant magnetic field and is subjected to a series of resonant microwave pulses of varying

duration (in nsec range) and power, separated by evolution times, periods when the microwave pulse is off. Application of a refocusing pulse reverses dephasing due to inhomogeneity and the spin packets refocus resulting in the formation of a spin echo. The integrated intensities of electron spin echoes are then measured as a function of time intervals between pulses. The variation in amplitude or modulation of the spin echo amplitude is used to measure splittings that are too small to be resolved in the inhomogeneously broadened EPR line. This method makes it possible to separate the dephasing arising due to inhomogeneity from the decay of magnetization due to spin-spin relaxation. The two most common methods of ESEEM experiment are commonly referred to as two-pulse and three-pulse techniques.

II.2.1 Two-pulse ESEEM spectroscopy

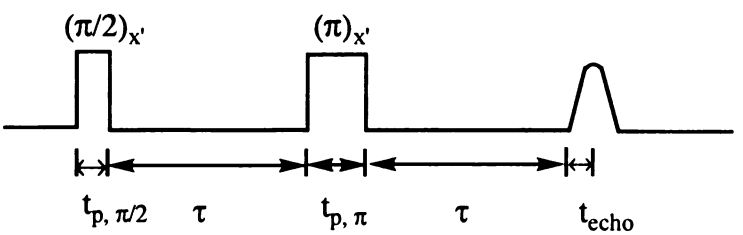

Figure II-6: The pulse scheme used in a two pulse ESEEM experiment.

Figure II-6 shows the pulse scheme used in a two-pulse ESEEM experiment to generate the spin echo. The pulsed method of EPR has been discussed in various articles

in great detail.[2,4,5,9,10] The formation of the spin echo and the basis of two-pulse and three-pulse ESEEM methods are briefly discussed below.

II.2.1.1 Formation of Electron Spin Echo (ESE)

In the presence of a static external field ($\mathbf{B_0}$) spins precess around the axis of $\mathbf{B_0}$ with angular frequency ω_0 (section II.1.1) and a net or equilibrium magnetization **M** associated with electron spins is along $\mathbf{B_0}$. Because an EPR transition involves a change in the orientation of the electron spin, the optimal direction for the magnetic field ($\mathbf{B_1}$) of the mw pulse is most often perpendicular to $\mathbf{B_0}$. This time-dependent field can be represented as,

$$\mathbf{B_x}(t) = 2\,\mathbf{B_1}\cos(\omega t) \qquad [2.24]$$

where ω is the carrier frequency of the mw pulse. The effect of this field can be analyzed by decomposing it into two rotating components, $\mathbf{B_r}$ and $\mathbf{B_l}$, each of magnitude B_1, one rotating clockwise and the other counterclockwise in the plane of $\mathbf{B_1}$.

$$\mathbf{B_r}(t) = B_1\,[\mathbf{i}\cos(\omega t) + \mathbf{j}\sin(\omega t)], \qquad [2.25]$$

$$\mathbf{B_l}(t) = B_1\,[\mathbf{i}\cos(\omega t) - \mathbf{j}\sin(\omega t)] \qquad [2.26]$$

One of these components will rotate with frequency ω in the same direction as the electron spins (section II.1.1). The other component will have a frequency -2ω and at resonance when $\omega = \omega_0$, this component will have little effect, so it may be neglected. The time dependence of $\mathbf{B_1}$ can be removed by introducing a coordinate system x'y'z, rotating about the axis of $\mathbf{B_0}$ at an angular frequency ω.[11] Hence, in the rotating frame, $\mathbf{B_1}$

is a stationary field and is defined along x'-axis, $\mathbf{B_1} = B_1\mathbf{i}$. The magnetization **M** appears to precess about $\mathbf{B_o}$ at a frequency $(\omega_o - \omega)$ which is the Larmor frequency corresponding to a field of magnitude $(\omega_o - \omega)/\gamma = (\omega_o - \omega)/(\omega_o/B_o)$. Thus **B** is given by,

$$\mathbf{B} = B_1\mathbf{i} + (\omega_o - \omega)\, B_o/\omega_o\mathbf{k} \qquad [2.27]$$

The magnitude of this field is,

$$B = [B_1^2 + ((\omega_o - \omega)\, B_o/\omega_o)^2]^{1/2} \qquad [2.28]$$

and its direction is at an angle θ from z-axis defined by $\tan\theta = B_1\omega_o/(\omega_o - \omega)\, B_o$. In the presence of mw pulse, a torque acts on the magnetization according to the Bloch's equation,

$$d\mathbf{M_i}/dt = \gamma\, \mathbf{B_i} \times \mathbf{M_i}, \qquad [2.29]$$

where $\mathbf{B_i}$ is the effective static magnetic field experienced by spin packet 'i' and is the resultant of $\mathbf{B_1}$ and $\mathbf{B_o}$. B_{local} is negligible as compared to B_1 and B_o. The magnetization before and after the application of mw field is obtained from the solutions of the Bloch equations,

$$\frac{du}{dt} = +\gamma B_o v - v\omega - u/T_2$$

$$\frac{dv}{dt} = -\gamma B_o u + u\omega + \gamma M_z B_1 - v/T_2 \qquad [2.30]$$

$$\frac{dM_z}{dt} = -\gamma B_1 v + (M_o - M_z)/T_1$$

where u and v are the x'- and y'- components of the magnetization in the rotating frame and M_o is the magnetization at thermal equilibrium before the application of $\mathbf{B_1}$. If it is assumed that the mw pulse width (t_p) is sufficiently small, such that no appreciable decay of magnetization takes place during t_p and the field $B_1 >> B_o$ (in rotating frame), such that the effect of B_o can be neglected during the application of mw field, then the effective field experienced by the spin is just B_1 and the magnetization precesses about it at frequency $\omega_1 = \gamma B_1$. Under these conditions the above equations (2.26) reduce to,

$$\frac{du}{dt} = 0$$

$$\frac{dv}{dt} = \gamma M_z B_1 = \omega_1 M_z \qquad [2.31]$$

$$\frac{dM_z}{dt} = -\gamma B_1 v = -\omega_1 v$$

At the time t = 0, when the mw pulse is turned on, equilibrium magnetization M_o is along z-axis and the solutions of [2.31] are,

$$M_z = M_o \cos(\omega_1 t)$$

$$v = M_{y'} = M_o \sin(\omega_1 t) \qquad [2.32]$$

These equations [2.32] describe the rotation of magnetization in y'z-plane. When the pulse is turned off at $t = t_p$, the components of magnetization are,

$$M_z(t_p) = M_o \cos(\omega_1 t_p)$$

$$v(t_p) = M_{y'}(t_p) = M_o \sin(\omega_1 t_p) \qquad [2.33]$$

Thus the effect of the mw pulse is to turn the magnetization vector that was aligned along $\mathbf{B_o}$ by an angle θ_{flip}, given by $\theta_{flip} = \omega_1 t_p$. In ESE experiments, pulse widths are chosen to rotate the magnetization by some predetermined amount, for example, if width and magnitude of mw pulse are selected such that $\omega_1 t_p = \pi/2$, then the magnetization is flipped along y'-axis,

$$M_z(t_p) = 0$$

$$v(t_p) = M_{y'}(t_p) = M_o \qquad [2.34]$$

Due to inhomogeneity in the external and internal magnetic fields, there will be a distribution of precessional frequencies of spin packets around the central frequency ω_o. Since these spin packets have different offset frequencies they start dephasing immediately after the pulse. This is called Free Induction Decay (FID). The dead time of the instrument is usually too large for the FID signal to be detectable. From this FID, however, an echo called primary echo, can be generated by means of a second mw π-pulse ($\omega t_p = \pi$) along x'-axis, applied at time τ after the first pulse. With the same mw field its pulse width would be twice that of the $\pi/2$-pulse. The π-pulse torques the magnetization vector by 180° about x'-axis. The original precession frequencies and direction of precession remain unchanged and all the magnetization vectors align along the -y' direction at time τ after the second pulse to build up a 'spin echo' which is detected. For any length of pulses an echo is generated, but maximum echo intensity is obtained with a $\pi/2$-π sequence of pulses.

II.2.1.2 The nuclear modulation effect

The unpaired electron can have anisotropic hyperfine interactions with the surrounding magnetic nuclei and the NMR transition frequencies can be observed as modulations on the ESE decay curve (figure II-7). The dipolar field from unpaired electron spin ($\sim \mu_e/r^3$) can be a significant part of B_o, for example, it is about 350 G for r = 3 Å (figure II-4). The dipolar field from a nucleus is much smaller, less than 1 G for r > 2.5 Å. However, the dipolar field from a nucleus experienced by the electron varies with time due to the precession of nuclear spin. This leads to modulation of the electron Larmor frequency at the nuclear Larmor frequency. For the simplest case of a spin system consisting of an unpaired electron coupled to a single nucleus with I = 1/2, the energy level diagram consists of four levels as shown in figure II-8. For a totally isotropic case only the allowed transitions labeled $1\leftrightarrow3$ and $2\leftrightarrow4$ would occur, but the presence of an anisotropic hfi of the same magnitude as the nuclear Zeeman coupling may lead to mixing of the nuclear states. As a result, the "forbidden" transitions, $1\leftrightarrow4$ and $2\leftrightarrow3$ may also occur to some extent. If the short mw pulse covers the frequency range corresponding to these transitions then all four transitions will occur simultaneously.

The formation of ESE in a two-pulse experiment can be seen pictorially in figure II-9. After the first $\pi/2$-pulse the electron spins "s_{13}", "s_{24}" from allowed transitions and "s_{14}", "s_{23}" corresponding to forbidden transitions will be in the x'y'-plane, here "s_{ij}" represents spins undergoing transition $i\leftrightarrow j$. As $\omega_{13}, \omega_{23} < \omega$, so s_{13} and s_{23} will make negative angles with respect to y-axis and $\omega_{24}, \omega_{14} > \omega$, so s_{24} and s_{14} will make a positive angle with respect to y-axis, ω_{ij} represents the angular frequency of the spin s_{ij} and ω is the angular frequency of rotating frame. Since $\omega_{14} > \omega_{24}$, so s_{14} will be ahead of s_{24} and

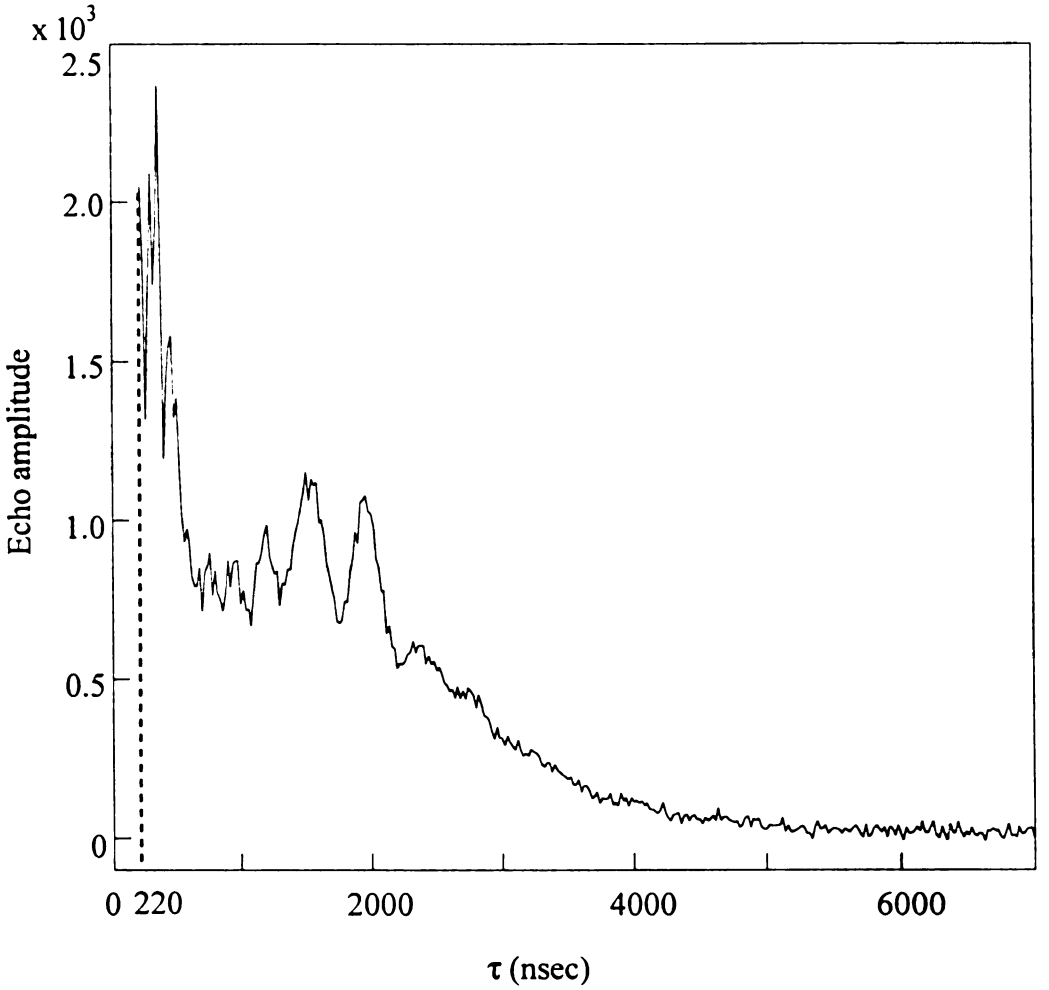

Figure II-7: Two-pulse time domain ESEEM data, dead time = 220nsec.

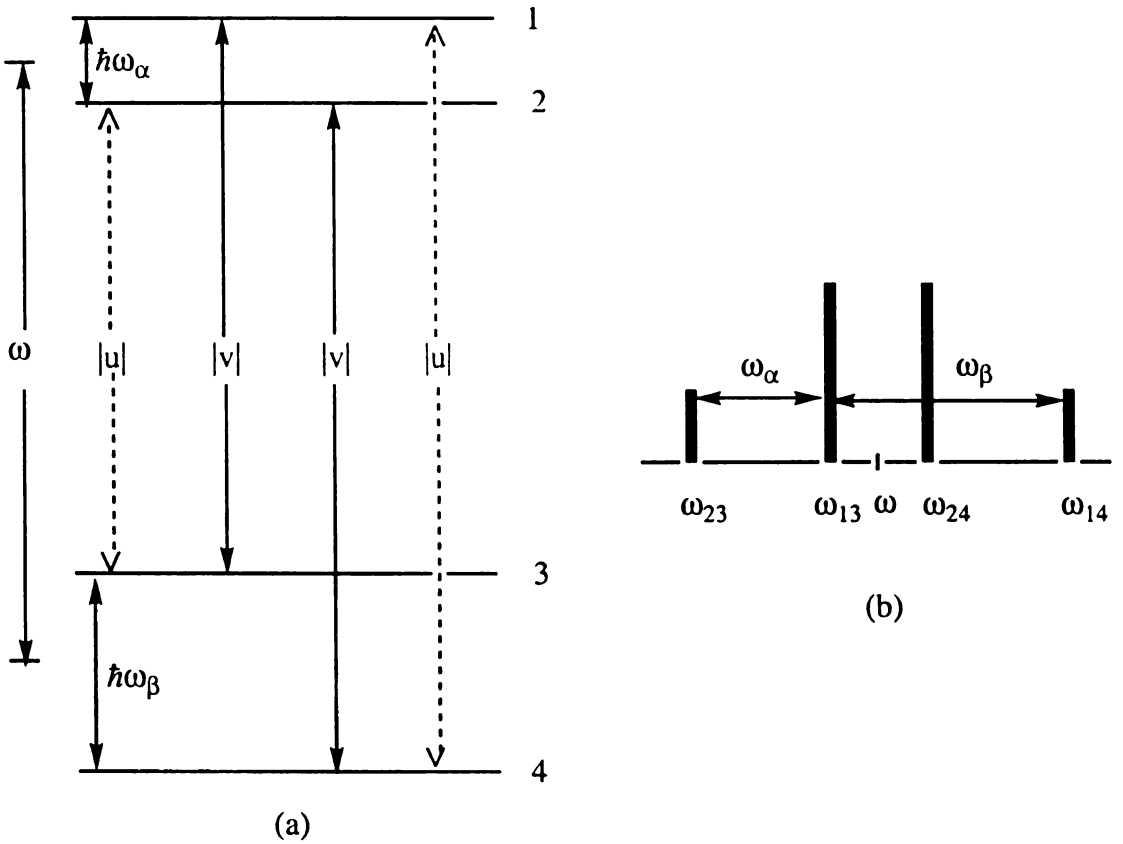

Figure II-8: Energy-level diagram for the interaction of an unpaired electron (S = 1/2) and a nucleus with I = 1/2.

Figure 9: Vector diagram showing the formation of electron spin echo as a result of a 90°-τ-180° mw pulse sequence in a two pulse ESEEM experiment. (a) at thermal equilibrium the net magnetization **M** is aligned with the external magnetic field $\mathbf{B_0}$; (b) as a result of first 90° mw pulse, **M** is torqued onto the **x'y'**-plane of the rotating frame; (c) the spin packets that constitute **M** start to dephase due to difference in their precession frequencies; (d) the second 180° pulse applied along **x'**, flips the spin packets about **x'**, while the direction of precession of individual spin packets remains unchanged. This pulse also introduces branching of transitions; (e) the individual spin packets refocus to form an spin echo along **-y'**.

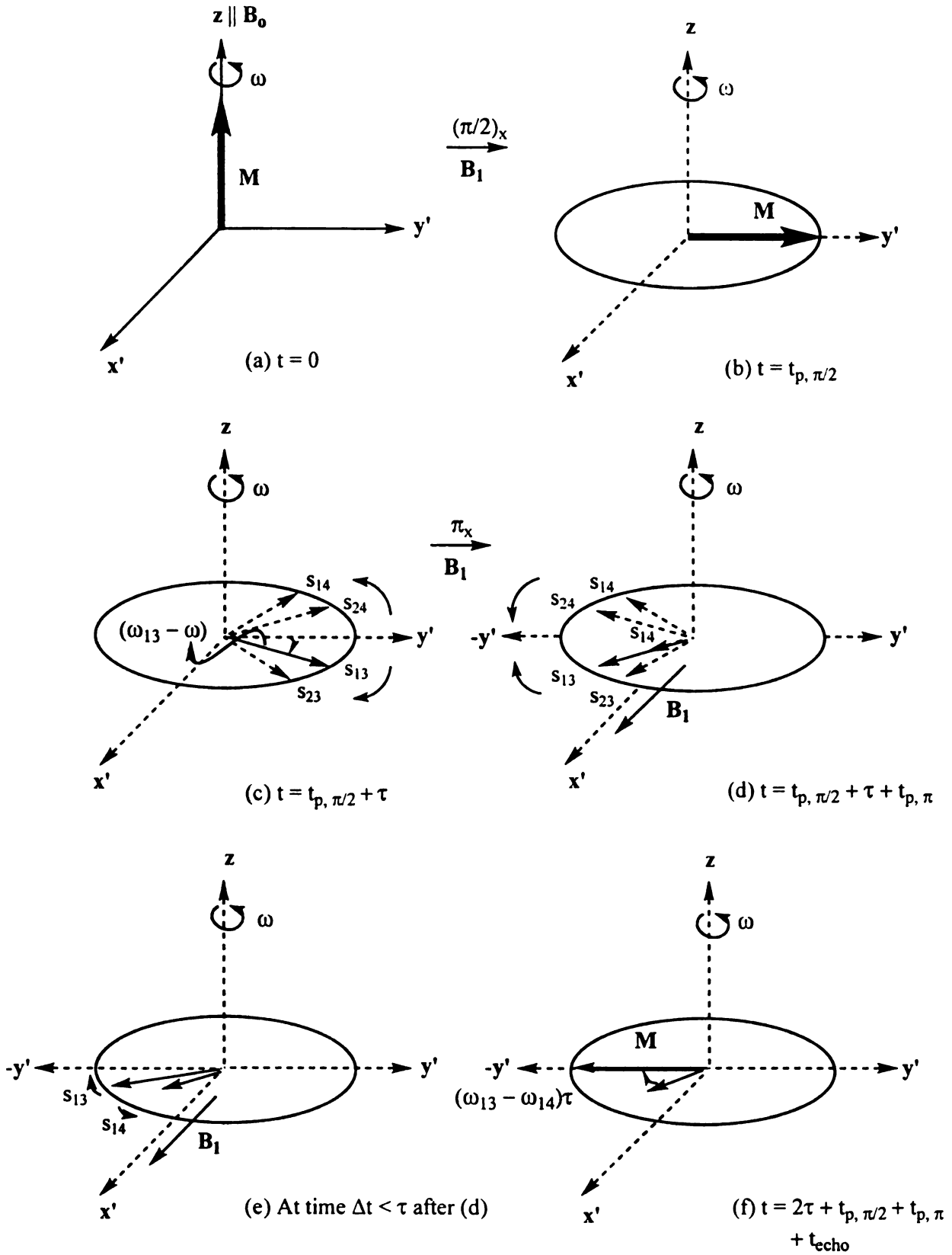
z || B0
ω
M
y'
x'
(a) t = 0
(π/2)x
B1
z
ω
M
y'
x'
(b) t = tp, π/2
z
ω
S14
S24
(ω13 − ω)
y'
S13
S23
x'
(c) t = tp, π/2 + τ
πx
B1
z
ω
S14
S24
-y'
S14
y'
S13
S23
B1
x'
(d) t = tp, π/2 + τ + tp, π
z
ω
-y'
y'
S13
S14
B1
x'
(e) At time Δt < τ after (d)
z
ω
M
-y'
y'
(ω13 − ω14)τ
x'
(f) t = 2τ + tp, π/2 + tp, π + techo

will make greater angle with y'-axis and appear to move clockwise in the rotating frame as shown in figure II-9(c). Similarly, $\omega_{23} < \omega_{13}$, so s_{23} will lag behind s_{13}. In order to understand the effect of pulses on the spin packets, we focus on one of the spin packet s_{13} (solid arrow). After the first free precession period τ, this packet would make a negative angle of $(\omega_{13} - \omega)$ with respect to the x'-axis. The effect of the 180° pulse is to flip the packet s_{13} by 180° about x'-axis and to introduce two possible transitions, level 1 to 3 and another from 1 to 4. Thus, the spin packet s_{13} is split into a packet s_{14} that will now precess at ω_{14}, (figure II-9d). This is termed as 'branching of transitions'. As $\omega_{14} > \omega > \omega_{13}$, this new packet s_{14} will precess in the direction opposite to s_{13} from which it is split, (figure II-9e). After the second free precession period τ after the π-pulse, s_{13} will refocus to form an echo along -y'-axis, however, at this time s_{14} will make certain angle with the -y' axis and thus, will not contribute fully to the echo, (figure II-9f). The contribution of the component s_{14} to the echo will be equal to its projection on the -y' axis, $\cos\{(\omega_{13} - \omega_{14})\tau\}$, weighted by the probability of branching. Thus, the interference is modulated with a frequency of $(\omega_{13} - \omega_{14}) = \omega_\beta$, as τ is varied. Its contributions will be maximum if, $(\omega_{13} - \omega_{14})\tau = n\,2\pi$, i.e. when it precesses an integral number of times in time τ, in the rotating frame. In the above treatment it is assumed that the spin-lattice relaxation time $T_1 >> \tau$, such that there is no build up of the longitudinal component of the magnetization (M_z) during the time τ, i.e. $M_z = 0$. The spin-spin relaxation time (T_2) is of the order of few μsec, whereas τ is typically few hundred nsec or few tenth of a μsec so, the decay of transverse magnetization is not complete when the second π-pulse is applied. The requirement on mw pulse length is that it should be shorter than the shortest modulation period to be observed and the mw field B_1 must be large enough such

that γB_1 is larger than the nuclear frequencies ω_α and ω_β. If B_1 is too small the branching of transitions will not occur. This can sometimes be useful when different kind of nuclei with quite different nuclear frequencies are coupled to the electrons. It may be possible to vary B_1 such that branched transition for only one nucleus is excited this would suppress the modulations from the other nuclei.

The theory behind pulsed methods can be described by using density matrix formalism.

II.2.1.3 Density matrix formalism

In quantum mechanics the expectation value of an observable depends on the state, Ψ of the system. Various members of an ensemble can be in different states, and any bulk property (O) measured is an average of various expectation values i.e.,

$$\overline{\langle O \rangle} = \overline{\langle \Psi(t) | O | \Psi(t) \rangle} \qquad [2.35]$$

Thus, knowledge about the exact state of the system is a prerequisite for measuring a bulk property. The density matrix formalism provides a means for calculating properties of ensembles within the framework of the wavefunctions describing the state of the microscopic spin system that comprises the ensemble's fundamental element. The calculation involves solving the equation of motion of density matrix rather than solving the Schrödinger equation. Since in ESEEM experiments one studies an ensemble of spins, density matrix formalism can be used to describe these experiments. There are several articles that describe density matrix[1,12-15] and its use in magnetic resonance.[2,16] A brief

description of the use of this method for deriving the modulation formula for two-pulse ESEEM experiment will be presented in this section.[5]

The density operator ρ describes the projection of one basis set onto another. It has the form,

$$\hat{\rho}(t) = |\Psi(t)\rangle\langle\Psi(t)|, \qquad [2.36]$$

where $\Psi(t)$ is the wavefunction describing the state of the system. As any state of a system can be expanded in terms of a complete set of orthonormal functions $|\phi_k\rangle$ with coefficients $c_k(t)$, so $\Psi(t)$ can be expressed as,

$$\Psi(t) = \sum_k c_k(t)\,|\phi_k\rangle \qquad [2.37]$$

and the density matrix has the elements

$$\rho_{ij} = \langle\phi_i\,|\rho(t)|\phi_j\,\rangle \qquad [2.38]$$

So, the density matrix has different forms in different representations but the density operator $\rho(t)$ is independent of the choice of basis states. Using equations 2.36-2.38 to simplify 2.35, it can be shown that,

$$\overline{\langle O\rangle} = \text{Trace}\{\rho(t)O\} \qquad [2.39]$$

$\rho(t)$ can be found by solving the equation of motion of the density matrix,

$$\frac{d}{dt}\rho(t) = \frac{i}{\hbar}[\rho(t), \mathcal{H}(t)] \qquad [2.40]$$

where $\mathcal{H}(t)$ is the time-dependent Hamiltonian and the square brackets represent the commutator of ρ and $\mathcal{H}$. On integration [2.40] gives the solution for density matrix $\rho(t)$ at time t, in terms of its initial value $\rho(0)$ at time zero,

$$\rho(t) = e^{-i\mathcal{H}t/\hbar}\,\rho(0)\,e^{i\mathcal{H}t/\hbar} \qquad [2.41]$$

In the case of spin echo experiment the evolution of the spin states during the periods of nutation, when the mw pulse is on, and free precession, when the mw pulse is off, can be followed by density matrix formalism. Figure II-10 shows a set of energy levels and transitions involved in the formation of spin echo. $|\alpha\rangle$ and $|\beta\rangle$ are two electron spin states and the spread in α and β levels is due to hyperfine structure and inhomogeneity.

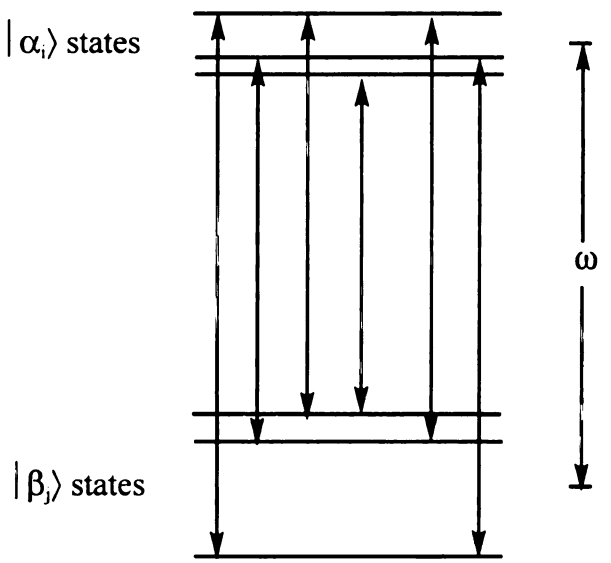

Figure II-10: Energy-levels of a quantized system and transitions giving rise to spin echo. $|\alpha\rangle$ and $|\beta\rangle$ are two electron spin states. Only those levels of the over-all quantized system for which the transition $|\alpha_i\rangle \leftrightarrow |\beta_j\rangle$ has a significant amplitudes are shown.

The evolution of α and β states during period of nutation and the free precession period can be followed by using eq. 2.36. The Hamiltonian $\mathcal{H}(t)$ consists of a time-independent part $\mathcal{H}_o$ describing electronic Zeeman, nuclear Zeeman, electron-nuclear hyperfine, nuclear quadrupole, zero field interactions etc. during the free precession period and a time-dependent part $\mathcal{H}_1$ that describes the interaction of the spins with the resonant mw field during the period of nutation.

$$\mathcal{H}(t) = \mathcal{H}_o + \mathcal{H}_1(t), \qquad [2.42]$$

$$\mathcal{H}_o = \mathcal{H}_{e\text{-}Zeeman} + \mathcal{H}_{nuc\text{-}Zeeman} + \mathcal{H}_{hfi} + \mathcal{H}_{nqi} + \mathcal{H}_{zfs} + \ldots \qquad [2.43]$$

$$\mathcal{H}_1(t) = \hbar\omega_1 S_x \cos\omega_1 t \qquad [2.44]$$

$$= \hbar\omega_1 S_x \text{ (in rotating frame)}$$

B_o can be neglected during the mw pulses since the pulse energy $g\beta B_1$ is much larger than the nuclear Zeeman or hfi energies. It might not be a reasonable assumption for longer pulses (smaller B_1) and for nuclei closer than ≈ 3Å (stronger hfi). This assumption is useful in obtaining simple equations for the echo modulation and some discrepancies between simulations and experiment may be associated with the partial failure of this assumption. The mw pulse width is assumed sufficiently small such that it has sufficient energy to excite all the transitions simultaneously and the effect of relaxation during the pulses is negligible. The decay of echo due to spin relaxation can also be neglected during the periods of evolution, because the total echo as a function of time can be written as a product of a decay function and the echo modulation function,

$$f_{echo} = f_{decay}\, f_{mod} \qquad [2.45]$$

The decay function is of the form $\exp-(t/\tau_o)^n$, where $\tau_o \approx T_2$ is of the order of μsec and leads to a rapid background decay and is responsible for the reduction of frequency resolution in two-pulse experiment. The modulation function f_{mod} can be obtained as described by W. B. Mims[5] using the density matrix formalism. The density matrix $\rho(2\tau)$ at the time of appearance of spin echo is time-dependent so, $Tr\{\rho\mathcal{H}\}$ will depend only on the time-dependent part of $\mathcal{H}$ given by [2.44] and can be found using equation 2.41. The echo signal can then be determined as the expectation value of the $\mathbf{M_y}$ component of the magnetization,

$$E = \eta\ Tr\{\rho_{echo}\mathcal{H}_1\} \qquad [2.46]$$

where η is a constant of proportionality that depends on experimental parameters, ρ_{echo} is the density matrix of the spin system at the time when the maximum echo appears and $\mathcal{H}_1$ is the time-dependent Hamiltonian describing the interaction of the spin system with the microwave pulse. The evaluation of equation [2.46] requires two summations to be performed: a sum over all $|\alpha_i\rangle$ and $|\beta_j\rangle$ states involved in the branching of transition for each quantized system and a sum over all the individual systems that make up the inhomogeneous line. $\mathcal{H}_o$ will have a spread $\Delta\mathcal{H}_o$ about a mean value $\mathcal{H}_{o,av}$ due to inhomogeneity,

$$\mathcal{H}_{o,k} = \mathcal{H}_{o,av} + \Delta\mathcal{H}_{o,k} \qquad [2.47]$$

Provided $\Delta\mathcal{H}_{o,k}$ is large compared to the spread within α and β manifolds, the two summations can be factorized. The first sum would give the envelope-modulation function and the second sum, the form of the spin-echo signal. It is assumed that $\Delta\mathcal{H}_{o,k}$ only affects the spacing between α and β levels but does not contribute towards

inhomogeneous spread within each manifold. During the free precesion periods $\mathcal{H}$ is time-independent and $\rho(t_f)$ at the end of the pulse can be found in terms of the density matrix, $\rho(t_i)$ at the start of the free precession period using equation 2.37. In the eigenvalue basis, $\rho(t_i)$ and $\mathcal{H}_o$ are diagonal and at the end of the free precession period the off-diagonal elements are multiplied by phase factors exp-$i(\omega_{\alpha i} - \omega_{\beta j})(t_f - t_i)$, where $\omega_{\alpha i}$ and $\omega_{\beta j}$ are the nuclear frequencies in α and β electron spin manifolds respectively. During the periods of nutation, the spin system interacts with the time-dependent oscillating mw field and the Hamiltonian can be written as,

$$\mathcal{H}_1(t) = \mathcal{H}_{\mathcal{N}}(e^{i\omega t} + e^{-i\omega t}) \qquad [2.48]$$

where ω is the frequency of the mw field and $\mathcal{H}_{\mathcal{N}}$ is a time-independent Hermitian operator that connects α states with β states, but does not connect states within α or β manifolds. In order to describe evolution of the spin system under the influence of mw pulses, $\exp(\pm i\omega_1 S_x t)$ should be expressed in the eigenvalue basis. This matrix consisting of states $|\alpha_i\rangle$ and $|\beta_j\rangle$ can be divided into four sub-matrices with $\alpha_i\alpha_i$, $\alpha_i\beta_j$, $\beta_j\alpha_i$ and $\beta_j\beta_j$ as their matrix elements,

$$\mathcal{H}_1 = \begin{array}{c|cc} & |\alpha_i\rangle & |\beta_j\rangle \\ |\alpha_i\rangle & 0 & \mathcal{H}_{\mathcal{N}} e^{-i\omega t} \\ |\beta_j\rangle & \mathcal{H}_{\mathcal{N}}^{\dagger} e^{i\omega t} & 0 \end{array} \qquad [2.49]$$

The time dependency of $\mathcal{H}_1$ can be removed by a similarity transform that is equivalent to introducing a new frame of reference rotating about z-axis at angular frequency ω,

$$\mathcal{H}_1 = \exp(i\sigma_z\omega t/2)\, \mathcal{H}_1 \exp(-i\sigma_z\omega t/2) \qquad [2.50]$$

where σ_z is a Pauli matrix of dimension $(2I+1)\times(2I+1)$ for rotation about z-axis. Then,

$$\mathcal{H}_1 = \begin{array}{c|cc} & |\alpha_i\rangle & |\beta_j\rangle \\ \hline |\alpha_i\rangle & 0 & \mathcal{H}_N \\ |\beta_j\rangle & \mathcal{H}_N^{\dagger} & 0 \end{array} \qquad [2.51]$$

In this rotating frame, $\mathcal{H}_o$ and ρ can be found by similar transformations,

$$\mathcal{H}_o = \exp(i\sigma_z\omega t)/2\, \mathcal{H}_o \exp(-i\sigma_z\omega t)/2 \qquad [2.52]$$

$$\rho = \exp(i\sigma_z\omega t)/2\, \rho \exp(-i\sigma_z\omega t)/2 \qquad [2.53]$$

The final density matrix can be obtained by similarity transformations as,

$$\rho_{echo}(t) = R^{-1}\, \rho_{echo}(0)\, R \qquad [2.54]$$

where $R = R_{tpI}\, R_\tau\, R_{tpII}\, R_\tau$, R_{tpI} and R_{tpII} are the exponential operators for the first and second period of nutation and R_τ is the exponential operator during the free precession period. The time 't' in figure II-6 is approximately $t_p/2$ and is neglected.

$$R_{tpI} = \exp[i(\mathcal{H}_o + \mathcal{H}_1)t_{pI}/\hbar]$$

$$R_{tpII} = \exp[i(\mathcal{H}_o + \mathcal{H}_1)t_{pII}/\hbar] \qquad [2.55]$$

$$R_\tau = \exp[i\,\mathcal{H}_o\tau/\hbar]$$

Since $\mathcal{H}_o$ and $\mathcal{H}_1$ are Hermitian and R_{tpI}, R_{tpII}, and R_τ are unitary operators, so R^{-1} can be replaced by $R^{\dagger}$.

The modulation function for the two-pulse ESE can be obtained to be,

$$f_{mod}(\tau) = |u|^4 + |v|^4 + |u|^2|v|^2 \{2\cos(\omega_\alpha\tau) + 2\cos(\omega_\beta\tau) - \cos[(\omega_\alpha - \omega_\beta)\tau] - \cos[(\omega_\alpha + \omega_\beta)\tau]\} \quad [2.56]$$

where $|u|$ and $|v|$ are the normalized probability amplitudes for the forbidden and allowed EPR transitions as marked in figure II-8 and are defined as,

$$|u| = \langle 2|\hat{S}_x|3\rangle/0.5\omega_1 = \sin[(\varphi_\alpha - \varphi_\beta)/2] \text{and } |v| = \langle 1|\hat{S}_x|3\rangle/0.5\omega_1 = \cos[(\varphi_\alpha - \varphi_\beta)/2] \quad [2.57]$$

The angles, $\varphi_\alpha = \sin^{-1}[B/(2\omega_\alpha)]$ and $\varphi_\beta = \sin^{-1}[B/(2\omega_\beta)]$ define the axes of quantization for the α and β spin manifolds respectively. The nuclear frequencies $\omega_{\alpha i}$ and $\omega_{\beta j}$ are defined as,

$$\omega_\alpha = [(\omega_I - A/2)^2 + B^2/4]^{1/2}$$
$$\omega_\beta = [(\omega_I + A/2)^2 + B^2/4]^{1/2} \quad [2.58]$$

where A and B define the hyperfine coupling terms as,

$$A = A_{iso} + \frac{g\beta g_N \beta_N(3\cos^2\theta - 1)}{hr^3} \quad [2.59]$$

$$B = \frac{g\beta g_N \beta_N(3\cos\theta \sin\theta)}{hr^3} \quad [2.60]$$

The angle θ describes the orientation of the principal axis of the hyperfine tensor with respect to the external field $\mathbf{B_o}$. Thus, a two-pulse echo amplitude occurs at the fundamental nuclear frequencies, ω_α and ω_β, and also at their sum and differences, $(\omega_\alpha + \omega_\beta)$ and $(\omega_\alpha - \omega_\beta)$. The amplitude of modulation is proportional to square of the product of the transition probabilities, $|u|^2|v|^2$ of the classically allowed and forbidden transitions

associated with branching. The non-modulated portion of the echo depend on the individual transition probabilities, $|u|^4$ or $|v|^4$ for the two transitions. Substitution of equations [2.57] in [2.56] gives another form of echo modulation for the two-pulse experiment,

$$E_{mod}(\tau) = 1 - 0.5\,k\,\{1 - \cos(\omega_\alpha\tau) - \cos(\omega_\beta\tau) + 0.5\cos[(\omega_\alpha - \omega_\beta)\tau] + 0.5\cos[(\omega_\alpha + \omega_\beta)\tau]\} \qquad [2.61]$$

where $k = \sin^2(\varphi_\alpha - \varphi_\beta) = [\omega_I B/(\omega_\alpha\omega_\beta)]^2$ is called the modulation depth parameter, $\omega_I = g_N\beta_N B_o/\hbar$. For large depth parameters, the intensities of the combination lines can become substantial and may considerably complicate the ESEEM spectrum, especially at low mw frequencies. The modulation frequencies and depths reflect the hyperfine couplings between electrons and nuclear spins. In the presence of more than one nucleus contributing to the hfi, the ESEEM function is obtained by taking the product of the individual modulation functions as,

$$E(\tau) = f_{decay}\prod_{i=1}^{N} E^i_{mod}(\tau) \qquad [2.62]$$

where N is the number of coupled nuclei. Hence, in presence of many nuclei there will not only be fundamental and combination frequencies associated with each nucleus ($\Delta m_I = \pm 1$) but also combinations of frequencies arising from different nuclei. During time τ, the magnetization is in the xy-plane so, its relaxation is governed by spin-spin relaxation (of the order of μsec). As a result, the linewidth of two-pulse ESEEM peaks are severely broadened.

Figure II-11: Vector model showing the formation of electron spin echo in a three pulse ESEEM experiment. (a) pulse scheme; (b), (c) same events as in figure II-9; (d) the second 90° mw pulse along **x'** converts the transverse magnetization into longitudinal magnetization and the components start to dephase after the pulse is removed; (e) the third 90° mw pulse applied along **x'** rotates the magnetization components onto **x'y'** plane;(f) the spin packets refocus along **-y'** to give rise to a stimulated spin echo.

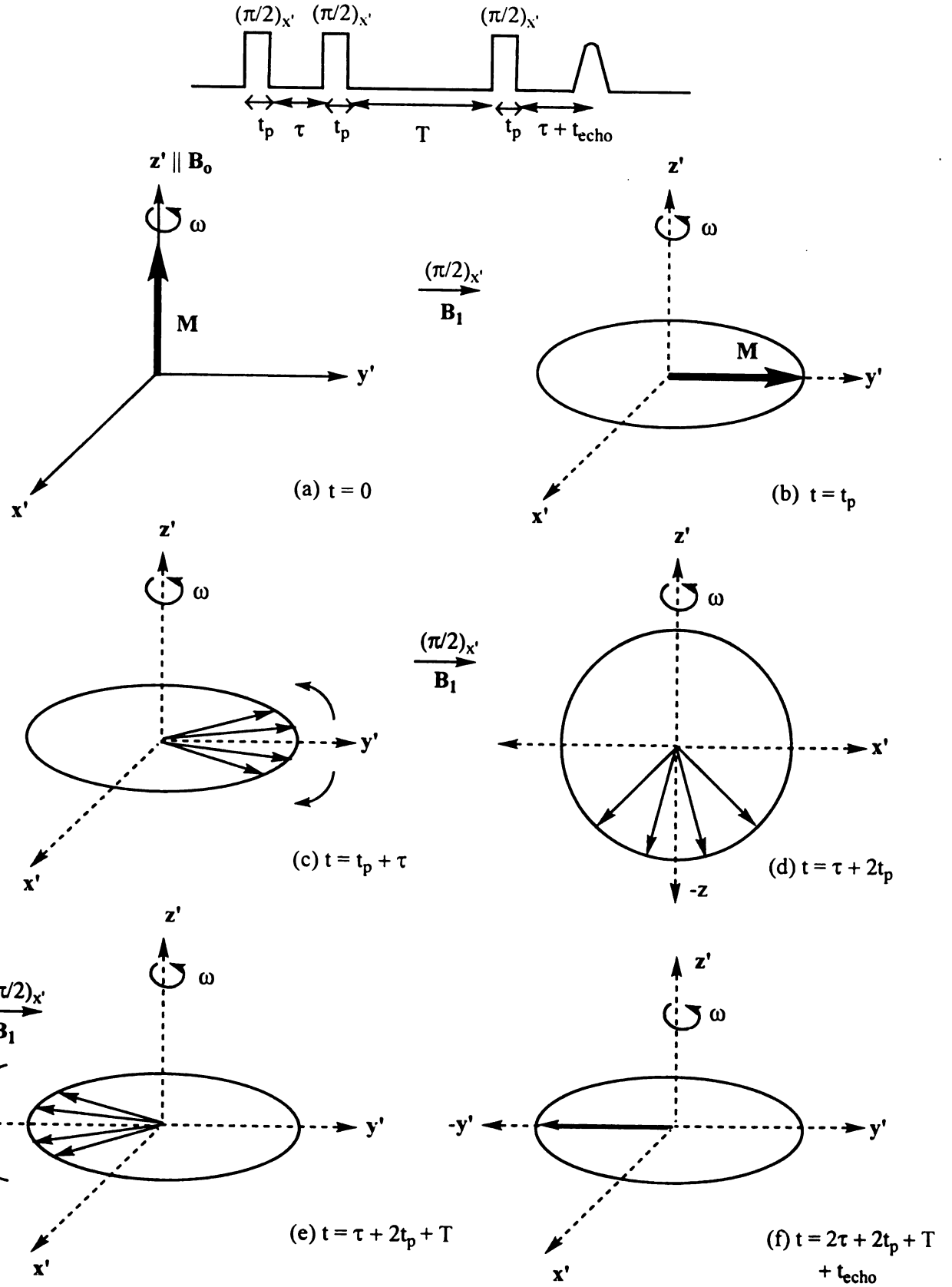
(π/2)x'
(π/2)x'
(π/2)x'
tp τ tp T tp τ + techo
z' || Bo
ω
M
y'
x'
(a) t = 0
(π/2)x'
B1
z'
ω
M
y'
x'
(b) t = tp
z'
ω
y'
x'
(c) t = tp + τ
(π/2)x'
B1
z'
ω
x'
-z
(d) t = τ + 2tp
(π/2)x'
B1
z'
ω
-y'
y'
x'
(e) t = τ + 2tp + T
z'
ω
-y'
y'
x'
(f) t = 2τ + 2tp + T
+ techo

II.2.2 Three-Pulse ESEEM spectroscopy

Some of the shortcomings of a two-pulse ESEEM experiment can be overcome by using a three-pulse experiment. The three-pulse experiment employs a $\pi/2 - \tau - \pi/2 - T - \pi/2$ pulse sequence (figure II-11). This sequence produces several echoes because it comprises three pairs of pulses that can produce two-pulse primary echoes in addition to the expected three-pulse echo, also called stimulated echo, which occurs at a time τ after the third pulse. The stimulated echo signal is recorded as a function of T, the time interval between second and third pulse, keeping τ fixed for a given measurement. Two-pulse echoes are eliminated by means of phase cycling of the mw pulses.

The effect of first mw pulse is same as in the two-pulse experiment discussed earlier. After the first $\pi/2$-pulse, the components that dephased in x'y' plane during first free precession period τ from the magnetization along +y' are rotated and stored along -z by another $\pi/2$-pulse, (figure II-11). If the waiting time T is such that, $T_2 < T < T_1$, then all the transverse magnetization would evolve as longitudinal magnetization that could be brought into the x'y' plane by another $\pi/2$-pulse and refocused to form a stimulated echo after time τ along -y' axis. If the waiting time is not long enough for the complete decay of transverse magnetization, it would lead to formation of an additional echo called Hahn echo at time τ after the second pulse. The amplitude of the stimulated echo depends of τ as well as T. During time τ the magnetization dephases in the x'y'-plane, so the echo modulation will decay via spin-spin relaxation as in two-pulse spin-echo sequence. The second $\pi/2$-pulse serves to store the precession frequency offsets $(\omega - \omega_0)$ of each spin packet as a longitudinal magnetization which forms the stimulated echo. As the magnitude of these longitudinal components are governed by a relatively slow spin-lattice

relaxation time, T_1, the overall decay rate of the amplitude of the stimulated echo is reduced leading to better frequency resolution as compared to the two pulse experiment.

An analytical expression for the three pulse modulation function for a S = 1/2, I = 1/2 system is,

$$E_{mod}(\tau) = |u|^4 + |v|^4 + |u|^2|v|^2 \{\cos(\omega_\alpha\tau) + \cos(\omega_\beta\tau) + 2\sin^2(\omega_\alpha\tau/2)\cos[\omega_\beta(\tau + T)] + 2\sin^2(\omega_\beta\tau/2)\cos[\omega_\beta(\tau + T)]\} \quad [2.63]$$

One important feature of the three-pulse echo is that it is modulated only at the nuclear frequencies ω_α and ω_β. The first pulse generates modulation effects at the nuclear frequencies; the second pulse creates additional modulations at the sum and difference of the nuclear frequencies. The third pulse causes interference between these sum and difference frequencies leaving only the nuclear frequencies in the modulation pattern. In presence of multiple nuclei the echo modulation function [2.62] is modified as,

$$E(\tau, T) = \frac{f_{decay}}{2}\left[\prod_{i=1}^{N} E_\alpha^i(\tau,T) + \prod_{j=1}^{N} E_\beta^i(\tau,T)\right] \quad [2.64]$$

The three-pulse echo decays as a function of T_1 which is much longer than T_2 at cryogenic temperatures, the decay time in a two-pulse experiment, hence leads to less line broadening in the frequency domain. Since fewer frequencies are involved and the modulation occurs over a longer time scale, so three-pulse spectrum is cleaner and better resolved as compared to a two-pulse spectrum.

In the pulsed experiments, mw pulses of very short widths (~20 ns) are required in order to ensure reasonable spectral width and to keep the effects of electron spin relaxation during the pulse negligible. For relaxation times in the range of μsec, in order to

achieve mw pulse-width short enough to be able to neglect relaxation, the requirement for microwave field is of the order of few mT (~30 G). It is technically difficult to obtain short and strong pulses. Another major difficulty encountered in a pulsed experiment is that of 'dead time'. It is the time needed for the high power transmitter pulses in the resonant cavity to decay far enough such that the echo signal can be observed. As a result the time domain data starts after the dead time (~ 0.15μsec) instead of starting at zero time (figure 7). Methods have been developed to overcome this problem by shortening the dead time[17-19], improving the detection scheme[20] and by developing better methods of data-analysis.[21]

List of References

1)Abragam, A.; Bleaney, B. *Electron Paramagnetic Resonance of Transition Ions*; Oxford University Press: Oxford, 1970.

2)Atherton, N. M. *Principles of Electron Spin Resonance*; Ellis Horwood Ltd.: West Sussex, England, 1993.

3)Gordy, W. *in Techniques of Chemistry, Vol. XV: Theory and Application of Electron Spin Resonance*; John Wiley & Sons: New York, 1980; Vol. XV.

4)Kevan, L.; Bowman, M. K. *Modern Pulsed and Continuous-Wave Electron Spin Resonance*; Wiley-Interscience: New York, 1990.

5)Mims, W. B. *Phys. Rev. B: Solid State* **1972**, *5*, 2409-2419.

6)Poole, C. P. *Electron Spin Resonance*; Wiley Interscience: New York, 1967.

7)Wertz, J. E.; Bolton, J. R. *Electron Spin Resonance*; Hall, C. a., Ed.; McGraw-Hill: New York, 1986.

8)Carrington, A.; McLachlan, A. D. *Introduction to Magnetic Resonance*; Chapman and Hall: London, 1979.

9)Keijzers, C. P.; Reijerse, E. J.; Schmidt, J. *Pulsed EPR: A new field of applications*: North Holland, Amsterdam, 1989.

10)McCracken, J. *Handbook of Electron Spin Resonance*; Poole, C. P. a. F., H.A., Ed.; Springer Verlag: New York, 1999; Vol. II, 63-89.

11)Rabi, I. I.; Ramsey, N. F.; Schwinger, J. *Revs. Modern Phys.* **1954**, *26*, 167-171.

12)Tolman, R. C. *The Principles of Statistical Mechanics*; Oxford University Press:, 1938.

13)Slichter, C. P. *Principles of Magnetic Resonance*; Springer-Verlag: Berlin, 1978.

14)Goldman, M. *Quantum Description of High Resolution NMR in Liquids*; Oxford University Press:, 1988.

15)Feynman, R. P. *Statistical Mechanics : A Set of Lecture Notes*; Benjamin, Reading: Masschusetts, 1972.

16)Fano, U. *Revs. Modern Phys.* **1957**, *29*, 74-93.

17)Narayana, P. A.; Massoth, R. J.; Kevan, L. *Rev. Sci. Instrum.* **1983**, *53*, 624-628.

18)Davis, J. L.; Mims, W. B. *Rev. Sci. Instrum.* **1981**, *52*, 131-132.

19)Cho, H.; Pfenninger, S.; Gemperle, C.; Schweiger, A.; Ernst, R. R. *Chem. Phys. Lett.* **1989**, *160*, 391-395.

20)Mims, W. B. *J. Mag. Res.* **1984**, *59*, 291-306.

Chapter III

INSTRUMENTATION

Early pulsed-EPR experiments, performed about forty years ago, showed that the FID from electron spins was strong enough to be observable.[1-3] The development of commercial spectrometers took some time because the technology required for the pulsed-EPR experiments is demanding. Due to the availability of faster digital logic components and advances in microwave component design, higher sensitivity and faster response times can be achieved in modern spectrometers, which nearly meet the idealized experimental conditions often assumed in theoretical analysis. The design and performance of the spectrometer is a strong function of the types of samples to be investigated. The most important criteria in the biological studies are to optimize the signal-to-noise ratio, to obtain highest sensitivity possible, and fast spectrometer response time.

Continuous wave-EPR spectra were obtained at X-band on a Bruker ESP300E commercial EPR spectrometer, using a TE_{102} EPR cavity, an Oxford ESR-900 continuous flow cryostat and an ITC 502 temperature controller. The microwave frequency was monitored by an EIP Microwave frequency counter Model 25B and the static magnetic field strength was measured using a Bruker ER 035M NMR gaussmeter.

The experimental pulsed-EPR data for this study were collected on a home-built pulsed EPR spectrometer built by Prof. J. L. McCracken at Michigan State University in 1990,[4] which has been modified from its original design since then. Some of the experiments that can be performed on this instrument include two-, three- and four-pulse

ESEEM, ESE-EPR (Electron Spin Echo detected EPR), ESEEM experiments with vector field jumps, Mims pulsed-ENDOR (Electron Nuclear Double Resonance), Davies pulsed-ENDOR, and HYSCORE (Hyperfine Sublevel Correlation Spectroscopy) in the frequency range of 6 to18 GHz.

The basic components of this spectrometer include a transmitter section capable of generating short, high-power microwave pulses as well as soft, low power pulses used to induce echo formation, a sample probe containing the sample, a receiver system for detecting the echo, a pulse programmer unit for controlling the timing and synchronization of the transmitter and receiver, and a magnet system. The schematic diagram is shown in figure III-1.

A microwave synthesizer (Gigatronics model 610) with a bandwidth of 6 to 18 GHz is used to generate cw-microwaves. It has an IEEE 488 interface and is controlled directly by the data collection program. The cw-microwaves are later converted into short microwave pulses by PIN diode switches that are directly controlled by a pulse logic module. The mw output of the synthesizer is about 10mW in power. It is divided by a directional coupler (Omni Spectra, model PN2025-601810) such that 90% of the mw power goes through a reference arm and 10% through the microwave pulse-forming arms. The reference arm has an adjustable phase shifter (ARRA, model 9828A) and serves both to bias the double balanced mixer (DBM) and as a phase reference for phase sensitive detection. In the pulse-forming arm the mw radiation goes through an isolator (Innowave, model 1119IR) to a power divider (Omni Spectra, model PN2089-6209-00), which divides it further into two independent pulse channels. The isolator prevents the reflected power from returning to the generator and helps in maintaining frequency

stability. These two mw pulse channels enable control of relative phases and the amplitudes of the mw pulses. Each pulse channel consists of a low-power, high speed PIN diode switch that creates pulses of desired widths (General Microwave model FM864-BH), a high-speed 0°/180° wide-band phase modulator (General Microwave model F 1938) that controls the relative phases of the pulses, and an isolator. The PIN diode switches and phase modulators are controlled by a home-built pulse logic circuit. One of these pulse channels has an attenuator (ARRA, model P9804-20) and the other has an adjustable phase shifter. The attenuator is needed to control the relative amplitude of the pulses in experiments like HYSCORE that require both soft and hard pulses. The attenuator introduces some phase shift, which is corrected by the adjustable phase shifter in the other arm. The pulses coming out of these channels are low power pulses of about 100 μW. They are combined by a pulse divider, passed through an isolator to eliminate any reflected pulses and are then fed into a medium-power GaAs FET amplifier (Avantek model SWL-89-0437). When GaAs FET amplifiers are used, some type of receiver protection, such as diode limiting, is usually used to prevent damaging the amplifier. *Since* the pulses of low power are fed to this amplifier, the limiter is not needed. The pulses coming out of the GaAs FET amplifier pass through an isolator to an attenuator and are then fed to a pulsed travelling wave tube amplifier (TWTA, Applied Systems Engineering, model 117). It is possible to achieve a gain of about 40 dBm with TWTA whereas mw power of about 60 dBm (1 kW) is needed for ESE experiments. So, an amplifier is used to ensure that the input power to TWTA be at least 20 dBm. To be in optimal working conditions the TWTA should be driven to saturation. The attenuator is

Figure III-1: Schematic of pulsed EPR spectrometer setup Various symbols used in this diagram represent the following components as :

Various symbols used in this diagram represent the following components as :

Directional Coupler


Isolator

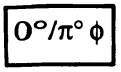

Phase modulator


Attenuator

Adjustible phase shifter


Power divider

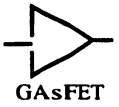

Galium-Arsenide field effect transistor preamplifier


Rotary vane variable attenuator


Double balanced mixer

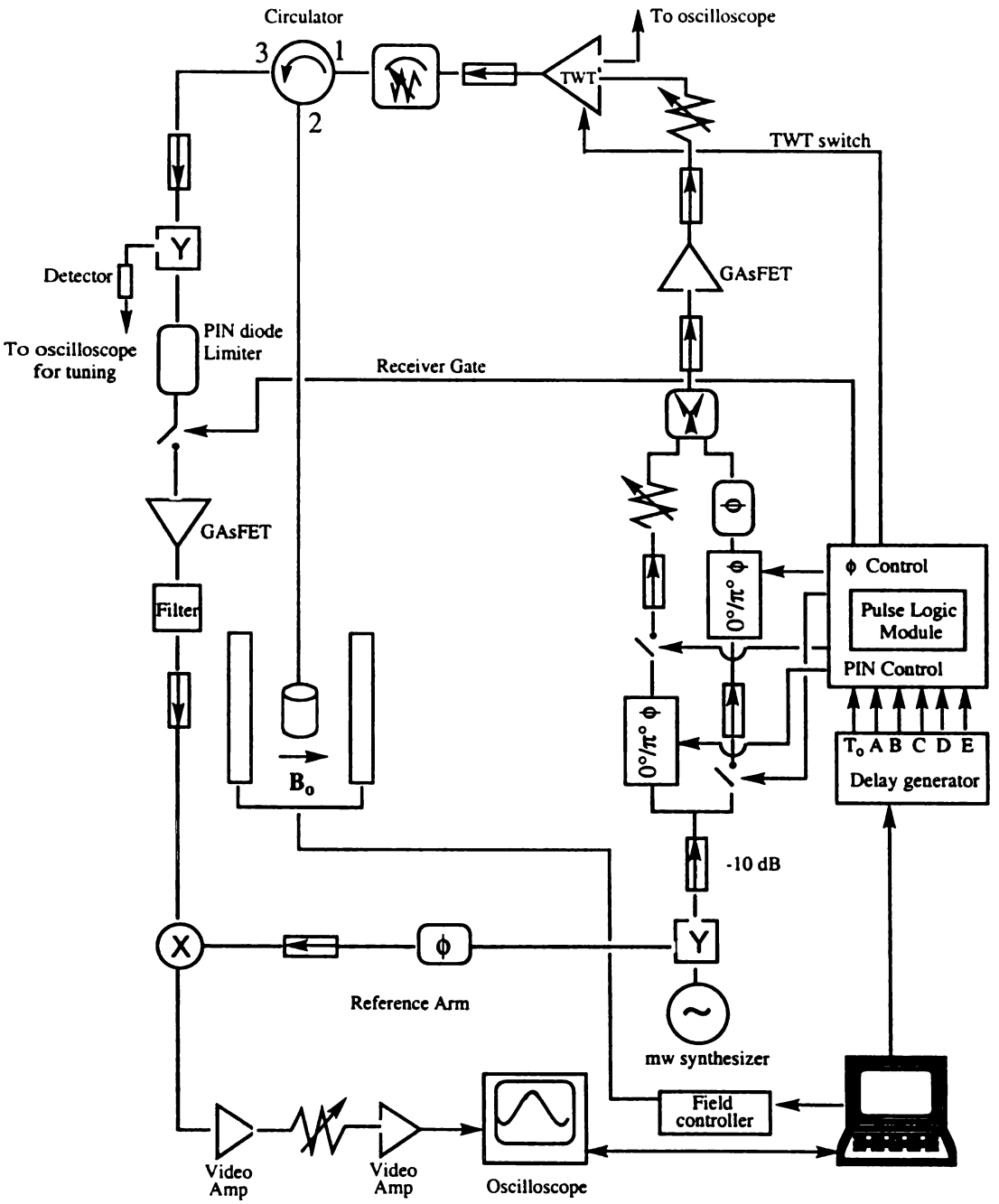
Circulator
3
1
2
To oscilloscope
TWT
TWT switch
GAsFET
Detector
To oscilloscope
for tuning
PIN diode
Limiter
Receiver Gate
GAsFET
Filter
B_0
ϕ Control
Pulse Logic
Module
PIN Control
0°/π°
T_0 A B C D E
Delay generator
-10 dB
Reference Arm
mw synthesizer
Field
controller
Video
Amp
Video
Amp
Oscilloscope

used to make sure that the TWTA is not over driven. The high power mw pulses from the TWTA pass through a rotary vane attenuator (Hewlett Packard, model X382A), which is used to vary the microwave power going to the sample, via an isolator, which protects TWTA from reflected power. In case of rotary vane attenuator, the attenuation is independent of frequency and does not introduce any phase shift in mw. The mw is then fed to a circulator (MACOM, model MA8K269) that controls the directional flow of microwaves into a reflection cavity with a folded stripline half-wave resonator[5,6] and a Gordon coupler.[6]

The microwave receiver utilizes wideband components and a balanced mixer (RHG model DM2-18 Ab) in a conventional homodyne arrangement. Signal from the resonator goes to a directional coupler via a waveguide isolator. It is then fed to a low noise GaAs amplifier (Avantek model AWT-18635). In order to protect this amplifier from the high-power excitation pulses, a medium-power, high speed PIN diode limiter (Innowave, model VPL-6018) and a fast PIN diode switch (General Microwave model F9114) controlled by the pulse-logic circuit, are used. The PIN diode switch remains open most of the time and is closed by the pulse-logic circuit only at the time of appearance of echo. About 1% of the signal from the directional coupler is fed via a detector to an oscilloscope (Tektronix 620 B digital oscilloscope) for spectrometer tuning. Electronic components cannot pass microwave frequencies so, the detector is employed to convert microwave energy to a video frequency. The signal from the amplifier goes through a bandpass filter (K & L Microwave, model 3H10-2000/18000-0/0), which serves to remove radio frequency noise introduced by the PIN diode switches, and an isolator and then is fed to a double balanced mixer (DBM) (RHG, model DM2-18 AB) in order to

convert to an electrical signal. The mixing scheme employed is a conventional homodyne arrangement. At the mixer, the signals from the reference arm and the receiver are combined to generate signals at the sum and the difference of the two input frequencies. The amplitude of the echo signal is proportional to the difference in amplitudes of the two input signals and their relative phases. This scheme of mixing the echo signal with a reference signal at same frequency is known as homodyne detection. The homodyne detection scheme not only allows for a coherent detection and phase discrimination of the echo but also provides a method of increasing signal-to-noise ratio. At the output of DBM the echo signal consists of frequency components centered about 50 MHz. The amplitude of the difference frequency is next amplified using a video amplifier (Comlinear, model E220), sampled by feeding to a digital oscilloscope (Tektronix 620 B) for analog to digital conversion for input to a computer.

The magnetic field is produced by an electromagnet (Walker Scientific, model HF-12H) and controlled over a range from 50 G to 15000 G by a Hall-effect field controller (Bruker, model B-H15), interfaced to the computer via IEEE-488 interface device. Experiments were carried out at 4.2 K, using a home built liquid helium immersion dewar capable of maintaining constant temperature of 4.2 K for about 15 hours. For most of the microwave network semirigid and flexible coaxial cable was used to reduce the geometric constraints of waveguides, but the high-power pulses and emitted echo from the probe were directed by waveguides to avoid the higher losses inherent in coaxial cables. The device connections were made with SMA-microwave connectors.

The spectrometer is controlled by a PowerComputing Macintosh computer via an IEEE-488 interface (National Instruments). Digital delay and gate generators (Stanford

research, Model DG535) are used to generate the accurate timing signals which are transferred to the pulse logic module and serve as a timing base for synchronization of the echo experiment. It controls the timings required to turn on the high-power TWTA, to control microwave pulse generation and spacing, to generate accurate pulse delays required for the experiments, to control the overall repetition rate of the measurements, to modulate the phase on the alternate echo generating cycles and to supply trigger pulses to the oscilloscope responsible for measuring spin echo intensities. For best performance it is essential that all timing pulses and intervals be synchronized to avoid jitter and instabilities and to insure that all timing intervals be properly aligned. The pulses to the PIN diode which form 90° and 180° pulses must be positioned such that the trailing edge of the pulses is aligned with the trailing edge of the TWTA modulator pulse. This is necessary since the high noise output of the TWTA would otherwise completely mask the echo. The pulse timing is directly programmed through the computer, which then performs the entire echo experiment using the pulse programmer and data collection software.

The data collection program is written in LabVIEW 5.0.1 (National Instruments) running on a Power Computing model 200 computer. The simulation programs are written in FORTRAN language. The software for the analysis of the experimental and simulated data is written in Matlab (Mathworks, Nantick, MA). Numerical simulations of the experimental data are performed on Sun SparcII work station.

III.1.1 Resonator

A resonant cavity is the microwave analog of a series RLC tuned circuit (figure III-2). The stored electric and magnetic energies inside the resonator determine its equivalent inductance and capacitance. The energy dissipated by the finite conductivity of the resonator's walls determines its equivalent resistance. It is a metallic enclosure with

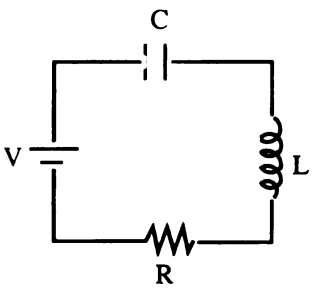

Figure III-2: A series RLC circuit fed by voltage V.

dimensions comparable to the wavelength made from high conductivity metal. At resonance, the cavity can sustain mw oscillations, which form standing waves from superimposed microwaves reflected from cavity walls.

A given resonator has an infinite number of resonant modes, and each mode corresponds to a definite resonant frequency. When the frequency of an input signal is equal to a resonant frequency, a maximum amplitude of standing waves occurs, and the peak energies stored in the electric and the magnetic fields are equal. The mode that has the lowest resonant frequency is called the dominant mode. At resonant frequency f_o, $\omega_o = 2\pi f_o = 1/(LC)^{1/2}$. When the power is turned off, the energy of the RLC circuit dissipates exponentially with time, approximately as a function of $\exp(-\omega_o t/Q)$, where Q

is called quality factor of the circuit, larger the Q slower the power dissipates. It is defined as,

$$Q = 2\pi \text{ (maximum energy stored/ Energy dissipated per cycle)} = \omega_o L/R$$

In a cw-EPR spectrometer the sensitivity is optimized by choosing a microwave cavity probe with large Q. The rectangular TE_{102} mode cavity that was used in cw-EPR experiments, has Q factor of 5,000. Such large Q factors are unacceptable for pulsed work because the excessively long ring down time would mask the echo. This situation is usually compounded by the finite time required by the transmitter TWTA pulse output to decay to near thermal noise levels. For samples with short phase memory times and small sample volumes, it is desirable to observe the echo immediately following the last transmitter pulse. Low Q factors are therefore required to limit the ring down time. Samples with short phase memory time also require short pulses for echo formation. Although the pulse areas should approach delta functions, an acceptable pulse width is generally on the order of 10% of the phase memory time. Most pulsed spectrometer use probes with Q values ranging between 50 and 500. Such low Q values can be obtained by using the inherently high Q cavity geometries and over coupling, by loading the cavity with a high dielectric material, or by loading with metallic blocks. Unfortunately, the same procedures used for lowering cavity Q also reduce the sensitivity. A better method to achieve a lower Q while maintaining the sensitivity is to use special microwave structures which have inherently lower Q than cavities and have large filling factors, the ratio of the sample volume to the volume in which the microwave field is contained. The folded stripline half-wave resonator that was used in the ESEEM experiments has a Q factor of about 800. The loaded Q of the resonator was varied by adjusting the position

of a teflon Gordon coupler that determined the coupling between the waveguide and the resonator. In pulsed experiment it was overcoupled to lower the Q to ~80.

Stripline resonator

The design of folded stripline half-wave resonator is shown in figure III-3 (a). The resonator is a rectangular strip of brass $\lambda/2$ in length and 5 mm in height bent in the form of an arc and fits firmly in a hole 5.5 mm in diameter in the teflon block. When immersed in liquid helium, teflon shrinks more than brass and the resonator is held tightly in place. The teflon block with the resonator is mounted and is held by a nylon screw inside part of X-band waveguide with interior dimensions of 1.02 by 2.29 cm, which is effectively a TE_{102} cavity oriented with its long axis vertically.

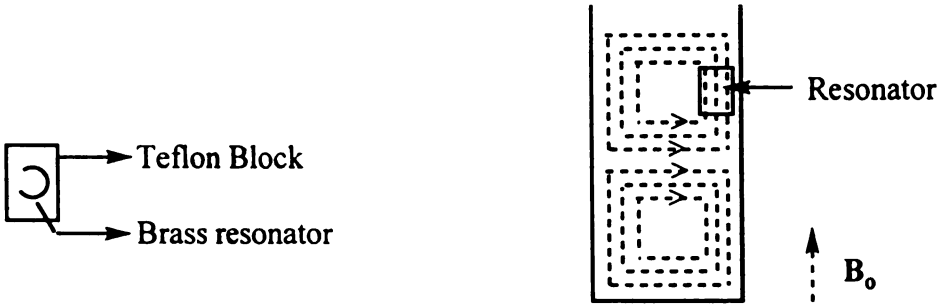

Figure III-3: Schematic of folded stripline half-wave resonator mounted in teflon block as seen from top (a), transverse cross section of the cavity showing the mw magnetic field lines that couple to the resonator (b).

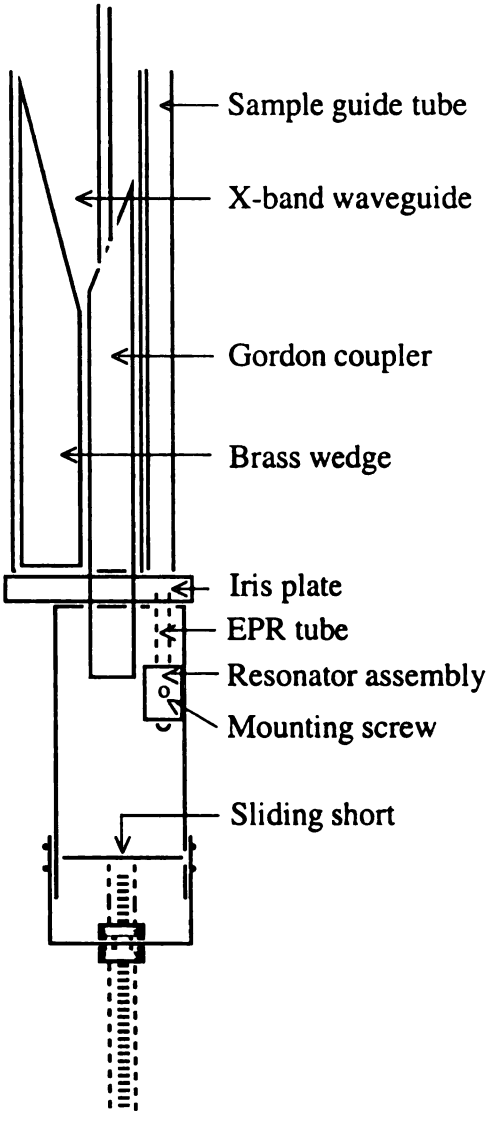

Figure III-4: Schematic of the folded stripline half-wave resonator probe structure.

This cavity is then screwed to the rest of the waveguide with an iris plate in between. The resonator couples to the standing wave magnetic field lines running vertical along the walls of the cavity (figure III-3 b). The bottom of the cavity is made of a screw-operated sliding short that is initially positioned to provide maximum coupling of the resonator. Its position is left unchanged once optimal position is found and all the coupling adjustments are done through a coupler. An external stainless steel guide tube is mounted along the axis of the resonator and runs parallel to the waveguide. Sample is contained in quartz EPR tube, the upper end of which is slipped into a teflon holder. This teflon holder is attached to a stainless steel rod and is inserted through the guide tube (figure III-4).

III.1.2 Gordon coupler

Mw power is coupled into the cavity via a Gordon coupler. A long teflon insert that tapers as a wedge as shown in figure III-4. The position of this insert can be varied with the help of a teflon rod whose one end is inserted into the teflon insert and it runs through the waveguide and has its other end available outside the waveguide for adjusting its position. By varying the position of this coupler the loaded Q of the resonator can be changed.

III.1.3 Circulator and Isolator

Both mw circulator and mw isolator are nonreciprocal transmission devices that use the property of Faraday rotation in the ferrite material. A nonreciprocal phase shifter consists of a thin slab of ferrite placed in a rectangular waveguide at a point where the dc

magnetic field of the incident wave is circularly polarized. Ferrite is a nonlinear material and in presence of a dc magnetic field it exhibits a phenomenon of Faraday rotation and rotates the plane of polarization of the incident mw. By choosing a suitable length of the ferrite slab a desired phase shift can be obtained between two directions of propagation such that the reflected wave can not propagate backwards. At port 1 the polarization of the mw is altered such that it is directed to the resonator element in the cavity at port 2 (figure III-5). The plane of polarization of the mw reflected from the cavity at port 2 is such that it is can not propagate to port 1, and is directed to the detector at port 3 instead. Any reflected mw from the detector is directed to port 4 and is terminated to ground by a 50 Ω terminator on reaching port 4.

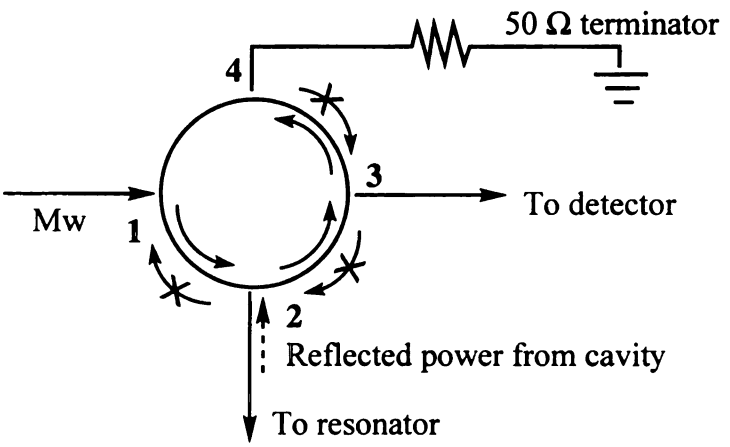

Figure III-5: Symbolic representation of a four port circulator.

An isolator works on the same principles as a circulator. It is in principle a three port circulator that terminates any reflected power. It is a necessary component in order to protect devices from reflective mw power.

List of References

1)Gordon, J. P.; Bowers, K. D. *Phys. Rev. Lett.* **1958**, *1*, 368.

2)Kaplan, D. E.; Browne, M. E.; Cowen, J. A. *Rev. Sci. Instrum.* **1961**, *32*, 1182.

3)Wanlass, L. K.; Wakabayashi *Phys. Rev. Lett.* **1961**, *6*, 271.

4)McCracken, J.; Shin, D.-H.; Dye, J. L. *Appl.Magn. Reson.* **1992**, *3*, 305-316.

5)Bowman, M. K.; Lin, C. P.; Norris, J. R. *J. Magn. Reson* **1985**, *65*, 369-374.

6)Britt, R. D.; Klein, M. P. *J. Mag. Res.* **1987**, *74*, 535-540.

CHAPTER IV

CHARACTERIZATION OF THE TTQ-SEMIQUINONE CATALYTIC INTERMEDIATE OF MADH BY ESEEM

IV.1 Introduction

This chapter presents results from continuous-wave electron paramagnetic resonance (cw-EPR) and electron spin echo envelope modulation (ESEEM) spectroscopic studies on the semiquinone forms of the cofactor of MADH. The cw-EPR spectrum of TTQ semiquinone prepared by substrate addition (N-form) was found to differ substantially from that observed when the semiquinone was generated by reduction of the enzyme with dithionite (O-form). These differences prompted a detailed study of hyperfine and nuclear quadrupole interactions of three ^{14}N atoms of the semiquinone species using ESEEM. Two of these heteroatoms are derived from the indole and the indole-quinone side chains that comprise TTQ, while the third ^{14}N originates from substrate methylamine. Three-pulse ESEEM spectra of $CH_3{}^{14}NH_2$-reduced sample showed three isolated features at 1.0, 1.5 and 4.3 MHz, which were absent in MADH sample reduced with $CH_3{}^{15}NH_2$. Analysis of spectral data from substrate-derived ^{14}N revealed an isotropic hyperfine coupling of 2.4 MHz and nuclear quadrupole couplings characterized by $e^2qQ = 1.7$ MHz and $\eta = 0.5$. The hyperfine and the nuclear quadrupole couplings found for the two ^{14}N nuclei indigenous to TTQ were: A_{iso}, 2.8 and 1.9 MHz; e^2qQ, 3.0 and 2.1 MHz and η, 0.3 and 0.7, respectively. Taken together, these couplings provide definitive evidence that substrate ^{14}N is covalently bound to TTQ when the cofactor is in its one-electron reduced form and that it has an imine-like structure. The

intensities of the modulations indicate that the semiquinone generated by the method recently reported by Zhu and Davidson[1] results in a homogeneous preparation of the radical. A comparison of ^{14}N hyperfine and nuclear quadrupole couplings measured for the N-form semiquinone with those measured previously for the O-form[2] shows that a significant change occurs in the highest occupied molecular orbital when substrate nitrogen is bound, and may be related to the different redox and electron transfer properties of these two semiquinone forms.

IV.2 Materials and Methods

IV.2.1 Protein purification and preparation

The MADH under study was obtained from *Paracoccus denitrificans* and was purified as described previously.[3] The concentration of MADH was calculated from known extinction coefficients in 10mM phosphate buffer, pH 7.5.[3-5] The extinction coefficients of the different redox forms of MADH vary with pH and ionic composition of the buffer.[6] MADH was fully reduced with substrate methylamine (1 MADH : 2 methylamine). Then the fully reduced MADH, which exhibits an absorption maximum at 330 nm, was photo-oxidized by exposing it to a source of long-range UV light until the absorption at 420 nm (due to the semiquinone form) reached a maximum.[1] This typically occurred in 5-10 min. The source for long-range UV light was a Rad-Free RF UV-365 Long-Wave UV Lamp (Schleicher & Schleicher) using an 8W bulb that emitted light spanning wavelengths from 320-380nm with a peak value at 365 nm. The UV light source was placed approximately 3 inches away from the sample contained in a quartz

cuvette. The effects of light are completely reversible.[1]

IV.2.2 Continuous-wave EPR spectroscopy

Continuous wave-EPR spectra were obtained at X-band on a Bruker ESP300E EPR spectrometer, using a TE_{102} EPR cavity, an Oxford ESR-900 continuous flow cryostat and an ITC 502 temperature controller. The microwave frequency was monitored by an EIP Microwave frequency counter Model 25B and the static magnetic field strength was measured using a Bruker ER 035M NMR gaussmeter.

IV.2.3 ESEEM spectroscopy

The ESEEM spectra were recorded at X-band with a home-built spectrometer[7] described in chapter III. Our spectrometer was modified from its original design in that signal averaging and subsequent integration of the electron spin echo signals was accomplished by a Tektronix 620 B digital oscilloscope fed directly by the double-balanced mixer and mixer preamplifier of the microwave bridge. In the original design a boxed-car integrator was used for this purpose. The pulse sequence for the three-pulse ESEEM experiment, $\pi/2$-τ-$\pi/2$-T-$\pi/2$-τ-echo, used a two-step (0, 0, 0), (π, π, 0) microwave pulse phase cycling to eliminate two-pulse echo interference. The modulation was observed by recording integrated spin-echo intensities as a function of T. ESEEM spectra were recorded at τ-values that ranged from 150 to 600 ns. Typical conditions for data collection were: microwave frequency, 8.815 GHz; pulse power, 43 W; pulse width, 20 ns; sequence repetition rate, 6 Hz; total number of experimental points, 512; time increment, 20 ns; number of events averaged/point, 10; sample temperature, 4.2 K and

each data set represented an average of 9 scans.

ESEEM spectra were obtained by a Fourier analysis procedure that included dead time reconstruction.[8] Numerical simulations of the experimental data were performed on Sun SparcII work station. Simulation programs were written in FORTRAN and were based on the density matrix formalism developed by Mims.[9] Software for the frequency analysis of the experimental and simulated data was written in Matlab (Mathworks, Nantick, MA). The data collection programs for our pulsed EPR spectrometer were written in LabVIEW 5.0.1 (National Instruments) running on a Power Computing model 200 Power PC.

IV.3 Results

IV.3.1 CW-EPR Spectroscopy

Figure IV-1 shows cw-EPR spectra of TTQ semiquinone prepared by reduction of MADH with dithionite (a), $CH_3{}^{14}NH_2$ (b), and $CH_3{}^{15}NH_2$ (c) in frozen buffer. All three spectra consist of simple derivative line shapes that have no observable hyperfine structure. The dithionite-reduced (O-form) and the substrate-reduced (N-form) semiquinone spectra are centered at g = 2.0043 and g = 2.0039, respectively. The peak-to-peak linewidths of the O-form, ^{14}N- and ^{15}N-substrate generated semiquinones were observed to be 6.81 G, 11.09 G and 11.55 G respectively. The lineshapes for all three of these TTQ semiquinones are more symmetrical than those found for samples poised by comproportionation.[10] Apparently, the asymmetry observed previously for the comproportionation products arose from the mixture of 'O-' and 'N-' form spectra present.[2]

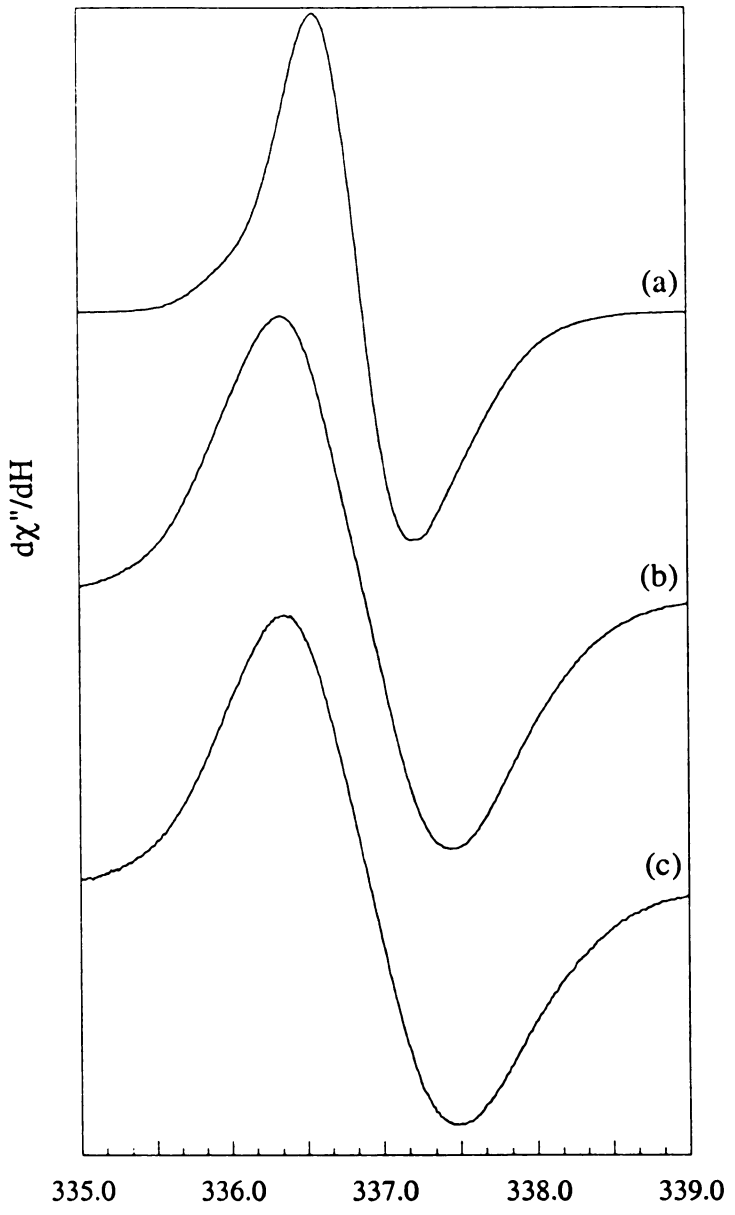

Figure IV-1: Continuous-wave EPR spectra of the semiquinone forms of methylamine dehydrogenase from *P. denitrificans* generated by dithionite addition (O-form) (a), ^{14}N-methylamine addition followed by illumination (b), and ^{15}N-methylamine addition followed by illumination (c). Spectra were collected under the following conditions: microwave power, 0.63mW; microwave frequency, 9.473GHz; modulation frequency, 100 kHz; modulation amplitude, 0.1 mT; sample temperature, 103 K; and number of scans averaged, 10.

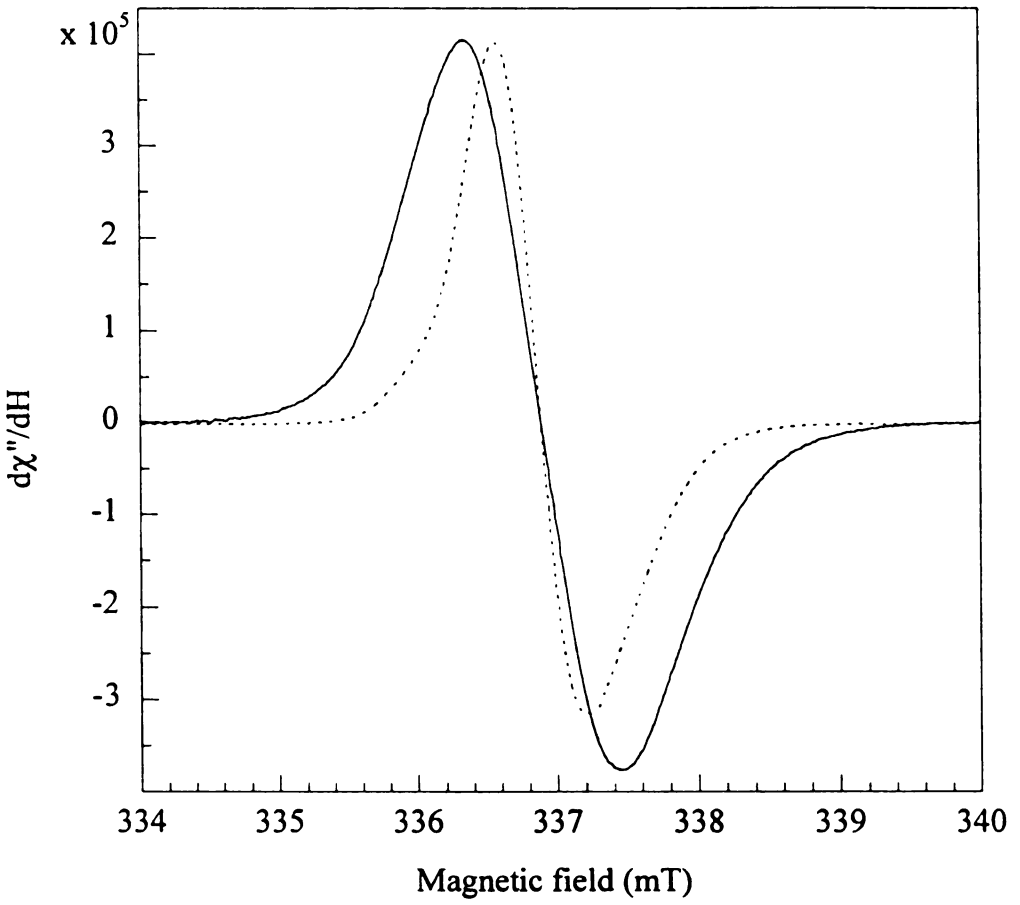

Figure IV-2: Continuous-wave EPR spectra of the semiquinone forms of methylamine dehydrogenase from *P. denitrificans* generated by dithionite addition (O-form) (dashed line), ^{14}N-methylamine addition followed by illumination (solid line). Conditions were same as in figure IV-1. Presence of both the N-form and the O-form in the samples prepared by comproportionation method lead to the asymmetric spectrum.

IV.3.2 ESEEM Spectroscopy

To understand the differences in electronic structure of substrate- and dithionite-poised semiquinone, ESEEM spectroscopy was used to probe the hyperfine couplings of ^{14}N nuclei derived from substrate and from those native to the cofactor. The presence of the nitrogen derived from the substrate, was revealed by comparing identical samples of enzyme prepared by initial substrate reduction with ^{14}N-methylamine and by ^{15}N-methylamine. Distinct differences are expected in the magnetic interactions between the unpaired electron spin density and the nuclear spin I = 1 ^{14}N nucleus relative to those with I = 1/2 ^{15}N nucleus. Typically, three-pulse ESEEM data were characterized by deep low frequency modulations that damped over a 10 μsec range of T (figure IV-3). A cosine Fourier transformation of the time domain ESEEM data collected at τ = 219 ns, for N-form semiquinone poised with ^{14}N-methylamine yielded the spectrum of figure IV-4(a). This spectrum shows sharp features in the low frequency region, at 0.5, 1.0, 1.5, 2.0 and 2.5 MHz and a broad feature with a complex lineshape from 4.6-5.8 MHz. To distinguish peaks that arise from substrate ^{14}N-coupling, data was collected under identical spectrometer conditions for ^{15}N-methylamine poised semiquinone and is shown in figure IV-4(b). This spectrum also features deep modulations with peaks at 0.5, 2.0 and 2.5 MHz characterized by narrow lineshapes, along with a broad feature at 4.5-5.8 MHz. The spectra in figure IV-4 are indicative of nitrogen nuclei coupled to a paramagnetic center near the "exact cancellation condition".[11,12] Because ^{15}N is a spin I = 1/2 nucleus, its

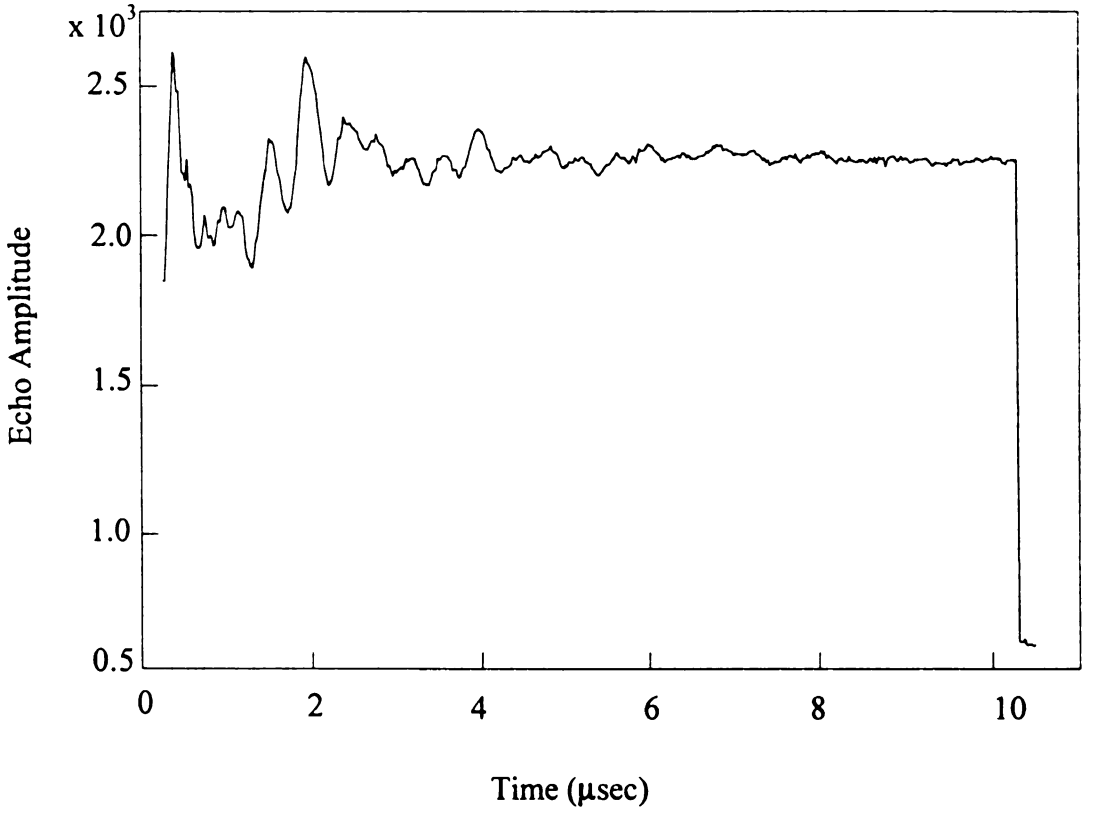

Figure IV-3: Time-domain three-pulse ESEEM spectra of randomly oriented ^{14}N-methylamine-reduced semiquinone, Conditions: τ, 219 ns; Microwave frequency, 8.815 GHz; magnetic field, 315.5 mT; microwave pulse power, 43W; pulse sequence repetition rate, 4 Hz; events averaged per time point, 10; sample temperature, 4.2 K; number of scans averaged, 9.

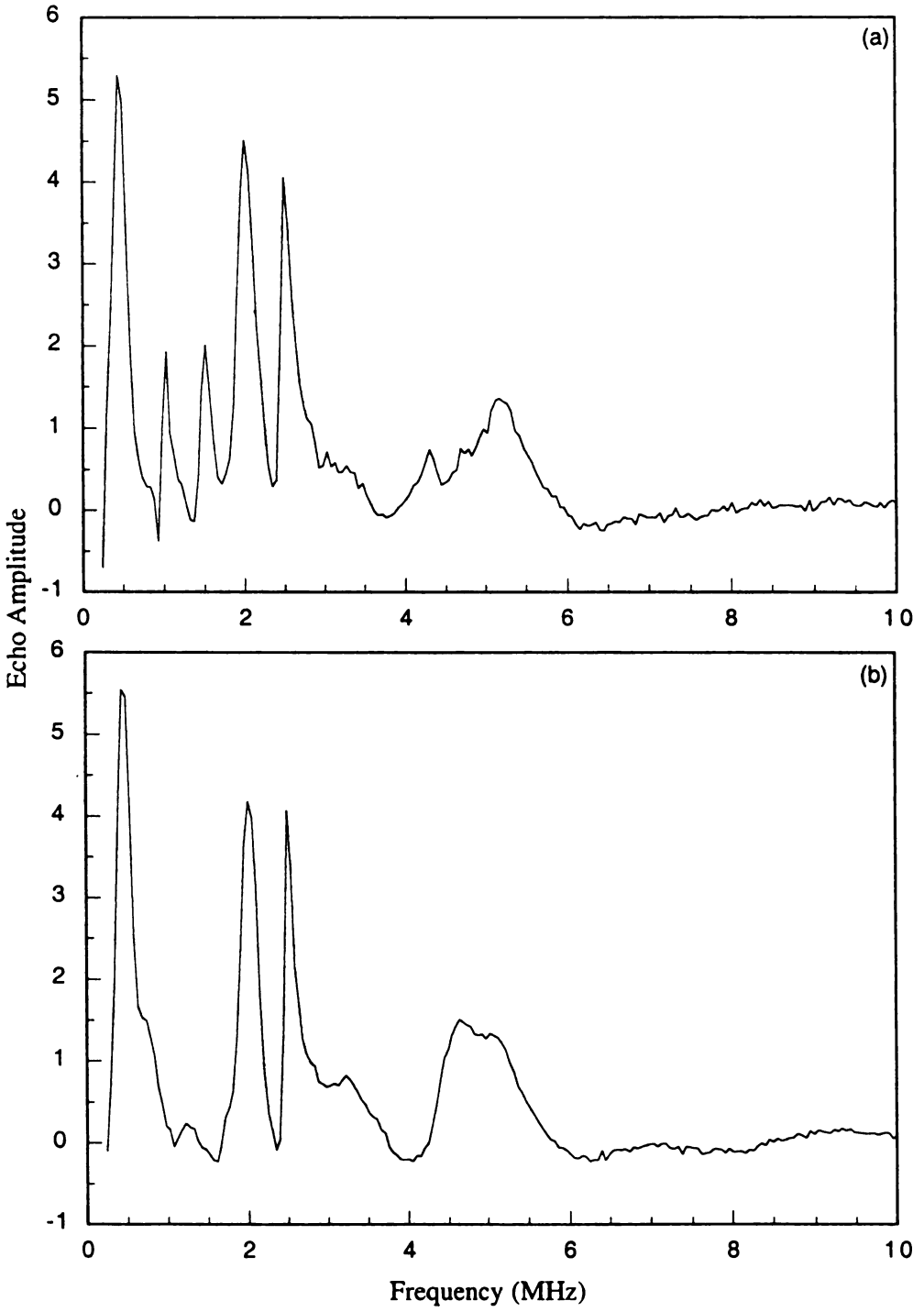

Figure IV-4: Frequency-domain three-pulse ESEEM spectra of randomly oriented (a) ^{14}N-methylamine-reduced semiquinone; (b) ^{15}N-methylamine-reduced semiquinone. Conditions were identical to those given in figure IV-3.

ESEEM contribution is expected to be distinctly different from that of ^{14}N. A comparison of the two data sets shown in figure IV-4 identifies the narrow peaks at 1.0 and 1.5 MHz as arising from hyperfine coupling to the $CH_3{}^{14}NH_2$-derived nitrogen.

Figures IV-5 and figure IV-6 show three-pulse ESEEM data collected for $CH_3{}^{14}NH_2$- and $CH_3{}^{15}NH_2$-treated MADH at two other τ-values, 365 ns (figure IV-5) and 450 ns (figure IV-6). Because of the τ dependence of three-pulse ESEEM amplitudes (equation [2.63]), different frequencies are accentuated in these two data sets. For the τ = 365 ns data (figure IV-5a, b), there is a significant difference in the amplitude of the 0.5 MHz component, with it being twice as intense with respect to 2.0 and 2.5 MHz peaks (assigned to TTQ) for the $CH_3{}^{14}NH_2$ sample (figure IV-5a) as for the $CH_3{}^{15}NH_2$ counterpart (figure IV-5b). This observation allows us to assign part of the intensity at 0.5 MHz to substrate-derived ^{14}N. Similarly, peaks at 0.8 and 1.2 MHz are observed for both ^{14}N- and ^{15}N- methylamine treated samples at τ = 450 ns (figs. IV-6a, b) and are assigned to the second ^{14}N of the TTQ cofactor (N(2)). ESEEM data collected at τ = 365 and 450 ns show a strong peak at 4.3 MHz due to substrate-derived ^{14}N. The narrow linewidth of this modulation component relative to the broad 4.6-5.8 MHz feature observed for N(1) of the $TTQ^{\bullet}$ (figure IV-4) indicates that the anisotropy in hyperfine interaction for substrate-derived ^{14}N might be comparatively small. Assignments based on these observations and the assumption that both TTQ nitrogens (labeled N-1 and N-2) are near "exact cancellation"(section IV.4.2) such that their low frequency lines are additive, are listed in table IV-1.

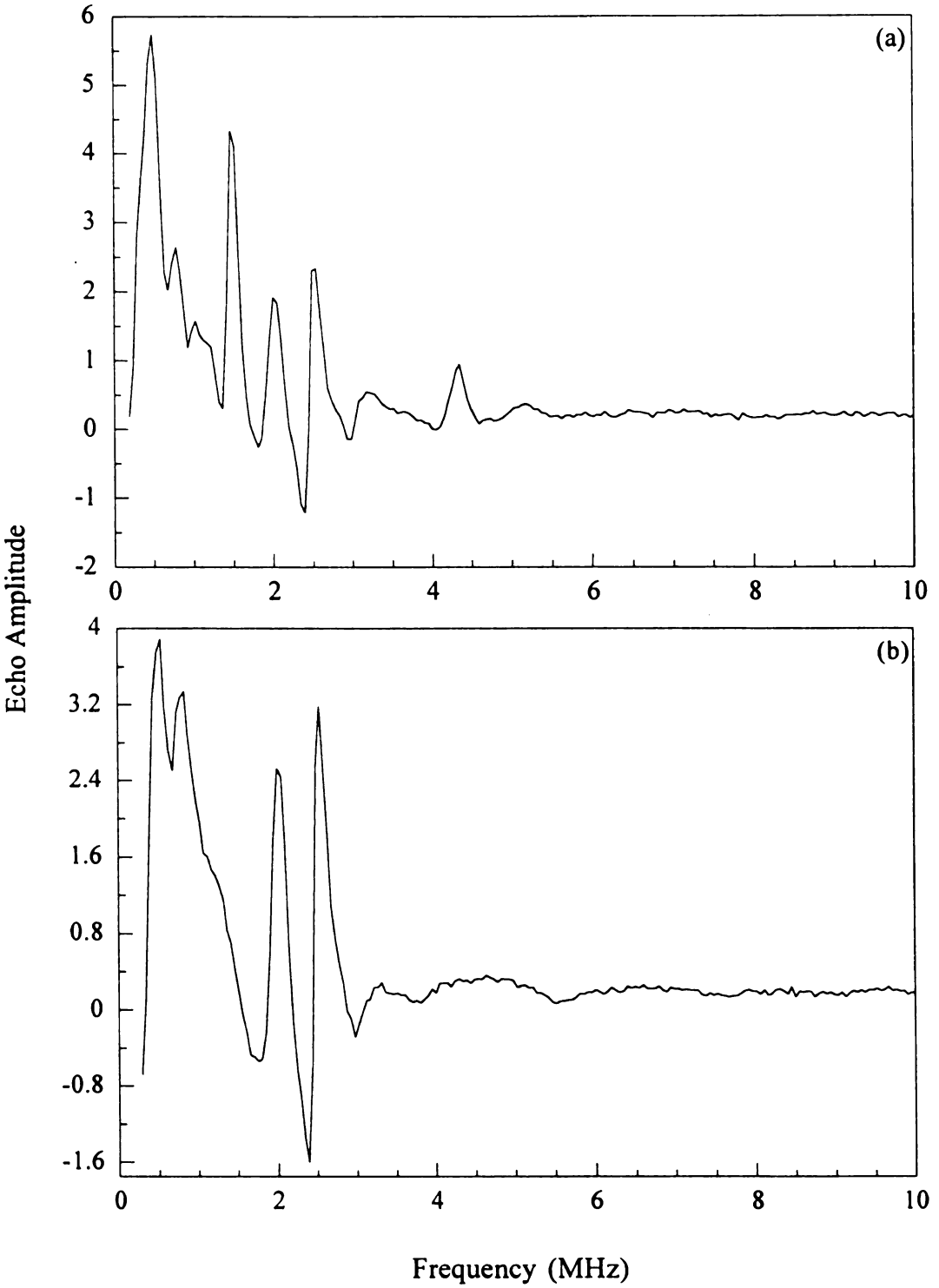

Figure IV-5: Three-pulse ESEEM spectra of randomly oriented ^{14}N-methylamine-reduced semiquinone (a); and ^{15}N-methylamine-reduced semiquinone (b). τ = 365 ns. Other conditions were identical to those given in figure IV-3.

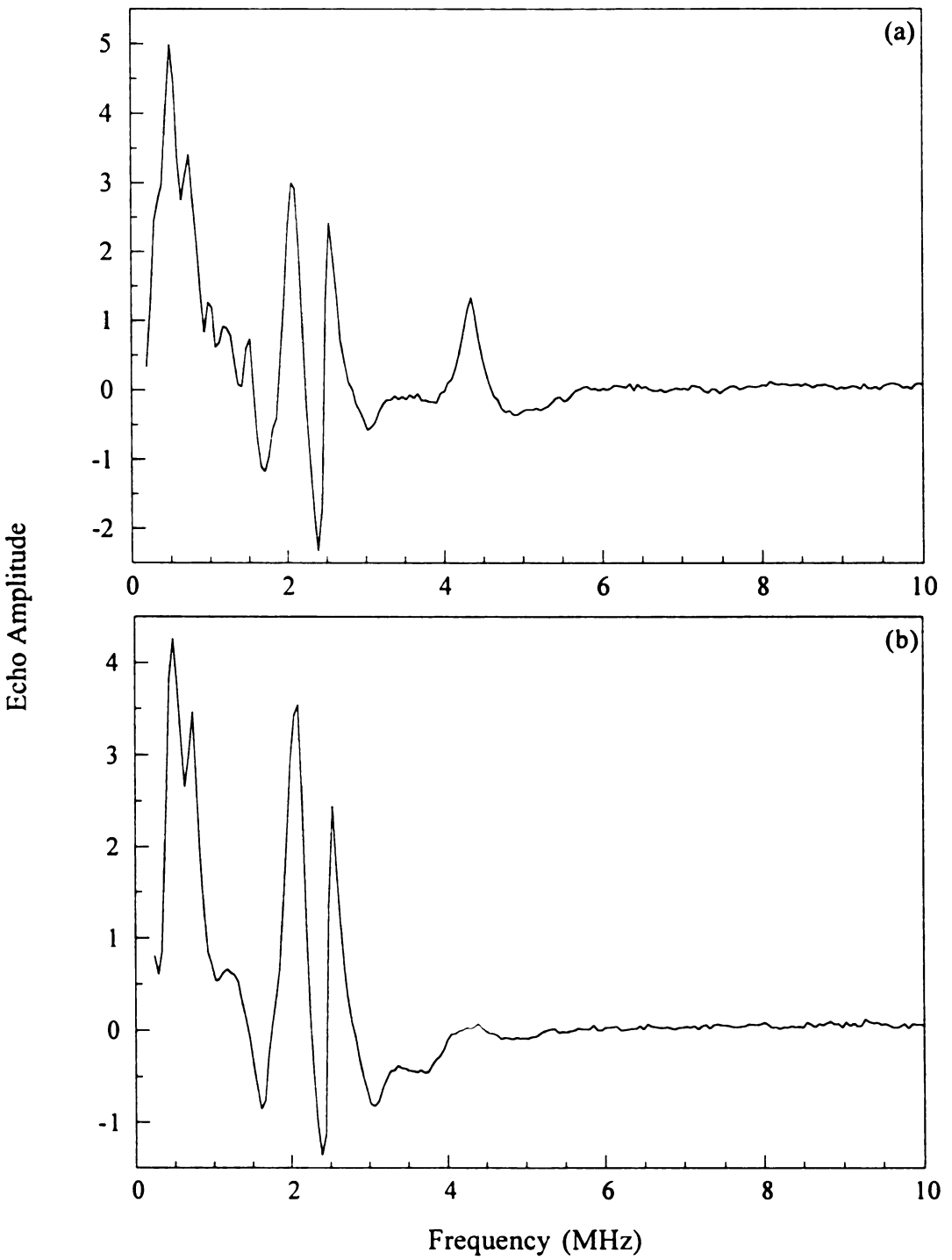

Figure IV-6: Three-pulse ESEEM spectra of randomly oriented ^{14}N-methylamine-reduced semiquinone (a); and ^{15}N-methylamine-reduced semiquinone (b). τ = 450 ns. Other conditions were identical to those given in figure IV-3.

IV.4 Discussion

Continuous wave EPR spectra of frozen solutions of MADH semiquinones prepared by reduction with ^{14}N- or ^{15}N-methylamine show lineshapes that are inhomogeneously broadened due to the presence of multiple hyperfine interactions. The observed increase in peak-to-peak linewidth of cw-EPR spectra for substrate-reduced as compared to dithionite-reduced semiquinone is indicative of a different electronic structure for the two forms. To understand these differences in detail, hyperfine and quadrupole coupling constants for the nitrogens that give rise to the ESEEM of figures IV-4, IV-5 and IV-6 must be determined.

IV.4.1 Interactions of the nitrogen nucleus

The ^{14}N nucleus has a spin I = 1 and possesses nuclear quadrupole moment that is rather small, about $+0.016 \times 10^{-24}$cm^2. As a result, ^{14}N e^2qQ values are small, seldom more than 6 MHz. However, the nuclear quadrupole interaction (nqi) tensor is usually large relative to the nuclear Zeeman interaction (~ 1MHz at X-band) and has marked effect on its modulation frequencies.

The nuclear quadrupole coupling energy is given by,

$$E_Q = - e/6\ \mathbf{Q}_{ij}\ \mathbf{V}_{ij} \qquad [4.1]$$

where e is the electronic charge, **V** and **Q** are symmetric 3 × 3 tensors that describe the time averaged electric field gradient and the nuclear quadrupole moment respectively. The product of these two tensors will depend on the relative orientation of the two axis systems. When the axis system of **Q** is chosen to coincide with that of the spin system,

then due to cylindrical symmetry of the nucleus, tensor **Q** can be defined in terms of a single parameter 'nuclear quadrupole moment' Q. The electric field gradient tensor **V** is symmetric and can also be expressed in its own principal axis system (PAS) to yield a diagonal traceless tensor, with $\partial^2V/\partial x^2$, $\partial^2V/\partial y^2$ and $\partial^2V/\partial z^2$ as the diagonal elements, where V is the electrostatic potential at the nucleus. The electric field gradient tensor can be expressed in terms of two quantities,

$$q_{zz} = \partial^2V/\partial z^2 \text{ and } \eta = \frac{(\partial^2V/\partial x^2) - (\partial^2V/\partial y^2)}{\partial^2V/\partial z^2} = (q_{xx} - q_{yy})/\, q_{zz} \qquad [4.2]$$

By convention $|q_{zz}| > |q_{xx}| > |q_{yy}|$, so η known as asymmetry parameter, ranges from 0 to 1. It measures symmetry of the electric field gradient around the direction defined by maximum electric field gradient component (q_{zz}), $\eta = 0$ indicates axial symmetry. It is called asymmetry parameter because it is a measure of deviation of the electric field gradient tensor from axial symmetry. It does not involve any property of the nucleus and can be interpreted directly in terms of the electron distribution in molecules.

It is necessary to define the orientation of electric field gradient PAS in the molecular axis system for which three Euler angles are required. In the PAS the Hamiltonian is given by,

$$\mathcal{H}_{NQI} = e^2qQ/4\, [3\, I_z^2 - I^2 + \eta(I_x^2 - I_y^2)], \qquad [4.3]$$

The product $e^2qQ/\hbar$ is called the 'quadrupole coupling constant', which for a given nucleus with nuclear electric quadrupole moment eQ, measures the maximum component of the electric field gradient, eq at the nucleus.

For ^{14}N in an electric field gradient, nqi gives rise to three energy levels, and in zero magnetic field, three transitions are possible with pure nuclear quadrupole frequencies given by,

$$\nu_+ = e^2qQ(3 + \eta)/4$$
$$\nu_- = e^2qQ(3 - \eta)/4 \qquad [4.4]$$
$$\nu_o = (e^2qQ)\eta/2,$$

such that $\nu_o = \nu_+ - \nu_-$ and $\nu_+ > \nu_- > \nu_o$.

IV.4.2 Exact cancellation

ESEEM spectrum of ^{14}N is often indicative of 'exact cancellation condition'[11,12] that arises when its isotropic hyperfine interaction is equal to twice its nuclear Zeeman frequency, $|A_{iso}| = 2\nu_n$. Under this condition, the hyperfine and the nuclear Zeeman interactions "cancel" one another in one of the electron spin manifolds (figure IV-7), such that the modulation frequencies are dominated by ^{14}N-nuclear quadrupole interaction. This manifold yields three narrow, low frequency peaks in the ESEEM spectra where the two lower frequencies add to give the third. They are independent of the direction of external magnetic field, and thus, lead to the appearance of narrow peaks in ESEEM spectrum. The other electron spin manifold, where the electron-nuclear coupling and the Zeeman interaction are additive, typically gives rise to broad, or rapidly damped ESEEM features with the most prominent spectral component being that between the highest and lowest energy levels of the manifold. Because the two energy levels involved in this

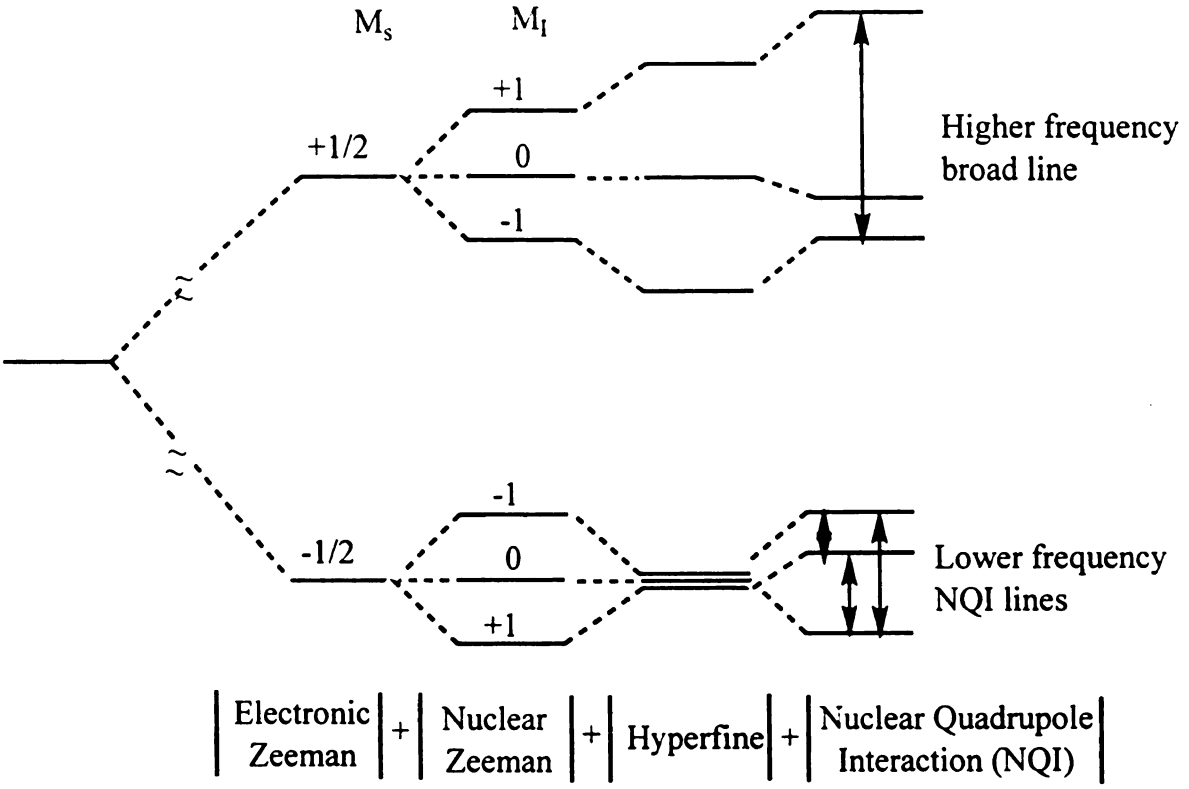

(a)

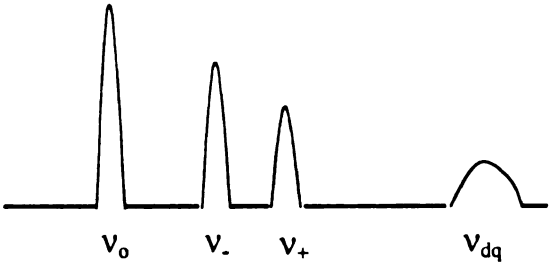

(b)

Figure IV-7: Energy level diagram for the interaction of an unpaired electron with a nucleus of ^{14}N (I = 1) at exact cancellation condition (a); and the expected spectrum (b).

modulation component have mostly $m_I = 1$ or $m_I = -1$ character, this peak is referred to as a "double quantum" ($\Delta m_I = \pm 2$) feature. The frequency of this broad component at exact cancellation is roughly four times the nuclear Larmor frequency, or 4 MHz in the case of ^{14}N at X-band. The other two $\Delta m_I = \pm 1$ transitions from this manifold are highly orientation dependent[13] and are not resolved in frozen samples. As long as the condition for exact cancellation is nearly satisfied, both the components e^2qQ and η, of the field gradient tensor can be obtained from the frequencies of the three sharp 'zero field' or 'pure' nuclear quadrupole resonance lines in ESEEM spectrum.

$$e^2qQ = 2(\nu_+ + \nu_-)/3; \text{ and } \eta = 3(\nu_+ - \nu_-)/(\nu_+ + \nu_-) \qquad [4.5]$$

Since ^{15}N is a spin I = 1/2 nucleus, it does not have a quadrupole moment, and its ESEEM is determined by hyperfine and nuclear Zeeman interactions only.

IV.4.3 Spherical model approximation

In case of glassy samples the echo signal has contributions from a distribution of electron-nucleus systems randomly oriented with respect to the external static magnetic field B_o. Therefore spatial averaging must be performed, which requires integration over all possible orientations of B_o with respect to a common molecular frame to which the nqi and hfi tensors have been transformed. In the simulation program used, the quadrupole tensor is rotated into the PAS of the hyperfine tensor. The Euler angles defining this transformation are determined by molecular geometry and are independent of the direction of B_o. The overall echo intensity in the PAS of hfi tensor is given by,

$$\langle E(t)\rangle = \frac{1}{4\pi}\int_o^{2\pi}\int_o^{\pi} E(\theta_o,\phi_o,t)\sin\theta_o d\theta_o d\phi_o \qquad [4.7]$$

where θ_o and ϕ_o are the polar angles defining the direction of B_o and $t = \tau$ or $t = \tau + T$ for two-pulse or three-pulse experiments respectively. When the unpaired spin interacts with more than one nuclear spin, then the resulting modulation is the product of the modulations due to each nucleus. In such a case a different set of Euler angles will be needed to transform nqi tensor of each nucleus to the PAS of the hfi tensor. The modulation is then given by,

$$\langle E(t)^N\rangle = \frac{1}{4\pi}\int_o^{2\pi}\int_o^{\pi}\prod_{i=1}^{N} E_i(\theta_o,\phi_o,t)\sin\theta_o d\theta_o d\phi_o \qquad [4.8]$$

Information about the geometry of the nuclei around the paramagnetic center should be available in order to evaluate the above integral. Extensive computing time may be required in order to evaluate the above integral. It is often useful to make 'spherical approximation' as described by Kevan et al.[14] to simplify the spatial averaging. When the dipolar interaction is smaller than the nuclear Zeeman term it can be assumed that the nuclei are arranged around the electron over a sphere at an 'effective' distance 'r', and θ_o is the angle between r and the magnetic field direction. The dependence on ϕ_o can be removed by shifting to a coordinate system rotating about z-axis. The mutual nuclear arrangement of the nuclei can be neglected in the averaging procedure, then equation 4.8 becomes,

$$\langle E(t)^N\rangle = \frac{1}{4\pi}\int_o^{2\pi}\int_o^{\pi}[E(\theta_o,t)]^N\sin\theta_o d\theta_o d\phi_o \qquad [4.9]$$

where $t = \tau$ or $\tau + T$ depending on whether it is a two-pulse or a three-pulse experiment. This equation represents the modulation due to N nuclei at the same orientation, which is not realistic in many cases. A more appropriate model is to consider the surrounding nuclei as randomly oriented over the sphere such that,

$$\langle E(t)\rangle^N = \left[\frac{1}{4\pi}\int_o^{2\pi} d\phi_o \int_o^{\pi} \sin\theta_o d\theta_o \, E(\theta_o, t)\right]^N \qquad [4.10]$$

This approximate spatial averaging method is known as 'spherical model'. It works well for distance $r > 4$ Å. This approximation can be safely made for cases where there are at least four or more coupled nuclei.

Our computer simulations made use of this spherical model approximation to the product rule for assembling the ESEEM spectra of the three magnetically coupled nitrogens of TTQ. The consequences of this approximation were tested for dithionite-reduced MADH. For this case, only two nitrogens contribute to the data and they do so in a nearly equivalent fashion.[2] To perform this task we modified our simulation software to simultaneously consider two $I = 1$ nuclei whose magnetic axes were related by a simple Euler angle rotation. If one considers the principal axes of both the hyperfine tensors to be at an angle of 45° with respect to one another, the ESEEM calculated with the precise formulation of the product rule yields results that are nearly identical with those obtained using the spherical model approximations. In the worst case, when both hyperfine principal axes are collinear or perpendicular, the errors made by using the spherical model approximation are modest. Because the X-ray crystal structure of MADH shows the planes of the indole and indole-quinone rings of oxidized TTQ to be at

an angle of 38° with respect to each other, use of the spherical model approximation is justified for our work.

IV.4.4 Theoretical Simulations

The analysis of ^{14}N ESEEM spectra involves 8 adjustable spin Hamiltonian parameters for each nucleus: three principal elements for the hyperfine tensor; the quadrupole coupling constant, e^2qQ/h, and its asymmetry parameter, η; and three Euler angles relating the orientation of the quadrupole tensor's principal axis system to that of the hyperfine tensor. Because the substrate-derived ^{14}N and N(1) of TTQ are likely near exact cancellation, good starting values for e^2qQ, η and $A_{iso} = 1/3(A_{\parallel} + 2A_{\perp})$ can be determined directly. Also, the assumption of an axial ^{14}N-hyperfine tensor reduces the number of parameters for each ^{14}N by one. Our simulations are then mostly aimed at determining the hyperfine anisotropy, $A_{dip} = 1/3(A_{\parallel} - A_{\perp})$, and the Euler angles that relate the two tensors. These parameters manifest themselves in the spectra of figures IV-4, IV-5 and IV-6 in that they control the lineshapes of broad peak in the 4-6 MHz region and influence the τ-suppression behavior of the ESEEM spectra. Our numerical simulations focused on accounting for the frequencies, lineshapes and relative amplitudes of the peaks and then, on understanding the changes that occurred as τ was varied.

Using equation 4.5, the nqi parameters for the substrate-derived ^{14}N nitrogen are estimated to be: e^2qQ, 1.7 MHz; and η, 0.6. Similarly for the N(1) nitrogen of TTQ, $e^2qQ = 3.0$ MHz and $\eta = 0.3$. When the anisotropic hyperfine interaction is small, A_{iso} can be estimated from the frequency of the double quantum peak, ν_{dq}, that arises from the

electron spin manifold where Zeeman and hyperfine fields are additive, using the following equation:[15]

$$A_{iso}^2/4 \mp \nu_n A_{iso} + (e^2qQ/4)^2 (3 + \eta^2) + \nu_n^2 - \nu_{dq}^2/4 = 0 \qquad [4.11]$$

Using the values of e^2qQ and η determined above, A_{iso} values of 2.1 and 6.1 MHz, and 2.5 and 6.5 MHz respectively, were estimated for the substrate-derived ^{14}N and N(1) of TTQ. The higher values of A_{iso} were neglected because they are far from the exact cancellation value of A_{iso}, 1.94 MHz at 3155G and did not give the desired ESEEM features.

Using these initial estimates for nuclear quadrupole and isotropic hyperfine coupling constants along with non-adjustable parameters dictated by our experimental conditions, computer simulations of the data shown in figures IV-4, IV-5 and IV-6 were undertaken. The ESEEM spectrum of each nitrogen was first simulated separately, and then combined using the product rule.[16] The Euler angles were initially set to zero and the estimated values of e^2qQ and η were varied to account for the positions of the narrow, low-frequency components whose characteristics are primarily determined by the nuclear quadrupole interaction. Then, hf tensor values were varied to obtain the correct position and width of the double quantum line. Finally, the Euler angles were varied to account for the relative intensities of the low-frequency components and shape of the double quantum peak. As the line shape of the double quantum feature depends on the hf tensor principal values as well as on Euler angles, they had to be adjusted simultaneously in order to obtain the best fit to the data.

Only two ^{14}N features at 0.8 and 1.2 MHz from the second indole nitrogen N(2) of TTQ$^{\bullet}$ are resolved (figure IV-6a). It is possible that these two frequencies represent ν_o and ν_- for N(2) and that ν_+ could overlap with ν_- from N(1) at 2.0 MHz. With this assumption, simulations were carried out using the above procedure. Because the "double quantum" peak from this nitrogen was not resolved at any of the τ values studied, we focused on simulations that showed small ν_{dq} amplitudes for this nucleus, presumably because of larger hf anisotropy than that characterizing N(1) or substrate-derived nitrogen. The other possibility that ν_{dq}'s from both N(1) and N(2) fall in 4.6-5.8 MHz region, did not predict observed intensities and dependence on τ.

The principal values of hf and nqi coupling parameters obtained from our computer simulations for substrate-derived nitrogen and the two nitrogens from TTQ, are listed in Table IV-1. Figure IV-8 shows the simulated frequency domain ESEEM spectra calculated using the experimental conditions and τ values of 219 (a), 365 (b) and 450 ns (c). The simulations account well for the frequencies, relative amplitudes and linewidths of major ESEEM features. The trends in amplitude changes that occur with τ are also in agreement with experiment. The chief shortcomings of our modeling are in accounting for the details of the double quantum features. Independent information on the symmetries of the hyperfine tensors as determined from two dimensional ESEEM measurements (HYSCORE)[17] would be beneficial here, but progress on such measurements has been impeded by long T_{1e} of the MADH semiquinone (> 1 sec).

Close examination of the data shown in figures IV-4, IV-5 and IV-6 fails to reveal contributions from substrate-derived ^{15}N. To support this observation, simulations were performed using ^{14}N-coupling parameters given in table IV-1 for the TTQ nitrogens along

with ^{15}N hyperfine couplings obtained by scaling the corresponding values measured for ^{14}N-substrate coupling by a factor $g_{^{15}N}/g_{^{14}N} = 1.403$. The results predicted that no distinct ^{15}N peaks would be resolved for ESEEM collected using the conditions of figures IV-3, IV-4 and IV-5. Simulations of 2-pulse data also showed that these measurements would not reveal ^{15}N contributions in the presence of deep modulation from the TTQ nitrogens.

Table IV-1: The assignment of the observed frequencies and the principal values of hf and nqi coupling parameters used in computer simulations for substrate-derived nitrogen and the two nitrogens from TTQ.

^{14}N nucleus	Resolved ESEEM Frequencies (MHz)	$A_\perp$	$A_{\|\|}$	A_{iso}	A_{dip}	e^2qQ/h	η	α	β	γ
Substrate	0.5, 1.0, 1.5, 4.3	2.1	3.1	2.4	0.3	1.7	0.5	0°	108°	60°
N(1)-TTQ	0.5, 2.0, 2.5, 4.8-5.1	2.6	3.2	2.8	0.2	3.0	0.3	0°	69°	0°
N(2)-TTQ	0.8, 1.2	1.4	3.0	1.9	0.5	2.1	0.7	0°	0°	0°
N(1) O-form*	0.4, 2.1, 2.5, 4.0-6.0	1.9	2.6	2.1	0.3	3.0	0.2	0°	60°	0°
N(2) O-form*	0.8, 1.8, 3.1, 5.0-6.0	1.2	2.1	1.5	0.3	3.2	0.6	0°	90°	0°

* Data taken from reference 2.

Figure IV-9 shows a comparison of echo amplitude modulations for the time domain data collected at $\tau = 219$ ns for the ^{14}N-semiquinone (solid line), with that obtained from our simulation (dashed line). The simulation was multiplied by a decay

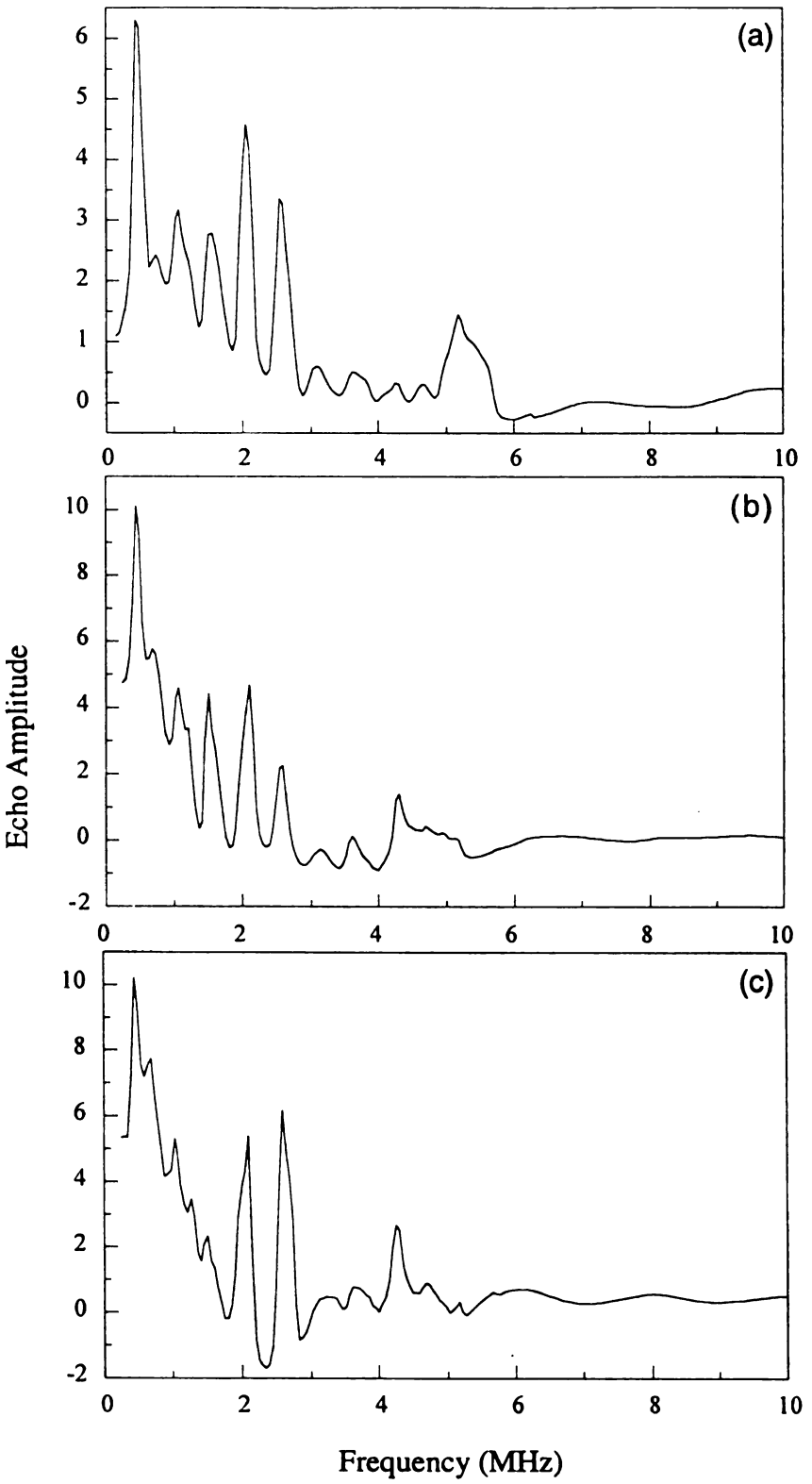

Figure IV-8: Cosine Fourier transformations of numerical simulations of three-pulse ESEEM data of $CH_3{}^{14}NH_2$-generated semiquinone in MADH (a) τ, 219 ns; (b) τ, 365 ns; (c) τ, 450 ns. The simulations were performed using three coupled ^{14}N nuclei, N(1), N(2) and substrate-derived N, whose hf and nqi coupling parameters are listed in table IV-1. Other simulation parameters: g_N, 0.4035; magnetic field strength, 315.5 mT. An isotropic electronic g-factor was assumed.

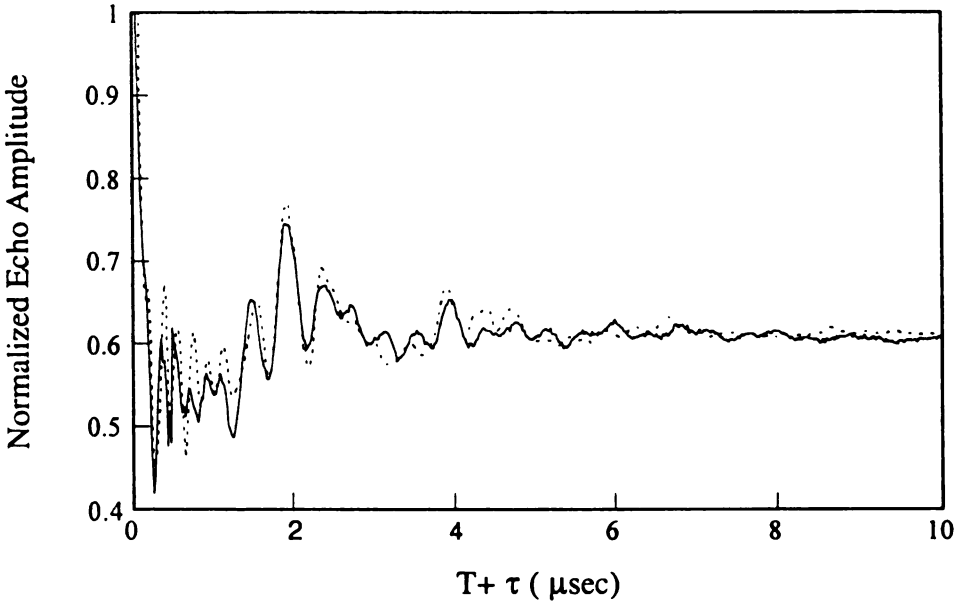

Figure IV-9: A comparison of the normalized three pulse electron spin echo envelope modulation amplitudes for ^{14}N-methylamine poised MADH semiquinone measured experimentally (solid line) at τ = 219 ns with that predicted by spectral simulation (dashed line) for the same τ-value.

function, $e^{-t/\tau}$, where τ was 4.5 μs. The depths of modulations in the time domain data and simulation agree well and show that the semiquinone is nearly pure N-form. The above ^{14}N-ESEEM analysis has provided two types of Hamiltonian parameters that report on the electronic structure of the TTQ-semiquinone. The hyperfine coupling parameters can be directly related to the structure of the highest occupied molecular orbital (HOMO) of the semiquinone in that the dipolar portion of the tensors are a measure of the unpaired spin density localized in the p^{π}-orbital of each coupled nitrogen. When an observed nuclear coupling constant is known to arise from a particular atomic orbital of the coupling atom in a free radical, the electron spin density of this atomic orbital can be obtained from the ratio of the measured coupling constant to that for the corresponding orbital of the free atom. Spin densities of p^{π} orbitals calculated in this manner are accurate only when the A_{dip} is entirely due to the spin density in the particular p^{π} orbital with its axis fixed in the crystal. Spin density in the perpendicular p orbitals of the coupling atom or the motion of the coupling orbital relative to the crystal axis or charge on the coupling atom influence the value of A_{dip} and hence affect the spin densities. In the present case, an estimate of the π-orbital unpaired spin density of each nitrogen in TTQ is obtained by dividing the A_{dip} values in table IV-1 by the corresponding value measured for atomic nitrogen, 47.8 MHz. Table IV-2 summarizes π-orbital unpaired spin densities located on the three nitrogens present in the N-form semiquinone and compares them to the values determined previously for the O-form radical.[2] All of the calculated p^{π} spin densities are small showing that our ^{14}N-ESEEM experiments are detecting only a small portion of the TTQ$^{\bullet}$ HOMO, and that the HOMO is delocalized over the framework of the cofactor. However, these numbers do reveal some of the details of

electronic structure changes triggered by substrate binding. For O-form semiquinone, the unpaired p^{π} spin densities on N(1) and N(2) nuclei of the cofactor are equal, consistent with a more uniform distribution. N-form semiquinone is characterized by an unpaired spin density on N(2) that is almost three times larger than that found for N(1). The presence of substrate derived amine has altered the HOMO, increasing the contribution of N(2) to the M.O. while reducing that of N(1).

Table IV-2: π-orbital unpaired spin densities located on the three nitrogens present in the N-form semiquinone and comparison with the values determined previously for the O-form radical.

Semiquinone	Electron densities		
	N-Substrate	N(1)-TTQ	N(2)-TTQ
N-form	0.007	0.004	0.011
O-form*	---	0.006	0.006

* Data taken from reference 2.

Molecular orbital calculations of spin densities and hyperfine coupling constants were performed using SPARTAN and Gaussian 98 programs on N- and O-semiquinone forms of a model compound structurally related to TTQ (figure IV-10). This model compound has been previously synthesized and characterized by Itoh, et.al.[18-20] The notations N1 and N2 in figure IV-10 are the notations used in SPARTAN and Gaussian 98 programs, and they are not the same as N(1) and N(2) used in numerical simulations. In earlier studies molecular orbital calculations and density functional analyses have been

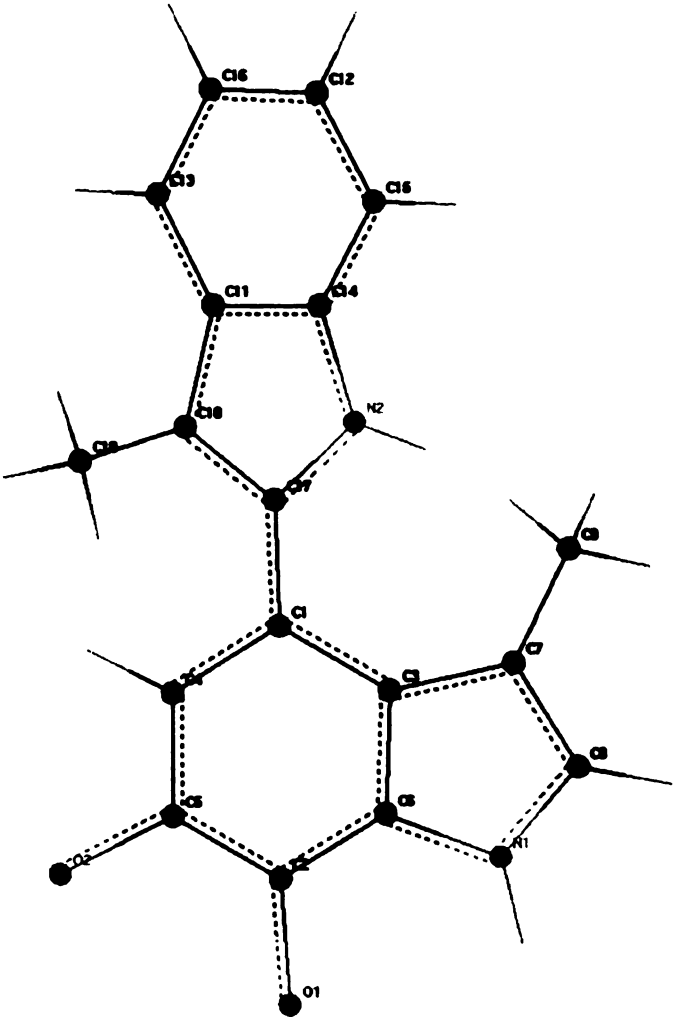

Figure IV-10: Structure of the oxidized form of the model compound of TTQ cofactor of MADH used in theoretical calculations. Atoms are labeled as, nitrogen in magenta, oxygen in red, carbon in black and hydrogen in yellow.

performed on the tryptophan radical and benzosemiquinone anion radicals providing the molecular geometries, electron spin densities and approximate hf coupling values.[21-29] In going from these molecules to the model compound of TTQ, due to increased number of heavy atoms (atoms other than hydrogen) in the molecule, the calculations become more expensive. The presence of possible hydrogen bonding is also expected to change these molecular properties to a great extent. The density functionals and semiemperical theory, that can calculate molecular properties to a reasonably good approximation for these planar molecules, may not yield satisfactory results for the non-planar model compound of TTQ. This is because all these methods suffer from having poor electron correlations. For obtaining good quantitative picture and for calculating the values of isotropic hyperfine and anisotropic hyperfine coupling constants for the three nitrogens of N-form semiquinone, methods based on correlated coupled cluster theory need to be used. These methods treat electron correlations to better approximations and are expected to give more realistic results but are exorbitantly expensive for a large molecule like model coumpound of TTQ. However, the results obtained from the semiemperical calculations give a qualitative outlook about the spin densities in this molecule.

The calculations were performed using Hartree-Fock, density functional theory and semiemperical theory with UHF, B3LYP, 6-31G* basis sets for comparison.[30,31]. Geometry optimization led to minimum steric energy when the dihedral angle of the two indole planes was 35.9° for the N-semiquinone form and 35.2° for the O-semiquinone form of the model compound. The EPR spectroscopic measurements on this model compound had suggested a partial π-conjugation between the indole and indo-quinone rings and a non rigid conformation.[19] The calculated spin density for the O-form is

plotted in figure IV-11, where it can be seen that the extent of the 0.002 e/au^3 spin density contour around N1 and N2 are almost same, and the unpaired spin density is equally distributed on both the nitrogens of the TTQ ring system which agrees with the results of previous ESEEM studies.[2] Calculations using unrestricted Hartree-Fock model were found to be less accurate. The calculated spin density for the N-form is plotted in figure IV-12. Figure IV-13 is a plot of the electron density and HOMO of the N-form showing that the HOMO is spread over the entire molecule. Figure IV-14 is a similar plot for the O-form. Using the results of this calculation the N(1) and N(2) nitrogens from theoretical simulations can be identified. The indole nitrogen has the higher spin density, which favors the idea that the electron transfer from MADH to amicyanin follows a path involving this indole ring that is nearest to Cu of amicyanin (figure I-4). An ET from the indole ring would be more favorable as compared to the other possible path involving direct transfer from the reduction site at C6. As seen from figure I-4 the most direct distance between the site of radical generation, the substrate-derived nitrogen, and Cu is about 16.8 Å and a direct ET would involve a large through-space electron jump which is less favorable because the efficiency of ET through space is relatively very poor.

The alterations of the HOMO for the TTQ semiquinone caused by the presence of substrate-derived amine are interesting in the light of the different electron transfer (ET) rates to amicyanin measured for N- versus O-form quinol and semiquinone intermediates of MADH.[32] Electron transfer from the N-semiquinone is slower than from the O-semiquinone. Conversely, electron transfer from the N-quinol, which yields the N-semiquinone as a product, is faster than from the O-quinol. The differences in the ET rates from the N- and O-semiquinone forms appear to be due to differences in their

Figure IV-11: Calculated spin density for the O-semiquinone form of the model compound. Calculations used semiemperical model and UHF basis sets in SPARTAN software program; isosurface value, 0.002. Atoms are labelled as, nitrogen in magenta, oxygen in red, carbon in gray and hydrogen in white.

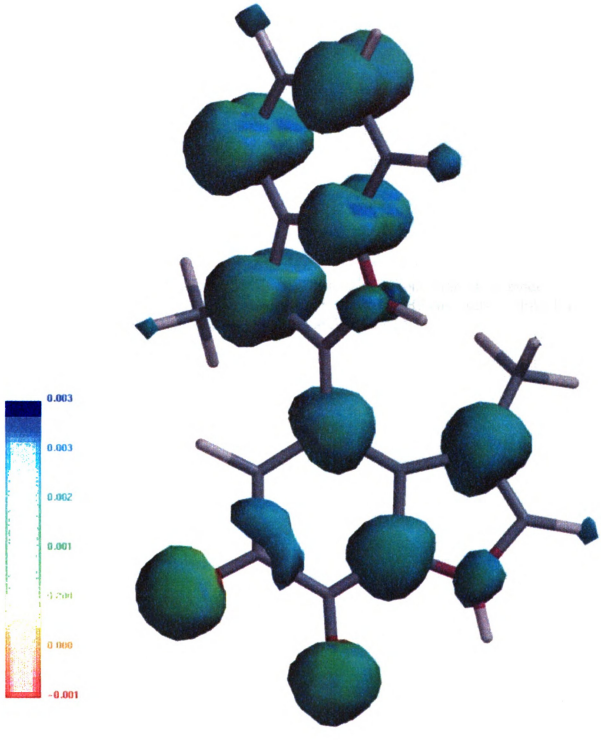
0.003
0.003
0.002
0.001
0.000
-0.001

Figure IV-12: Calculated spin density for the N-semiquinone form of the model compound. Calculations used semiemperical model and UHF basis sets in SPARTAN software program. Atom labeling is same as in figure IV-11.

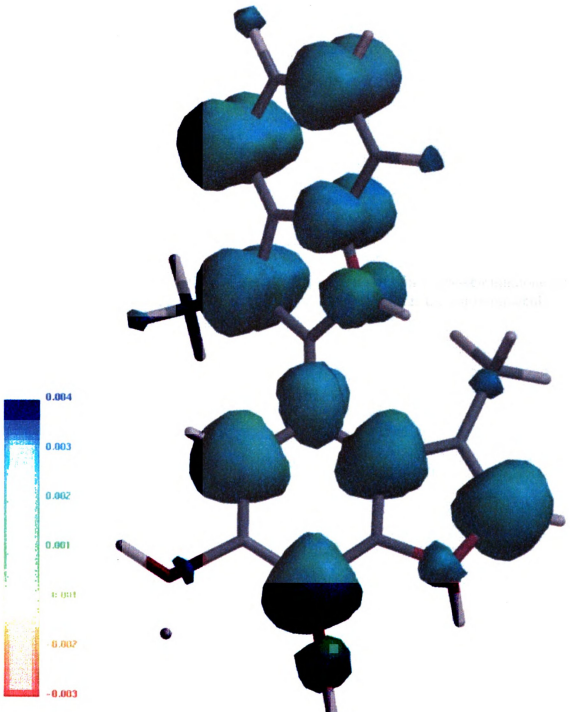
0.004
0.003
0.002
0.001
0.002
-0.003

Figure IV-13: A plot of the electron density and HOMO for the N-semiquinone form of the model compound showing that the HOMO is spread over the entire molecule. Atom labeling is same as in figure IV-11.

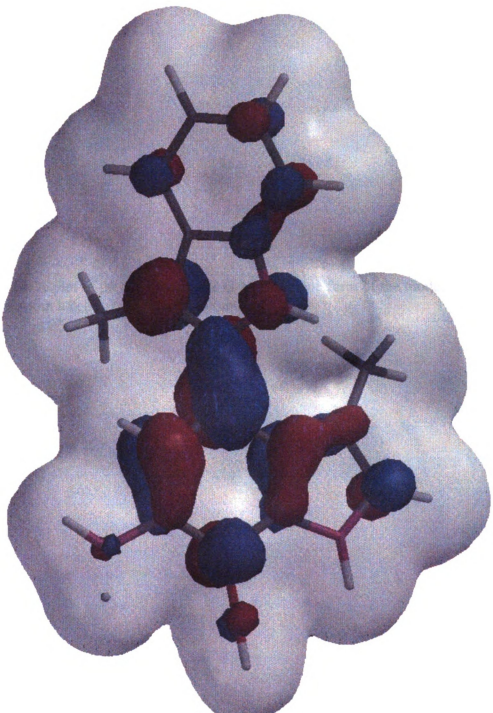

Figure IV-14: A plot of the HOMO for the O-semiquinone form of the model compound. Atom labeling is same as in figure IV-11.

redox potentials.[32] The basis for differences in the reaction rates of the N- and O-form quinols, which yield the corresponding semiquinone forms as products, is more difficult to interpret because the reaction of the N-quinol is gated by the deprotonation of the substrate-derived amino group on TTQ[33] (discussed later), whereas ET reactions from dithionite-reduced quinol and semiquinone forms of MADH are rate-limited by the ET event. In addition to redox potential, two other parameters which determine ET rates are the electronic coupling (H_{AB}) related to the distance that the electron must travel and the reorganizational energy (λ) composed of solvational and vibrational components.[34] The covalent incorporation of substrate-derived N into TTQ affects the rate and standard free energy (ΔG°) for the ET reaction from the TTQ semiquinone by altering its redox potential, but it does not alter λ and H_{AB} associated with ET from TTQ to amicyanin which are same as in the case of the ET reactions of the dithionite-reduced O-quinol and O-semiquinone forms. An important result from this study is that the unpaired electron spin density in the TTQ semiquinone is delocalized over the framework of TTQ. This suggests that the starting point for the electron transfer reaction may be any point on the cofactor, including the edge of the Trp108 indole ring, which is closest to amicyanin. The asymmetry of the spin density raises an interesting question of whether the observed differences in the HOMO for different TTQ forms would contribute to differences in H_{AB} for electron transfer reactions from different redox forms. Another interesting question is to what extent the electronic structure of the TTQ semiquinone, relative to that of the oxidized and reduced forms, contributes to the λ associated with electron transfer reactions that involve the semiquinone TTQ as a reactant or product. The electron transfer reactions of MADH exhibit relatively large values of $\lambda > (2\ eV)$,[32] which may be

reflective of the kinetic complexity of this reaction. The ET from TTQ to amicyanin may be a coupled ET in which a rate-limiting ET event is preceded by a relatively rapid but unfavorable non-ET reaction step.[35] For such a reaction, the experimentally determined λ value will include contributions from both the λ associated with the ET as well as the energetics associated with the non-ET step. A possible non-ET step could be a change in dihedral angle between indole and indolquinone rings in order to optimize the system for ET. The need for such a change in dihedral angle was also suggested on the basis of studies with TTQ model compounds,[19] and from the molecular orbital calculations and geometry optimization of the model compound in this study. Such a reaction would be expected to occur at the expense of large amount of energy and would contribute significantly towards increasing the λ value. These new data will form the basis for future studies to elucidate any correlation between electron transfer properties and the electronic properties of this and other organic redox cofactors.

The other group of ^{14}N-Hamiltonian parameters derived from this work are nuclear quadrupole interaction (nqi) parameters, e^2qQ and η. Although the ^{14}N nucleus has a small quadrupole moment, this interaction can often be substantial because of the large electric field gradient created by the atom's 2p electrons.[36] For the tricoordinate, planar geometries that describe the bonding of the ^{14}N nuclei of the TTQ semiquinone, the principal axis of the electric field gradient is directed along the $2p^{\pi}$ orbital of the atom, perpendicular to the three sp^2 hybrid orbitals that characterize the sigma bonding. Using this simple Townes-Dailey description of the interactions, the value of e^2qQ, the quadrupole coupling constant, can be related to the electron occupancy of the nitrogen $2p^{\pi}$ orbital.[37] If this orbital houses 2 electrons, the e^2qQ value is > 4 MHz. For the

indole nitrogen of tryptophan powder e^2qQ is 3.0 MHz, which corresponds to a $2p^{\pi}$ orbital occupancy of about 1.75.[38] The e^2qQ values measured for the TTQ nitrogens of the O-form semiquinone are 3.0 (N(1)) and 3.2 (N(2)), indicating that the occupancy of the p^{π} orbital on these heteroatoms is not greatly affected by the protein environment or the difference between the electronic structure of the cofactor and the amino acid (tryptophan) model compounds.

The asymmetry parameter η is used to describe the degree of rhombicity in the electric field gradient. η ranges from 0, for an axial interaction, to 1 for the completely rhombic case.[36] For tryptophan powders, the indole nitrogen is found to have $\eta = 0.18$ indicative of an axial tensor and a measure of the 'equivalence' of the C-N and N-H bonds. For the O-form semiquinone, Warncke, et al. found that η for N(1) was 0.2, identical to that of the tryptophan model, while the N(2) asymmetry was 0.6 indicating an asymmetry likely caused by hydrogen-bonding to a peptide. The x-ray crystal structure of oxidized MADH shows nearly equivalent hydrogen bonding interactions for both the indole and the indole-quinone nitrogens.[39] The results of Warncke, et al. on O-form semiquinone had shown that only one of these interactions is important for reduced cofactor.[2]

The differences observed in ^{14}N hyperfine couplings between O- and N-form semiquinones are mirrored by changes in e^2qQ. For the N(1) nitrogen of N-form $TTQ^{\bullet}$, both e^2qQ and η were determined to be 3.0 MHz and 0.3, respectively, and remain close to the indole model compound values. The e^2qQ values for the N(2) nitrogen dropped from 3.2 MHz for the O-form to 2.1 MHz for the substrate reduced enzyme. Using the

analysis results of Edmonds and Speight, this decrease in e^2qQ can be interpreted as a decrease in the N(2) $2p^{\pi}$ orbital population from ~1.75 to about 1.63. This decrease is supportive of our ESEEM simulation results for N(2) that attribute the lack of a 'double quantum' peak to an increase in hyperfine anisotropy or $2p^{\pi}$ unpaired electron spin density. The asymmetry parameter for N(2) was found to be nearly 0.7, essentially unchanged from the value determined for the O-form.

The ESEEM spectra of the N-form semiquinone also yielded a well resolved set of resonances due to substrate derived nitrogen. The measured isotropic coupling constant is 2.4 MHz, in good agreement with value estimated from samples prepared by comproportionation and studied previously by ESEEM.[10] This value compares well to those measured for the TTQ nitrogens, 2.7 (N(1)) and 1.9 (N(2)), and definitely shows that the substrate-derived nitrogen is covalently bound to the TTQ semiquinone. The low value of e^2qQ, 1.7 MHz and the deviation of the asymmetry parameter from that expected for an axial interaction ($\eta = 0.5$) are commensurate with the incorporation of the substrate nitrogen into the π-system of the TTQ semiquinone and our previous proposal that the nitrogen is an imine-like species.[33,40] The low value of e^2qQ dictates that all of the substrate derived nitrogen's electrons are involved in bonding interactions, and agrees well with the e^2qQ value determined for the substrate derived nitrogen of the topa-semiquinone cofactor of copper amine oxidases.[41,42] For these systems a combination of ^{14}N- and ^{2}H-ESEEM, and ^{1}H-ENDOR spectroscopies were used to show that the nitrogen derived from amine substrate was bound to the topa-quinone cofactor as an imine-like species with one strongly, and one weakly coupled exchangeable proton accounting for the bonding about the heteroatom.[42]

For MADH, an imine-like semiquinone species with one strongly, and one weakly coupled exchangeable proton is very consistent with the chemical reaction mechanism that we have proposed for the deprotonation reaction that gates the electron transfer from the N-quinol MADH to amicyanin.[33] It was proposed that rate-limiting deprotonation of the substrate-derived amino group on reduced TTQ was required to activate the system for rapid electron transfer. This deprotonation of TTQ-bound $-NH_2$ requires a monovalent cation at the active site to stabilize the transient $-NH^-$ intermediate from which electron transfer occurs to yield the =N–H imino-semiquinone product. Thus, in the semiquinone state the active site residue which removed the proton from $-NH_2$ will still be in close proximity to the =N–H of the semiquinone and in a position to provide this same proton for hydrogen bonding to the imino-semiquinone nitrogen. This would yield one strongly (covalent), and one weakly (H-bonded) coupled exchangeable proton.

IV.5 Studies on aromatic amine dehydrogenase

Aromatic amine dehydrogenase (AADH) is an enzyme that uses the same tryptophan tryptophylquinone (TTQ) cofactor as methylamine dehydrogenase (MADH). Like MADH it also catalyzes the oxidative deamination of a distinct class of primary amines. AADH is most specific for phenylethylamines, and is produced by *Alcaligenes faecalis* and allows growth on phenylethylamine as a carbon source. AADH uses a blue copper protein, azurin, to mediate electron transfer to cytochromes homologous to the role of amicyanin in *P. denitrificans*. Recent studies have shown that there is spectroscopic evidence for a common electron transfer pathway for these two tryptophan tryptophylquinone enzymes.[43] ^{13}C- and ^{15}N-NMR studies of the reaction

of AADH with methylamine have also demonstrated that the products of the reductive half-reaction are an equivalent of formaldehyde hydrate and a reduced aminoquinol form of the tryptophan tryptophylquinone (TTQ) cofactor which contains covalently bound substrate-derived N. The substrate-derived aminoquinol nitrogens of AADH and MADH exhibit ^{15}N chemical shifts, which are separated by approximately 7 ppm. and may reflect differences in the active-site mediated electrostatic environment of the aminoquinol N. The aminoquinol of AADH is also less stable against reoxidation than that of MADH, suggesting that the active-site environments of the respective enzymes influence the relative reactivity of the aminoquinols.[44]

The overall structural and functional similarities suggest that AADH and MADH may have evolved from a common ancestor to yield enzymes with distinct substrate specificities. A comparison of the experimental data of the N-form (^{14}N- and ^{15}N-substituted) and O-form of the semiquinone from AADH and those from MADH should be useful in further understanding the reaction mechanism involved in AADH.

Cw-EPR (figure IV-15) and three pulse ESEEM experiments were performed on the AADH O-form and N-form semiquinones. Unfortunately, the echo intensities for the AADH samples were weak and a comparison of the three pulse ESEEM spectra for the ^{14}N- and ^{15}N-substituted semiquinones showed no significant difference from that of the O-form spectrum; only small changes in the intensities of the peaks were observed and there was absence of any strong peaks due to the substrate-derived nitrogen which were clearly seen in the MADH data. The reason for this could be that the poising of semiquinone did not lead to the formation of the N-forms. But EPR-spectra of N-forms were broadened to a great extent as compared to the O-form, indicating the presence of

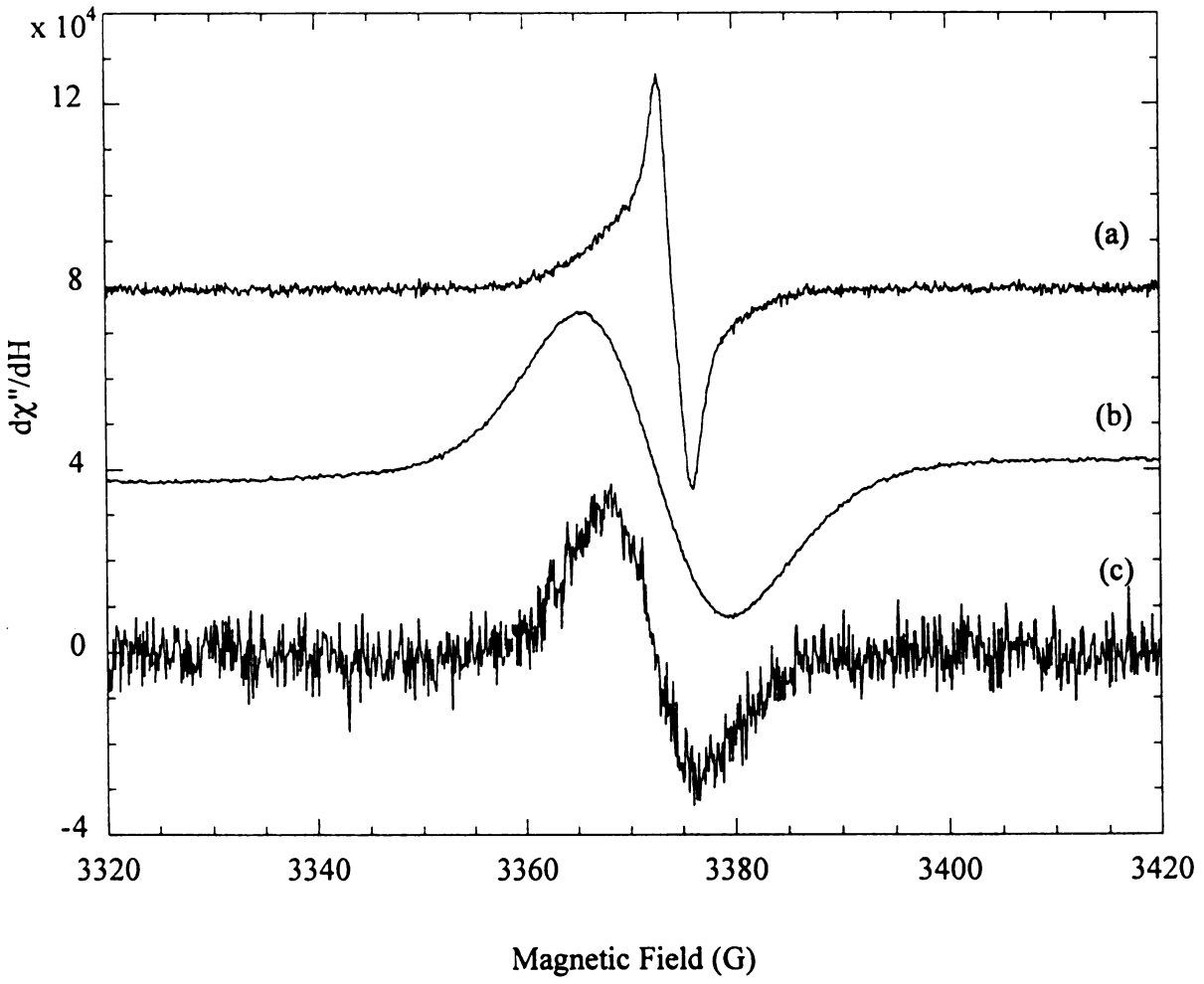

Figure IV-15: Continuous-wave EPR spectra of the semiquinone forms of aromatic amine dehydrogenase from *Alcaligenes faecalis* generated by dithionite addition (O-form) (a), ^{14}N-methylamine addition followed by illumination (b), and ^{15}N-methylamine addition followed by illumination (c). Spectra were collected under the following conditions: microwave power, 2.0 mW; microwave frequency, 9.484GHz; modulation frequency, 100 kHz; modulation amplitude, 0.1 mT; sample temperature, 20 K; and number of scans averaged, 25.

extra coupling. It is possible that since the concentration of N-forms were very small in these samples, (as reflected in the poor echo amplitude) their signals were obscured by the ^{14}N-peaks near exact cancellation arising from the indole and indo-quinone nitrogen atoms of TTQ cofactor.

IV.6 Conclusions

The ESEEM experiments and analyses presented here show that the semiquinone species obtained by light-induced oxidation of substrate-reduced MADH contains a covalently bound nitrogen atom that is derived from substrate methylamine. The nuclear quadrupole coupling constant, e^2qQ, measured for this substrate-derived nitrogen is consistent with that determined for the topa-semiquinone species of amine oxidases[41] and is very distinct from the value measured for methylamine by NQR spectroscopy.[36] It is likely that this substrate-derived nitrogen exists as imine nitrogen in the TTQ semiquinone, with the lone pair of electrons that reside in the remaining sp^2 hybridized orbital involved in the formation of a strong hydrogen bond with an available proton-donor. Furthermore, the match between the depths, or intensities, of the ESEEM predicted by our simulations and the experimental data provides strong evidence that the intermediate species prepared using the light-induced oxidation procedure developed by Zhu and Davidson[1], is pure N-form semiquinone. It is important to note that these results were obtained using stoichiometric amounts of substrate reacted with enzyme rather than the 10^4 to 10^6 molar excesses that are typical in cation binding studies.[6,45,46]

The broadening of the cw-EPR lineshape found for substrate-reduced semiquinone when compared to that of dithionite-reduced enzyme reflects changes in the electronic

structure of TTQ$^{\bullet}$ that are a consequence of the substitution of substrate nitrogen for the C6 oxygen atom. The hyperfine couplings measured in this work for the three nitrogen atoms of the semiquinone provide details of how the highest occupied molecular orbital of this chemical intermediate are affected by substrate addition. Further characterization of this species by proton ENDOR spectroscopy will provide a detailed picture of the HOMO and key information for understanding how the electronic structure of the TTQ semiquinone in MADH effects the rates and mechanisms of electron transfer from different redox forms of MADH to amicyanin.

List of References

1)Zhu, Z.; Davidson, V. L. *Biochim. Biophys. Acta.* **1998**, *1364*, 297-300.

2)Warncke, K.; Brooks, H. B.; Hong-in, L.; McCracken, J. L.; Davidson, V. L.; Babcock, G. T. *J. Am. Chem. Soc.* **1995**, *117*, 10063-10075.

3)Husain, M.; Davidson, V. L. *J.Biol. Chem.* **1985**, *260*, 14626-14629.

4)Eady, R. R.; Large, P. J. *Biochem. J.* **1968**, *106*, 245-255.

5)Husain, M.; Davidson, V. L.; Gray, K. A.; Knaff, D. B. *Biochem.* **1987**, *26*, 4139-4143.

6)Gorren, C. F. A.; Moenne-Loccoz, P.; Backes, G.; Vries, S.; Loehr, J. S.; Duine, J. A. *Biochemistry* **1995**, *34*, 12926-12931.

7)McCracken, J.; Shin, D.-H.; Dye, J. L. *Appl.Magn. Reson.* **1992**, *3*, 305-316.

8)Mims, W. B. *J. Magn. Reson.* **1984**, *59*, 291-306.

9)Mims, W. B. *Phys. Rev. B: Solid State* **1972**, *5*, 2409-2419.

10)Warncke, K.; McCracken, J. L.; Brooks, H. B.; Babcock, G. T.; Davidson, V. L. *J. Am. Chem. Soc.* **1993**, *115*, 63-64.

11)Mims, W. B.; Peisach, J. *J. Chem. Phys.* **1978**, *69*, 4921-4930.

12)Flanagan, H. L.; Singel, D. J. *J. Chem. Phys.* **1987**, *87*, 5606-5616.

13)Colaneri, M.; Peisach, J. *J. Am. Chem. Soc.* **1992**, 114, 5335-5339.

14)Kevan, L.; Bowman, M. K.; Narayana, P. A.; Boeckman, R. K.; Yudanov, V. F.; Tsvetkov, Y. D. *J. Chem. Phys.* **1975**, *63*, 409-416.

15)Cosgrove, S. A.; Singel, D. J. *J. Phys. Chem.* **1990**, *94*, 8393-8396.

16)Dikanov, S. A.; Shubin, A. A.; Parmon, V. N. *J. Mag. Reson.* **1981**, *42*, 474-487.

17)Dikanov, S. A.; Bowman, M. K. *J. Magn. Reson. A* **1995**, *116*, 125-128.

18)Itoh, S.; Ogino, M.; Komatsu, M.; Y., O. *J. Am. Chem. Soc.* **1992**, *114*, 7294-7295.

19)Itoh, S.; Ogino, M.; Haranou, S.; Terasaka, T.; Ando, T.; Komatsu, M.; Y., O.; Fukuzumi, S.; Kano, K.; Takagi, K.; Ikeda, T. *J. Am. Chem. Soc.* **1995**, *117*, 1485-1493.

20)Itoh, S.; Y., O. *Meth. Enzymol.* **1995**, *258*, 164-176.

21)Hoffman, B. M.; Roberts, J. E.; Kang, C. H.; Margoliash, E. *J. Biol. Chem.* **1981**, *24*, 6556-6564.

22)Grafton, A. K.; Wheeler, R. A. *J. Phys. Chem.* **1997**, *101*, 7154-7166.

23)Walden, S. E.; Wheeler, R. A. *J. Phys. Chem.* **1996**, *100*, 1530-1535.

24)O'Malley, P. J. *Chem. Phys. Lett.* **1996**, *262*, 797-800.

25)O'Malley, P. J.; Collins, S. J. *Chem. Phys. Lett.* **1996**, *259*, 296-300.

26)O'Malley, P. J. *J. Chem. Phys. A* **1997**, *101*, 6334-6338.

27)O'Malley, P. J. *Chem. Phys. Lett.* **1997**, *274*, 251-254.

28)O'Malley, P. J. *Chem. Phys. Lett.* **1998**, *291*, 367-374.

29)O'Malley, P. J. *Chem. Phys. Lett.* **1998**, *285*, 99-104.

30)Becke, A. D. *Phys. Rev. A* **1988**, *38*, 3098.

31)Lee, C.; Yang, W.; Parr, R. G. *Phys. Rev. B* **1988**, *37*, 785.

32)Bishop, G. R.; Davidson, V. L. *Biochemistry* **1998**, *37*, 11026-11032.

33)Bishop, G. R.; Davidson, V. L. *Biochemistry* **1997**, *36*, 13586-13592.

34)Marcus, R. A.; Sutin, N. *Biochim. Biophys. Acta* **1985**, *811*, 265-322.

35)Davidson, V. L. *Biochemistry* **1996**, *35*, 14035-14039.

36)Lucken, E. A. C. *Nuclear Quadrupole Coupling Constants*; Academic Press: London, 1969.

37)Townes, C. H.; Dailey, B. P. *J. Chem. Phys.* **1949**, *17*, 782-796.

38)Edmonds, D. T.; A., S. P. *J. Mag. Res.* **1972**, *6*, 265-273.

39)Chen, L.; M., D.; Durley, R. C.; Y., C. A.; E., L. M.; Davidson, V. L.; Mathews, F. S. *J.Mol.Biol.* **1998**, *276(1)*, 131-49.

40)Zhu, Z.; Davidson, V. L. *J. Biol. Chem.* **1998**, *273*, 14254-14260.

41)McCracken, J. L.; Peisach, J.; Cote, C. E.; McGuirl, M. A.; Dooley, D. M. *J. Am. Chem. Soc.* **1992**, *114*, 3715-3720.

42)Warncke, K.; McCracken, J. L.; Babcock, G. T.; McGuirl, M. A.; Dooley, D. M. *J. Am. Chem. Soc.* **1994**, *116*, 4028-4037.

43)Edwards, S. L.; Davidson, V. L.; Hyun, Y.-L.; Wingfield, P. T. *J. Biol. Chem.* **1995**, *270*, 4293-4298.

44)Bishop, G. R.; Zhu, Z.; Whitehead, T. L.; Hicks, R. P.; Davidson, V. L. *Biochem. J.* **1998**, *330*, 1159–1163.

45)Gorren, C. F. A.; Duine, J. A. *Biochemistry* **1994**, *33*, 12202-12209.

46)Kuusk, V.; McIntire, W. S. *J.Biol. Chem.* **1994**, *269*, 26136-26143.

CHAPTER V

RESOLUTION ENHANCEMENT OF ECHO DETECTED EPR SPECTRUM OF MANGANESE-ETHYLENE (DINITRILO) TETRAACETATE BY MAGNETIC FIELD VECTOR JUMP AT X-BAND

V.1 Introduction

The resolution of powder spectra in EPR can often be improved by changing the microwave frequency and magnetic field strength where resonance occurs. Electron spin echo detected EPR spectroscopy with magnetic field vector jumps provides an alternative means for enhancing the resolution of powder spectra.[1] In this method specific molecular orientations are selected for resonance by inducing sudden changes in the direction of the static magnetic field keeping its magnitude constant, during the time at which refocusing pulses are applied in two- or three-pulse electron spin echo experiments. The resulting ESE-detected EPR spectra show improved resolution that should allow more straightforward analysis of magnetic coupling parameters. This method was used to explore the possibility of resolution enhancement of the echo detected EPR Spectrum of Manganese-ethylene (dinitrilo) tetraacetate.

Mn(II) acts as a cofactor in many enzymes and can serve as a substitute for a required Mg(II) cofactor. ^{55}Mn(II) (S = 5/2, I = 5/2) is a d^5 ion and in the high spin state it has five unpaired electrons. In the absence of an external magnetic field the degeneracy of its six spin states is partially lifted by a zero-field splitting interaction to yield three Kramer doublets denoted by $M_s = \pm 5/2, \pm 3/2$, and $\pm 1/2$. The origin of this zero field splitting interaction is the electron-electron dipolar interaction between the five unpaired Mn(II) valence electrons. Mn(II) complexes that show non-cubic symmetry, have zfs

interactions that complicate their EPR spectra, making it difficult to extract structural information. The complex chosen for this study was manganese-ethylene (dinitrilo) tetraacetate (Mn-EDTA) complex. This complex is expected to have large anisotropy due to zfs, which makes it a suitable system to study possible resolution enhancement by the application of field vector jumps. In the presence of a magnetic field, ^{55}Mn(II) gives rise to 6 non-degenerate electron spin states that are split into 6 levels by the ^{55}Mn(II) hyperfine interaction. The resulting 36 energy levels support 30 allowed EPR transitions (fine structure) according to the selections rules, $\Delta M_s = \pm 1$, $\Delta m_I = 0$, where M_s and m_I are electron and nuclear spin quantum numbers respectively (figure V-1). The laboratory field competes with the internal field from the Mn nucleus for alignment of spins, and spacings of the energy levels are dependent on the orientation of the molecular axis in the laboratory field. Thus, the EPR spectrum is orientation dependent. This orientation dependence of resonance frequencies of the allowed transitions in the case of isotropic g, can be expressed as:

$$\begin{aligned} B_{res}(\theta) = B_o &- D\,(M_s - 1/2)\,[3\mathrm{Cos}^2\theta - 1] \\ &+ (D^2/2B_o)\,[4S(S+1) - 24M_s(M_s - 1) - 9]\,\mathrm{Sin}^2\theta\mathrm{Cos}^2\theta \\ &- (D^2/8B_o)\,[2S(S+1) - 6M_s(M_s - 1) - 3]\,\mathrm{Sin}^4\theta \\ &- (A^2/2B_o)\,[I(I+1) - m_I^2 + m_I(2M_s - 1)] + [\text{higher order terms}]\ \text{Gauss} \end{aligned} \qquad \ldots[5.1]$$

where, A is the hyperfine coupling, D is the axial component of the zfs parameter (section V-5), S and I are the effective electron and nuclear spins of Mn, and θ is the angle between the principal axis of the zfs tensor and the applied static magnetic field B_o.

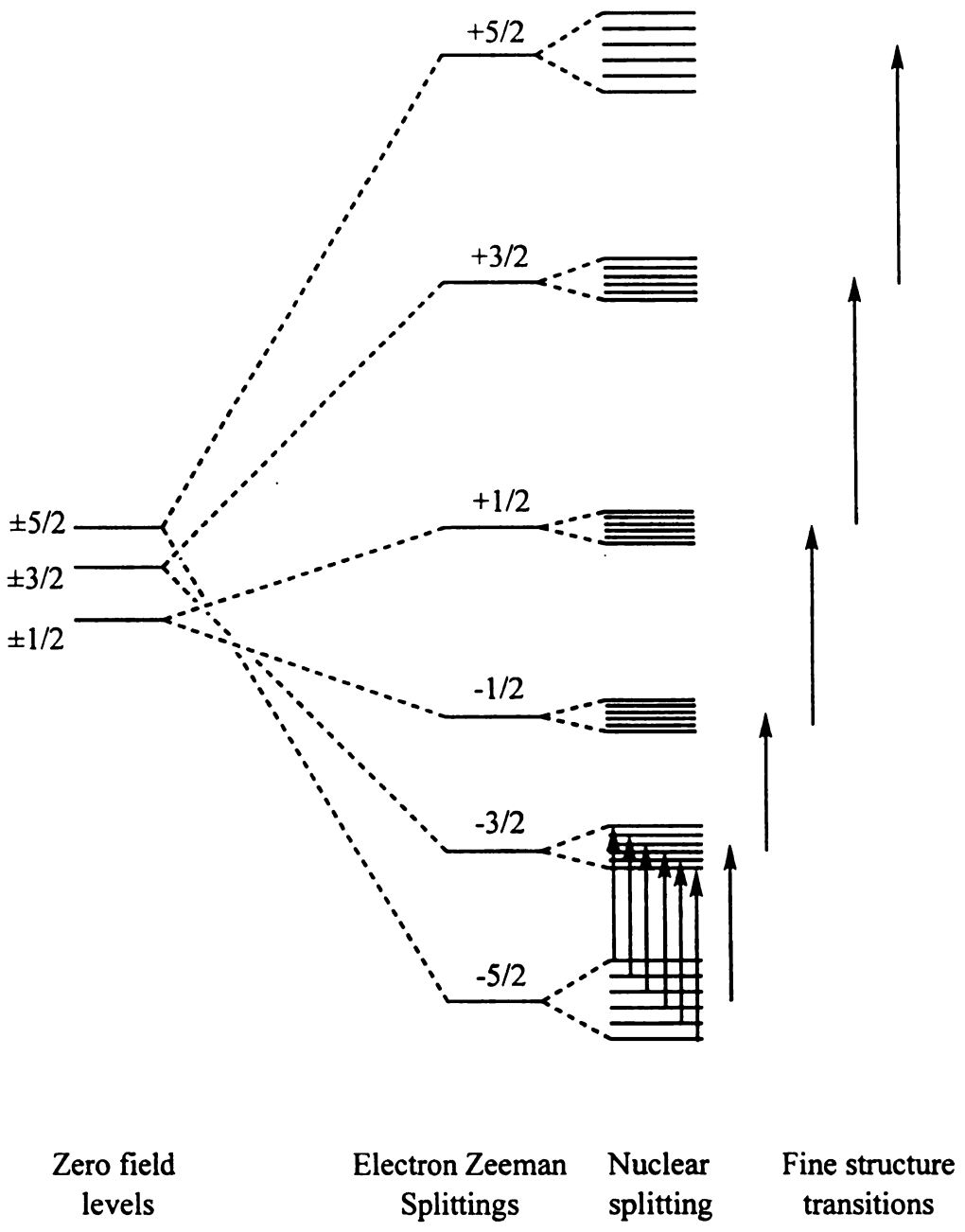

Figure V-1: An isotropic energy level diagram at fixed field for Mn(II)

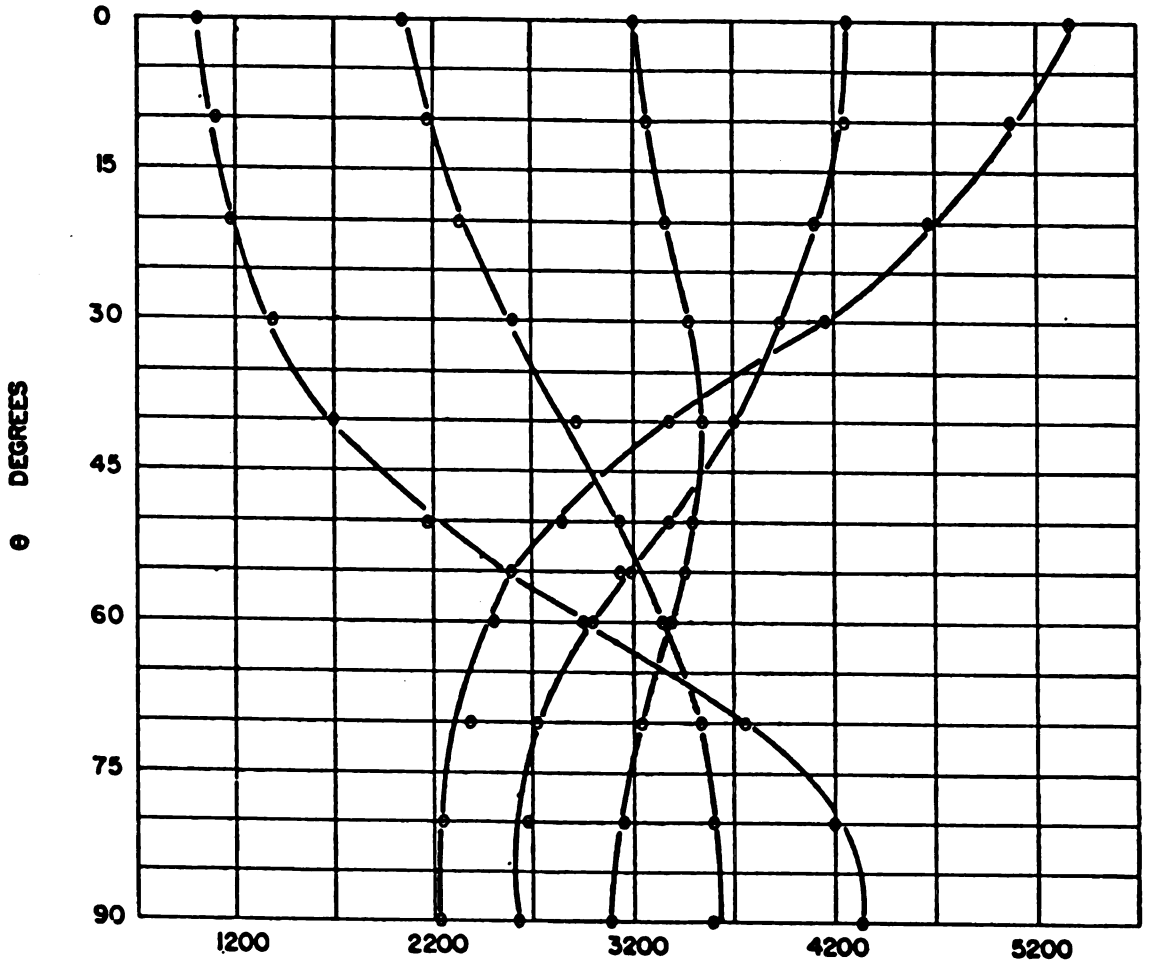

Figure V-2: Angular dependence of the centers of the sextets in the five fine-structure transitions (as shown in figure V-1) of Mn(II) in KN_3. Taken from reference 2.

A powder spectrum can be obtained by integrating equation 5.1 over all orientations of the magnetic field. In such a spectrum if the transition probability for a particular transition remains constant as the angle θ is varied, peaks are expected to occur at field positions corresponding to "turning points" of $B_{res}(\theta)$. These "turning points" are magnetic field positions where $dB_{res}(\theta)/d\theta$ goes to zero. Because the intensity *I* of an EPR transition is proportional to $Sin\theta/[dB(\theta)/d\theta]$, the turning points can mark positions of maximum EPR absorption intensity.

$$I \propto Sin\theta/[dB(\theta)/d\theta] \qquad [5.2]$$

The proportionality of *I* to sinθ reflects very large number of systems with axes nearly perpendicular to the field direction, and by contrast there will be very few systems with their axes aligned close to the field direction. The angular dependence of the five fine structure transitions for the case of Mn(II) in KN_3 from earlier work of King and Miller is shown in figure V-2.[2] Orientations corresponding to the turning points, for which $dB_{res}(\theta)/d\theta = 0$, show minimum susceptibility to a variation of magnetic field direction. The features in between the turning points from one set of M_s transition may mask the peaks corresponding to the turning points of a different transition that may be of interest (figure V-2). So, the resolution of a multiline powder spectrum would be considerably improved if only the features for which $dB(\theta)/d\theta = 0$, can be accentuated in a magnetic field jump experiment.

V.2 Basic principles of Echo-detected EPR with vector field jumps

In a one axis field jump experiment, a dc field pulse is applied transverse to the static field B_o during the application of the refocusing π-pulse in a two-pulse ESEEM

experiment according to the pulse scheme shown in figure V-3. It results in an attenuation of all the contributions except those from the principal axis directions. For complete suppression, a three-pulse experiment with two transverse dc pulses is required.[1] To apply echo-detected EPR with vector field jumps there should be anisotropy either in the electronic Zeeman interaction, the fine structure or in hyperfine interaction term.

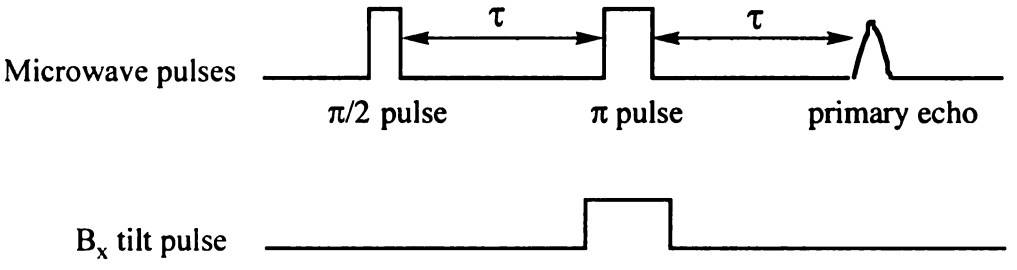

Figure V-3: Pulse scheme for two-pulse field jump experiment.

In order to tilt the static magnetic field by a small angle in a field jump experiment, a transverse field B_x is applied over a time which is short compared to the electron spin relaxation times T_1 and T_2, while keeping the magnitude of the static field constant. Since the intensity I is dependent on the variation of resonant field position with θ (equation 5.2), the effect of change in θ on the transitions can be seen by differentiating equation 5.1 with respect to θ,

$$dB_{res}(\theta)/d\theta \approx 6D(M_s\text{-}1/2)\sin\theta\cos\theta \qquad [5.3]$$

where the higher order terms in D and the hfi have been neglected. Only the orientations for which $dB_{res}(\theta)/d\theta = 0$, show minimum susceptibility to a variation of magnetic field direction. This condition is met for the spin systems for which $\theta = 0°$, $90°$ or $M_s = 1/2$; the resonance condition does not change for small tilts and the refocusing π-pulse can fully refocus the corresponding magnetization. For the case of $M_s = 1/2$, some dependence on orientation is expected to arise due to the second order terms that were neglected in equation 5.3. For all the other crystallite orientations the resonance conditions would be changed depending on θ and the tilt angle. Hence, the features corresponding to the turning points of $B(\theta)$ variation with θ will become pronounced in the spectrum and the contributions from all other orientations will be attenuated.

V.3 Materials and Methods

Two-pulse echo-detected EPR and ESEEM experiments were performed at X-band with magnetic field vector jumps on frozen samples of 10 mM Mn-EDTA complex in 50-50% water ethylene glycol mixture at 4.2K, using a Mims type microwave transmission cavity[3] with an eight-turn ENDOR coil wound around a half wave stripline resonator. The data were collected on the pulsed-spectrometer described earlier. Current generated by a home-built pulsed current source[4] was passed through the ENDOR coil producing the desired tilting magnetic field $\mathbf{B_x}$ whose position in time was controlled by a delay and gate generator. It was placed symmetrically with respect to the π-pulse (figure V-3). The directions of the static field, $\mathbf{B_0}$, the microwave field, $\mathbf{B_1}$, and the tilt field, $\mathbf{B_x}$, were mutually perpendicular.

V.4 Results

V.4.1 Two-pulse echo detected EPR with field vector jumps

In order to test the instrumentation, two-pulse echo-detected EPR spectra for Cu(II) in frozen aqueous-ethylene glycol solution were obtained with and without field jumps (figure V-4). They showed resolution enhancement similar to those observed for bis-(oxalato) Cu(II) in frozen aqueous-glycerine solution by S. Pfenninger et al.[1] For Cu, I = 3/2 and $A_{\|}$ hyperfine coupling of the copper nucleus gives rise to the two steps observed in the low-field region. The splitting due to $A_{\perp}$ was not resolved. On application of magnetic field jump, three distinct steps in the low-field region were observed. In the high-field region, application of the tilt-field lead to narrowing of the $g_{\perp}$ peak. Further experiments were performed on Mn-EDTA in frozen aqueous-ethylene glycol solution. Use of wide microwave pulses removed any possible modulations arising from EDTA nitrogens (figure V-5). Although the contributions from arbitrary orientations can not be eliminated completely, enhancement in resolution was observed with tilt-pulse generated with dc voltage > 40V as shown in figure V-6. The voltage corresponds to the amount of current passed through the coils generating the tilt field. The exact magnitude of the tilt field was not calculated. In two-pulse echo-detected EPR experiment, the width and the magnitude of the dc field pulse was varied in order to find a suitable value to perform the two-pulse ESEEM experiment with single axis field jump.

V.4.2 Two-pulse ESEEM experiments with field vector jumps

The two-pulse ESEEM spectrum with single axis field jump on Mn-EDTA complex in frozen aqueous-ethylene glycol solution is shown in figure V-7. The results

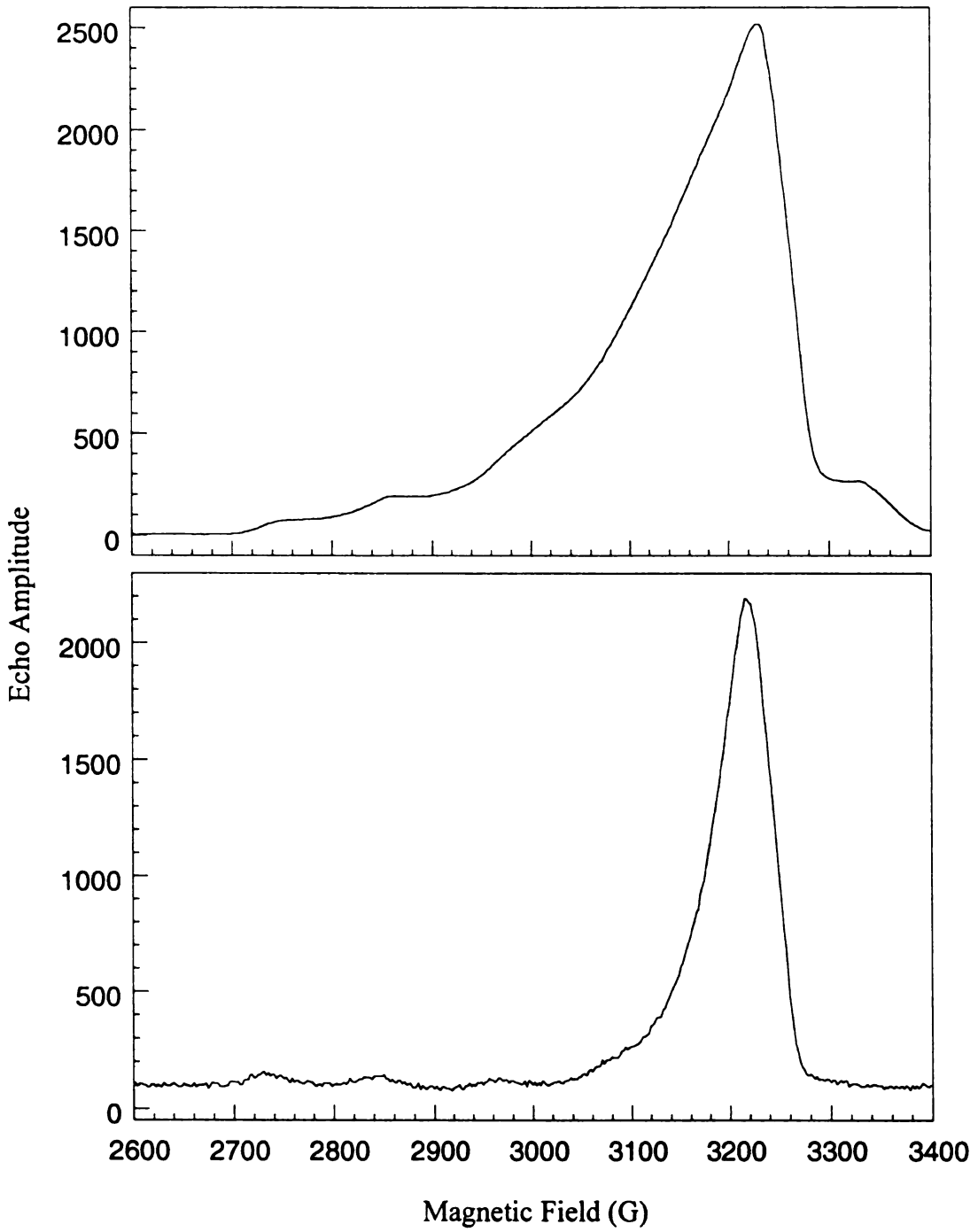

Figure V-4: Echo detected EPR spectrum with field jump for Cu(II) in frozen aqueous-ethylene glycol solution. (a) without the application of B_x pulse (b) in presence of B_x pulse proportional to a voltage of 220V; microwave frequency, 9.80GHz; τ, 500 ns; microwave pulse width = 20 ns.

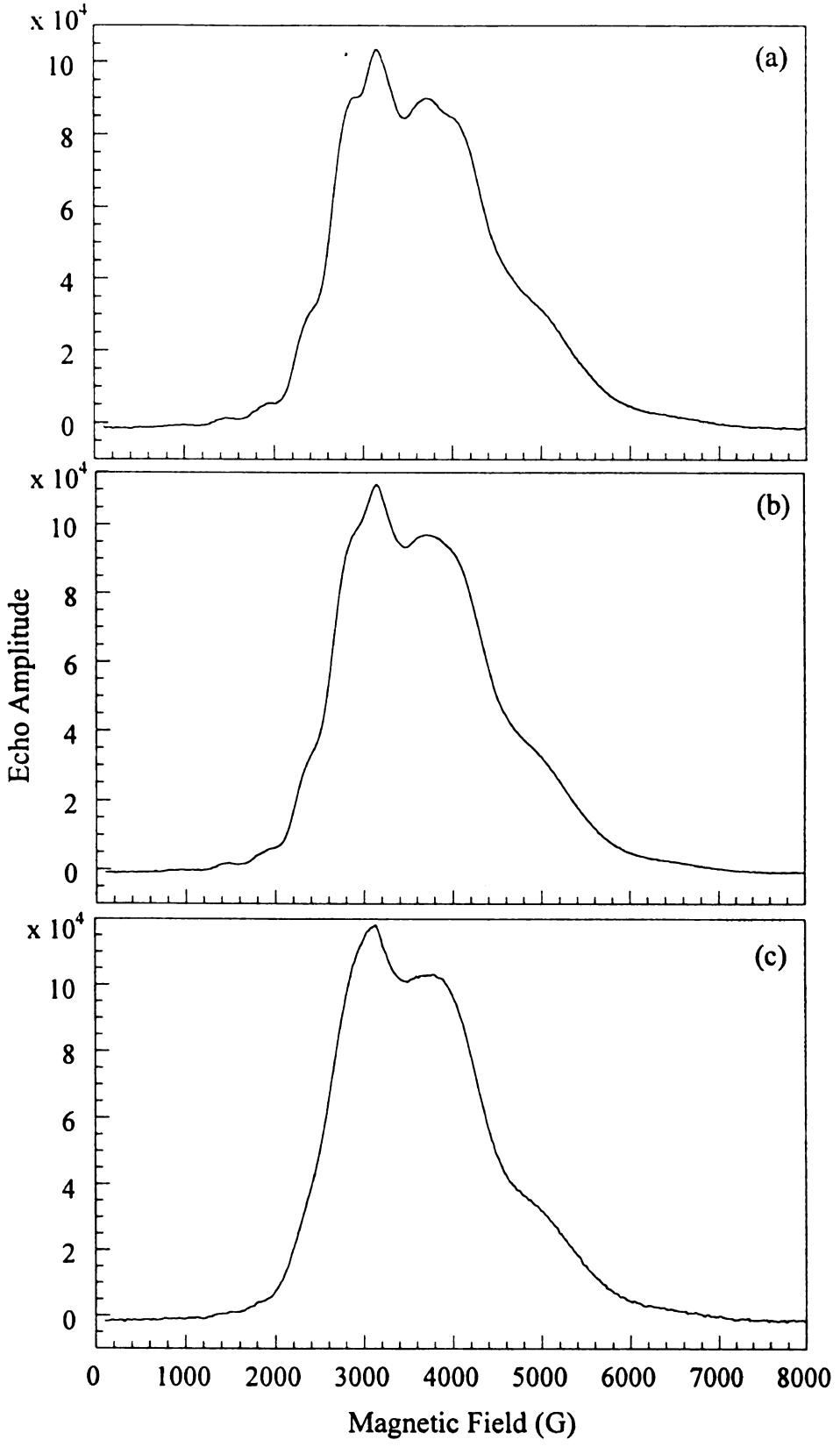

Figure V-5: Echo detected EPR spectra of Mn(II)-EDTA in frozen aqueous-ethylene glycol solution using different microwave pulse-widths (a) 20 ns; (b) 40 ns (c) 110 ns;. τ, 500 ns; pulse repetition rate, 60 Hz, microwave power, 40 dBm, temperature, 4.2 K. The B_x tilt field was not applied.

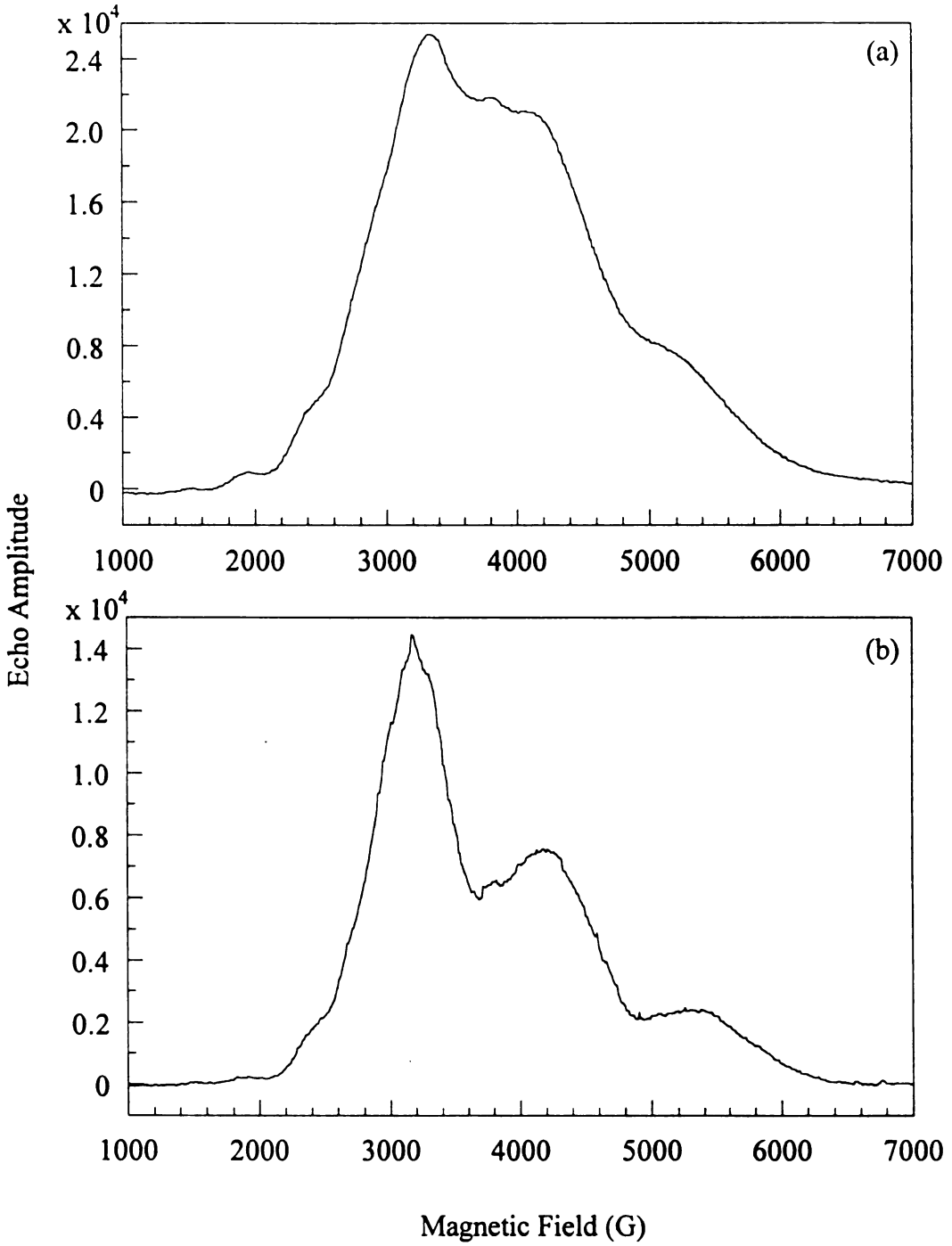

Figure V-6: Echo detected EPR spectrum with field jump of Mn(II)-EDTA in frozen aqueous-ethylene glycol solution. (a) without the application of B_x pulse (b) in presence of B_x pulse proportional to a voltage of 250V; microwave frequency, 9.80 GHz; other conditions same as in figure V-5.

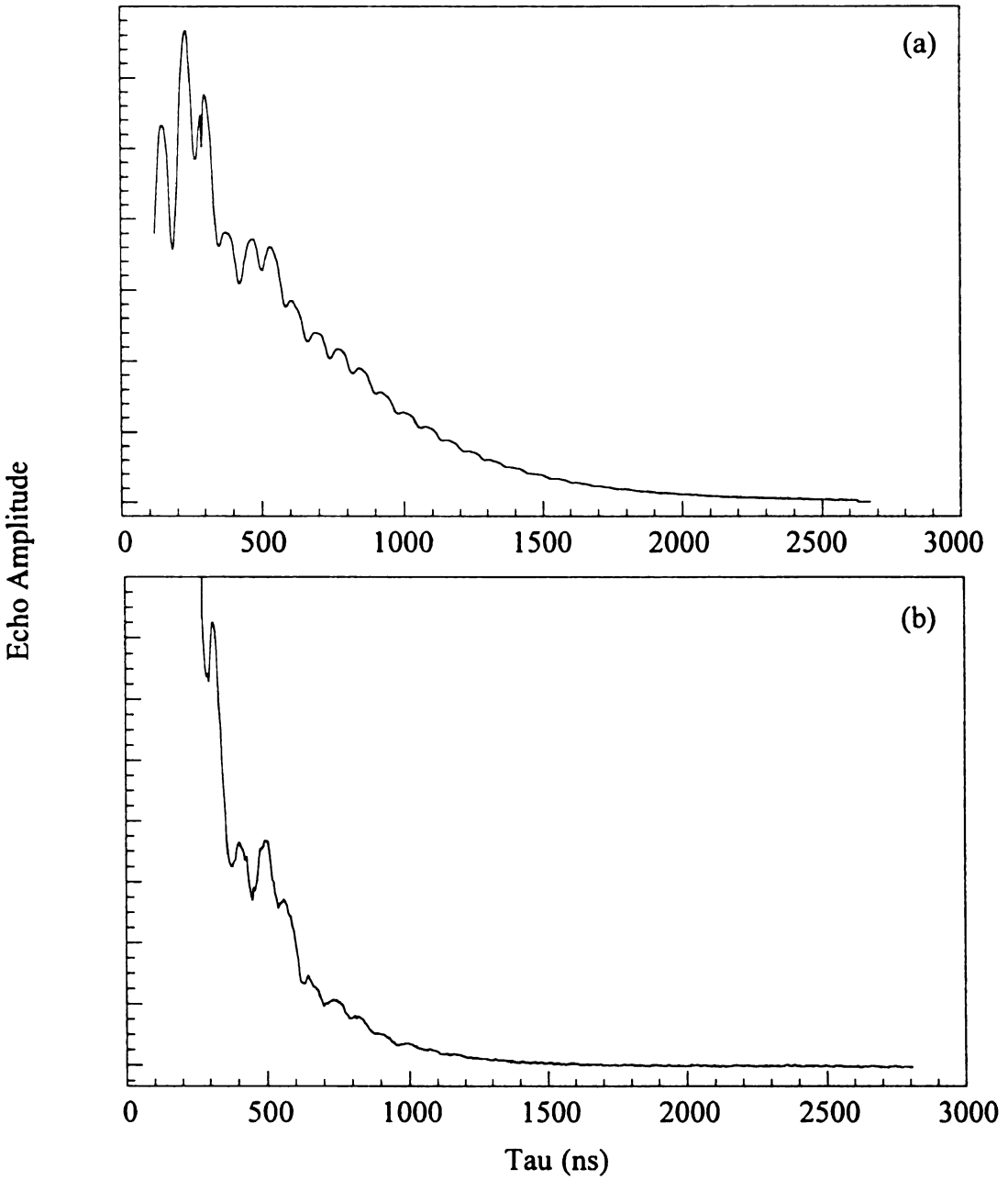

Figure V-7: Two pulse ESEEM spectra with field jump: (a) without the application of B_x pulse; (b) in presence of B_x pulse proportional to a voltage of 100V applied. Conditions: microwave frequency, 8.949 GHz; τ, 250 ns; magnetic field = 2800 G.

were not as expected. The decay time was further reduced in presence of field $\mathbf{B_x}$ due to possible increase in available relaxation mechanisms, reducing the frequency resolution rather than improving it.

V.5 Discussion

The EPR properties of Mn(II) are governed by the distribution of unpaired electrons around Mn nucleus, which is dependent on the type of ligands present and their geometrical arrangement about the ion. In the free ion each 3d orbital contains a single electron, and has a spherical charge distribution about the Mn nucleus. In the presence of ligands, interactions between d electrons and electrons localized on the ligand atoms remove the degeneracy and the spherical symmetry of the d electron distribution. In a perfect cubic symmetry of ligand environment either octahedral or tetrahedral, the six-fold spin degeneracy in absence of external magnetic field is lifted and creates a very slight cubic zero field splitting. Deviation of electronic symmetry about the ion from octahedral or tetrahedral case leads to a much larger ligand-induced quadratic zero field splitting. This is expected to be the case in Mn-EDTA complex, due to non-cubic environment as seen in the structure determined by analysis of three-dimensional X-ray data.[5,6] Mn(II) is in sexadentate seven-coordinated state (figure V-8) in Mn-EDTA complexes [Mn $(H_2O)_4$] - $[MnH.EDTA.H_2O]_2.4\ H_2O$ and in $MnMn(EDTA).9H_2O$. In Mn-EDTA complex, the cis-nitrogen coordination results in a highly anisotropic spectrum. The EPR spectra of randomly oriented sample of Mn(II) complexes often have features arising due to both allowed and forbidden transitions. The spectra are best interpreted with the aid of a spin Hamiltonian. Although the magnitude of zfs parameters D and E may not lead

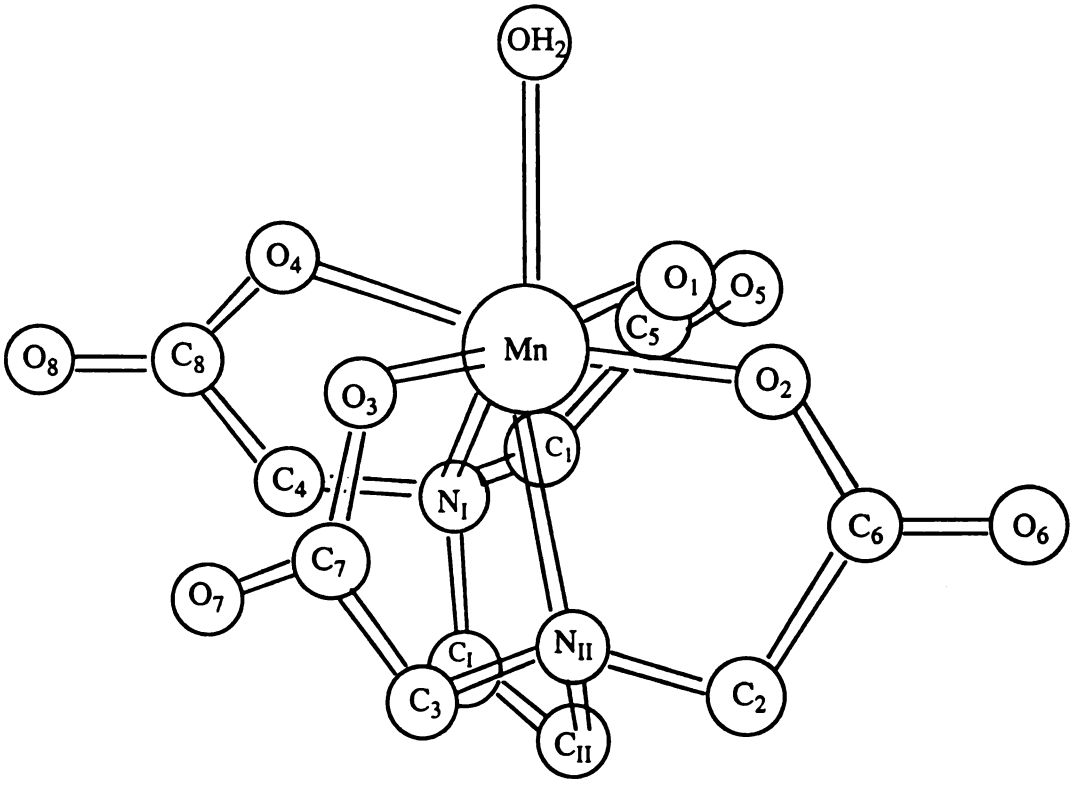

Figure V-8: Model of the structure of sexadentate seven-coordinated Mn-EDTA complex with twofold vertical axis.

directly to structural information, they can be used to account for the positions of all the features in the spectrum. The major terms in the spin Hamiltonian include the electronic Zeeman interaction which is the dominant term at X-band; the electron nuclear hyperfine coupling, which is usually isotropic and typically has a value of 95 G for an octahedrally coordinated Mn(II) ion; and zfs interaction arising from the interaction of Mn in non-spherical ligand environment.

The EPR spectra from earlier work by Reed, G. H. and Markham, G. D.[7,8] on Mn-EDTA in solution at Q-band and at 50°C and 3°C at X-band are shown in figure V-9. The spectrum at X-band is inhomogeneously broadened and does not show the expected five distinct nondegenerate central electron transitions usually seen in the spectra of Mn(II) complexes. From the Q-band spectrum, the value of the hyperfine coupling is be found to be ~95 G. If the small quartic terms in equation [1] are omitted, the spin Hamiltonian can be written as;

$$H = \beta \mathbf{B_o} \cdot \mathbf{g} \cdot \mathbf{S} + D\,[S_z^2 - 1/3\ S(S+1)] + E\,(S_x^2 - S_y^2) + A\,\mathbf{I} \cdot \mathbf{S} \qquad [2]$$

The magnitudes of D and E depend on how strongly the unpaired spins interact. If D and E are zero then an isotropic absorption line with a g value slightly greater than 2 is usually observed.[9] If D and E are finite but small (0.001-0.1 cm^{-1}) five ESR transitions are observed. If D or E is large compared to ($g\,\beta\,B_o$), there can be two limiting cases $D \neq 0$, $E = 0$ and $D = 0$, $E \neq 0$. The eigenvalues and eigenvectors of [2] in zero magnetic field are then three Kramers doublets. In the first case, the lowest Kramers doublet has effective g values $g_{||} = 2$, $g_{\perp} = 6$ and is experimentally observed in systems with a three fold or higher axis of symmetry with strong axially symmetric electric fields. In the

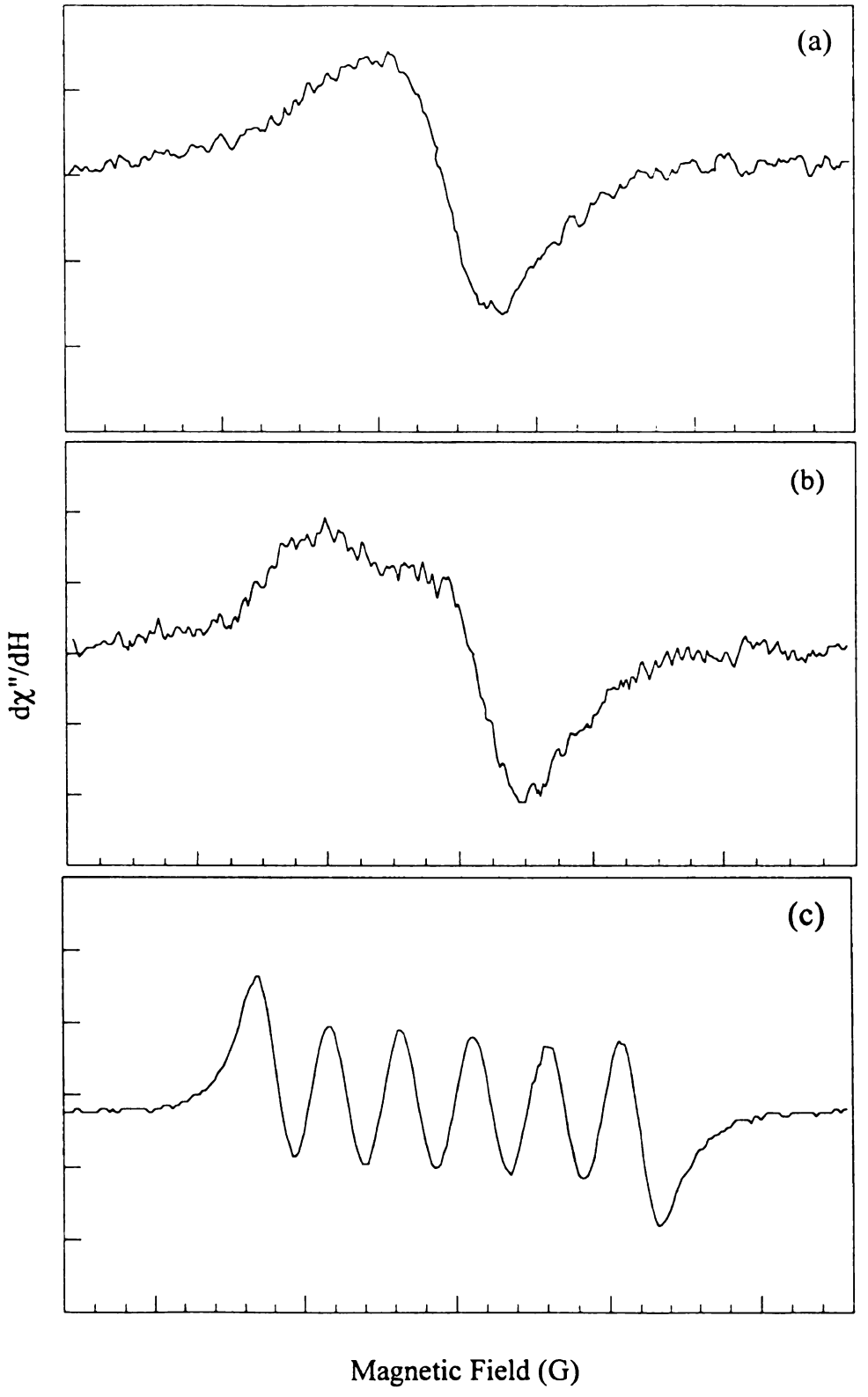

Figure V-9: X-band cw-EPR spectrum of Mn-EDTA (0.002 M) (a) at 50° C and (b) at 3° C; microwave frequency, 9.1GHz. Taken from reference 7. (c) Q-band cw-EPR spectrum of Mn-EDTA (0.01 M) obtained at 20° C; microwave frequency, 35 GHz. Taken from reference 8.

second case the middle doublet has an isotropic effective g value of 4.29.[10] This case occurs so long as the environment of the d^5 ion is more symmetric than the over-all symmetry group of the site, and D need not be zero but shall be small. The small D term would have the effect of broadening the line at g = 4.29 and the ratio $\lambda = E/D$, has been calculated from the observation of such broadening in some cases.[11] When both D and E are large compared with ($g \beta B_o$), g = 4.29 signal can arise if λ is 1/3. If $\lambda = 0$ represents axial symmetry ($D \neq 0$, $E = 0$), then an increase in λ represents a departure towards rhombic symmetry, $\lambda = 1/3$ represents maximum possible rhombic symmetry with equally spaced Kramers doublets and values greater than 1/3 represents a convergence towards axial symmetry, with $\lambda = 1$ representing entirely axial symmetry.

A simulation of the spectrum in figure V-6(a) using Simfonia simulation program provided by Bruker Instruments is shown in figure V-10. In comparing features of this theoretical spectrum with the experimental spectrum it is important to note that the simulation program is based on the perturbation treatment and the perturbation solutions work fairly well for Q-band spectra (35 GHz) but are more approximate for X-band spectra because of the relative magnitudes of the Zeeman and zfs terms. Hence, for X-band, unless the zfs is pretty small, it is difficult to fit the experimental data perfectly. All of the fine structure transitions need not have the same relaxation time (line width) and relaxation times may differ for $\theta = 0°$ and $\theta = 90°$ orientations. Additional complexities may arise from forbidden hyperfine transitions and from rhombic distortions. Literature data for Mn(II) compounds indicate that D generally does not exceed 1000G in distorted octahedral environments,[12] but similar information is not available for heptacoordinated manganese ions. The simulation gave an estimate of the

isotropic and anisotropic zfs parameters D and E to be 1180-1160G and 265-220G respectively giving a value of $\lambda = 0.22$ indicating deviation from axial symmetry, as is expected for a seven coordinate Mn(II).

Magnetic field positions for centers of fine structure transitions as a function of the extent of axial distortions are given in figure V-11. Diagrams representing solutions to the Hamiltonian in equation [1] for both axial and rhombic symmetries over a wide range of zfs are available.[13] The values of zfs parameters obtained by simulation fall in the range of that obtained from this diagram. These values of the zfs parameters also fall in the range estimated for the case of heptacoordinated site of Mn(II) doped into the diamagnetic compound $MgMg(EDTA).9H_2O$ where Mn occupies a heptacoordinated site.[6]

Figure V-6(b) shows the echo detected EPR spectrum obtained in the presence of tilting field $\mathbf{B_x}$. An improvement in the resolution is obtained because features other than those from the principal axis directions are suppressed. As seen in the figure V-3 central transition has minimum dependence on θ so, it is expected to contribute maximum to the spectrum of figure V-6(b).

Two-pulse ESEEM spectrum were obtained with single axis field jumps on the Mn-EDTA complex in order to extract information about the hyperfine couplings. The decreased resolution observed could be due to the fact that the enhancement in resolution achieved from suppression of contributions from non principal axis orientations was overcome by decrease of the transverse relaxation time, T_2. Transverse relaxation arising from local magnetic field inhomogenities due to coupling between magnetic dipoles varies as a function of $(1 - \cos^3\theta)/r^3$, where r is the distance between spins and θ is the angle

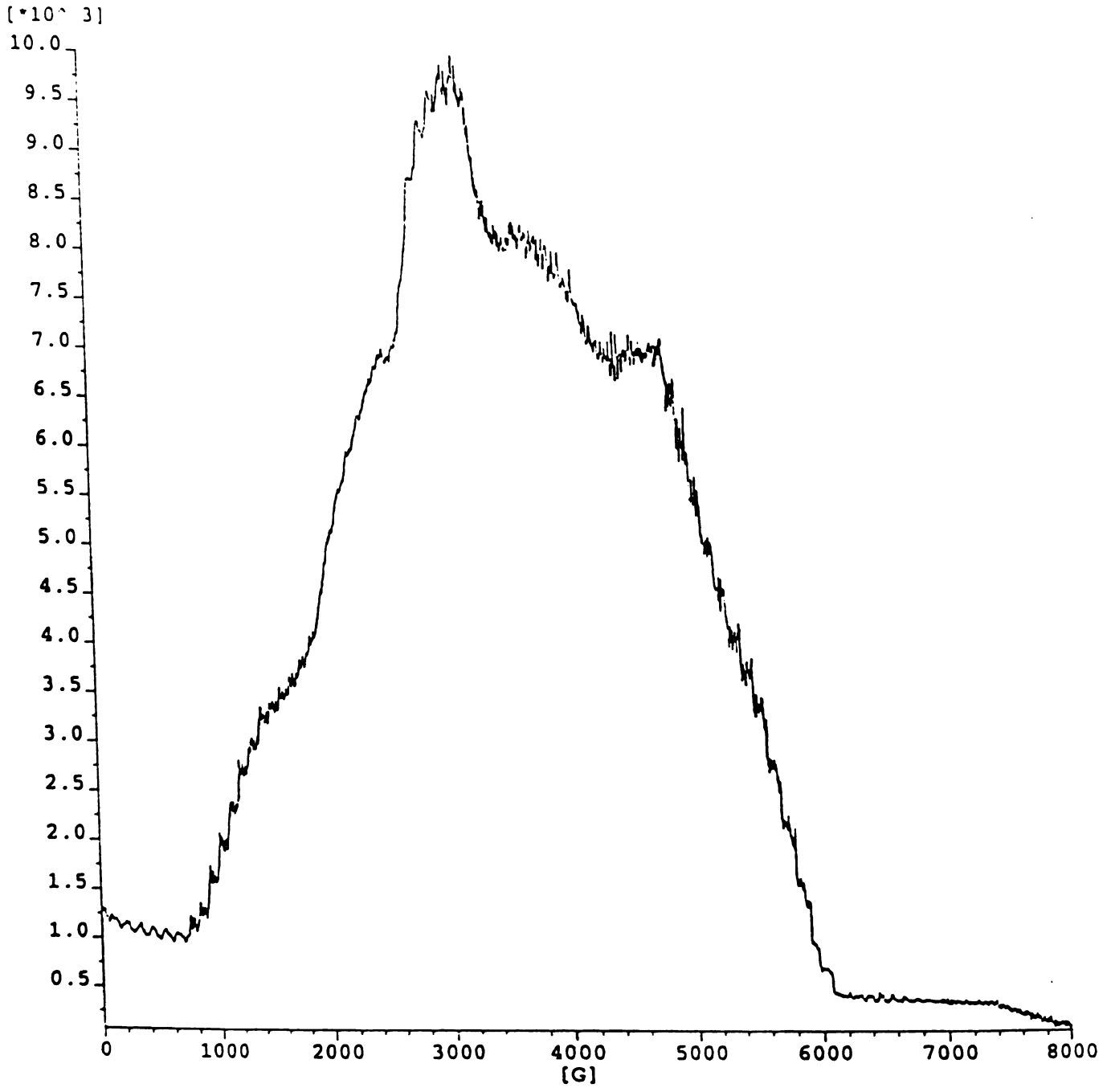

Figure V-10: Simulation using Simfonia simulation program provided by Bruker Instruments. Simulation parameters: D = 1180G, E = 265G, Microwave frequency, 9.104GHz, isotropic g value, 1.946.

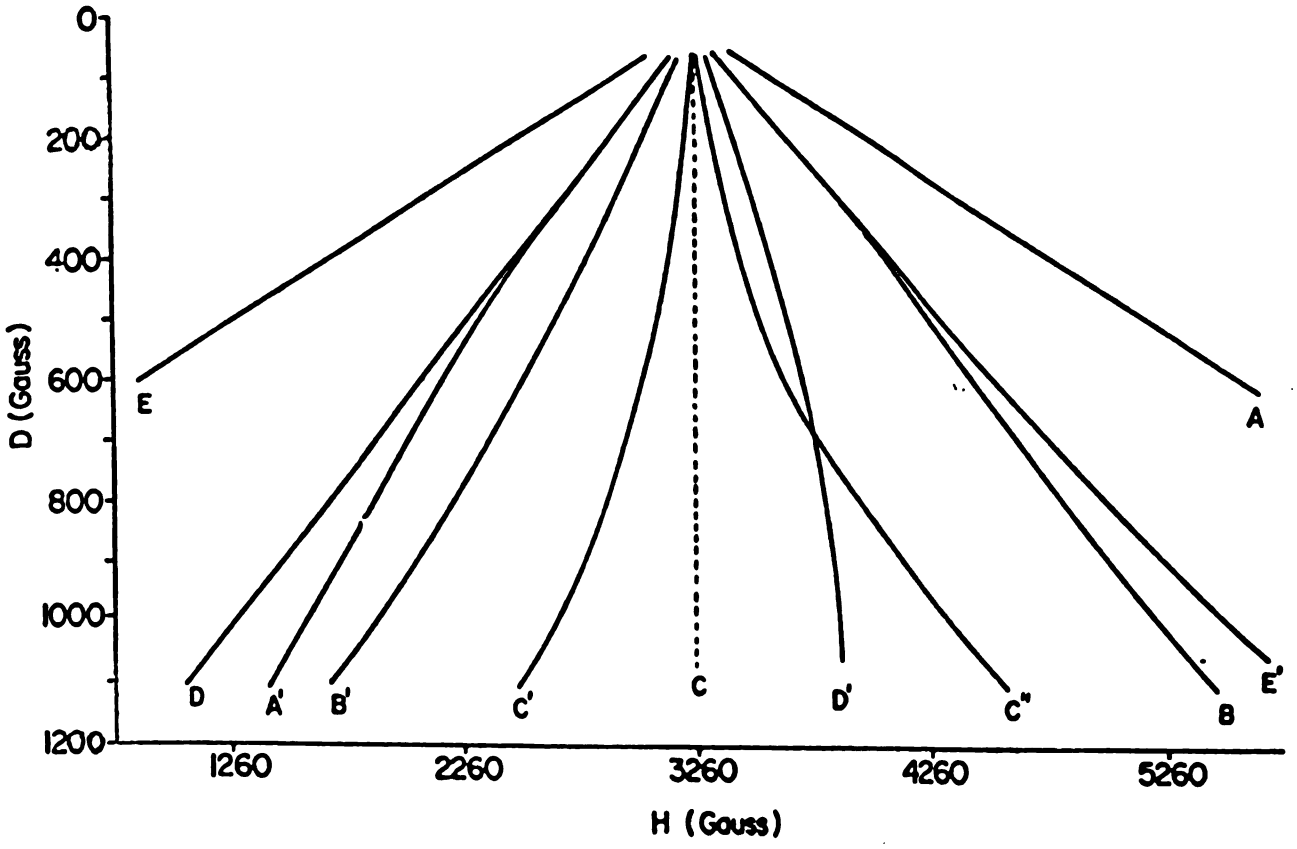

Figure V-11: Magnetic field positions of the fine structure transitions in a powder spectrum of a $^{55}Mn(II)$ complex with axial symmetry as a function of zfs at X band. D is assumed to be negative. Unprimed letters indicate the transitions for $\theta = 0°$; primed for $\theta = 90°$ and C" is for the central transition at $\theta = 41°48'$. A, 5/2 ↔ 3/2; B, 3/2 ↔ 1/2; C, 1/2 ↔ -1/2; D, -3/2 ↔ -1/2; and E, -5/2 ↔ -3/2. Free electron resonance position, g = 2.0023, coincides with C. Taken from reference 12.

between external field and the symmetry axis of the system. As seen in figure V-3 the pulse $\mathbf{B_x}$ is on for a much longer time as compared to mw-pulse $\mathbf{B_1}$. At the end of the refocusing pulse, the magnetizations forming the primary echo, experience field $\mathbf{B_x}$ for some time before it is turned off. The presence of an additional field $\mathbf{B_x}$, perpendicular to $\mathbf{B_0}$, may lead to an increase in local field fluctuations and reduction of the ESEEM decay time.

V.6 Conclusions

Using the magnetic field jump method, some enhancement in the ESE-detected EPR spectrum of Mn-EDTA was observed. It is also important to obtain a symmetrical tilt pulse and to be able to place the B_x pulse symmetrically with respect to the refocusing π-pulse, this would allow refocusing of the magnetization that is defocused due to the inhomogeneities in the B_x field. To provide the desired enhancement for ESEEM spectra, probe structures that yield more homogeneous pulsed magnetic fields are needed.

List of References

1)Pfenninger, S.; Schweiger, A.; Forrer, J.; Ernst, R. R. *Chem. Phys. Lett.* **1988**, *151*, 199-204.

2)King, G. J.; Miller, B. S. *J. Chem. Phys.* **1964**, *41*, 28-40.

3)Davis, J. L.; Mims, W. B. *Rev. Sci. Instrum.* **1978**, *49*, 1095-1097.

4)Forrer, J.; Pfenninger, S.; Sierra, G.; Jeschke, G.; Schweiger, A.; Wagner, B.; Weiland, T. *Appl. magn. Reson.* **1996**, *10*, 263-279.

5)Richards, S.; Pedersen, B.; Silverton, J. V.; Hoard, J. L. *Inorganic Chemistry* **1964**, *3*, 27-33.

6)Borras-Almenar, J. J.; Burriel, R.; Coronado, E.; Gatteschi, D.; Gomez-Garcia, C. J.; Zanchini, C. *Inorg. Chem.* **1991**, *30*, 947-950.

7)Reed, G. H.; Leigh, J. S. J.; Pearson, J. E. *J. Chem. Phys.* **1971**, *55*, 3311-3316.

8)Reed, G. H.; Markham, G. D. *Biological Magnetic Resonance*; Berliner, L. J. and Reuben, J., Ed.; Plenum: New York, 1984; Vol. 6, pp 73-142.

9)Orton, J. W. *Rep. Progr. Phys.* **1959**, *22*, 204.

10)Castner, T.; Newell, G. S.; Holton, W. C.; Slichter, C. P. *J. Chem. Phys.* **1960**, *32*, 668.

11)Wickman, H. H.; Klein, M. P.; Shirley, D. A. *J. Chem. Phys.* **1965**, *42*, 2113.

12)Carlin, R. L. *Magnetochemistry*; Springer-Verlag: Berlin, Heidelberg, 1986.

13)Aasa, R. *J. Chem. Phys.* **1970**, *52*, 3919.